Time-resolved spectroscopic studies of photovoltaic and photosynthetic materials

Rhea Kumar

Submitted for the degree of Doctor of Philosophy
Department of Chemistry, Imperial College London
January 2022

Declaration

I hereby declare that this thesis and the work reported herein was composed by and originated entirely from me. Information derived from the published and unpublished work of others has been acknowledged in the text and references are given in the list of sources.

The copyright of this thesis rests with the author. Unless otherwise indicated, its contents are licensed under a Creative Commons Attribution-Non Commercial 4.0 International Licence (CC BY-NC). Under this licence, you may copy and redistribute the material in any medium or format. You may also create and distribute modified versions of the work. This is on the condition that: you credit the author and do not use it, or any derivative works, for a commercial purpose. When reusing or sharing this work, ensure you make the licence terms clear to others by naming the licence and linking to the licence text. Where a work has been adapted, you should indicate that the work has been changed and describe those changes. Please seek permission from the copyright holder for uses of this work that are not included in this licence or permitted under UK Copyright Law.

Publications

The work carried out during the course of this PhD resulted in the following publications:

1. T. R. Hopper, D. Qian, L. Yang, X. Wang, K. Zhou, **R. Kumar**, W. Ma, C. He, J. Hou, F. Gao and A. A. Bakulin, *Chem. Mater.*, **31**, 6860-6869, 2019.

2. A. Weu, **R. Kumar**, J. F. Butscher, V. Lami, F. Paulus, A. A. Bakulin and Y. Vaynzof, *Adv. Funct. Mater.*, **30**, 1907432, 2019.

3. C. Labanti, M. J. Sung, J. Luke, S. Kwon, **R. Kumar**, J. Hong, J. Kim, A. A. Bakulin, S. Kwon, Y. Kim and J. Kim, *ACS Nano*, **15**, 7700-7712, 2021.

4. D. Becker-Kock, M. Albaladejo-Siguan, J. Kress, **R. Kumar**, Y. J. Hofstetter, Q. An, A. A. Bakulin, F. Paulus and Y. Vaynzof, *Nanoscale*, **14**, 3020-3030, 2022.

5. P. Jacoutot, A. D. Scaccabrozzi, T. Zhang, Z. Qiao, F. Anies, M. Neophytou, H. Bristow, **R. Kumar**, M. Moser, A. D. Nega, A. Schiza, A. Dimitrakopoulou-Strauss, V. Gregoriou, T. Anthopoulos, M. Heeney, I. McCulloch, A. A. Bakulin, C. L. Chochos and N. Gasparini, *Small*, **18**, 2200580, 2022.

Abstract

Soft materials employing organic molecules are among the front-running candidates for next-generation solar cells. They offer lightweight, flexible characteristics which are cheap to produce and implement, making them more promising than commercially available inorganic photovoltaics. Furthermore, the possibility to tune the molecular structure of organic components presents an infinite pool of opportunity in the endeavour to enhance photovoltaic performance. This thesis evaluates a collection of soft materials from various perspectives that are currently at the forefront of photovoltaic research. The investigations described herein aim to elucidate the mechanisms contributing to photovoltaic performance by application of time-resolved spectroscopic tools.

Chapter 3 examines the effects of chemical structure modification on small molecule components for organic photovoltaic devices. Two studies are presented, both of which describe a regioisomeric modification on a molecular structure that is incorporated into a photovoltaic blend. In both cases, transient absorption spectroscopy reveals stark contrasts in the materials' exciton and charge dynamics which strongly influence their propensity for photovoltaic charge generation. The discussion highlights the dramatic consequences of minor structural differences in organic photovoltaic components, which emphasises the immense potential for their development.

Chapter 4 considers the operational stability of photovoltaic devices comprising soft materials, which is a major hurdle currently hindering their industrialisation. Two studies are presented, in which charge dynamics unravelled by transient absorption spectroscopy are used to rationalise the studied materials' lifetimes under operational conditions.

Chapter 5 explores the natural biological apparatus for photovoltaic light-harvesting by examining photosynthetic microorganisms. A range of electrochemical and time-resolved spectroscopic methods are employed in order to investigate photoinduced processes in cyanobacteria in bio-photovoltaic devices as well as *in vivo*.

Overall, the research demonstrated in this thesis establishes fundamental findings for advancing soft photovoltaic materials. The insights regarding photophysical processes and optoelectronic properties of the studied systems highlight crucial lessons for material optimisation which could aid in their development, contributing to the goal of commercialisation.

Acknowledgements

First and foremost, I must extend the utmost gratitude to my supervisor **Dr Artem Bakulin** for his expert guidance. Over the last three years, I have had the privilege to indulge in a diverse range of projects that you have entrusted to me, each of which presented uncharted phenomena in my research journey. This, together with your insight and spectroscopic eye, have allowed me to learn, grow and enjoy these years more than I ever expected to.

To **Tom**, thank you for teaching me all that you did, albeit a negligible fraction of what you know. I am sure you would hate to admit it, but your investment in my feeble attempt at research was instrumental to this thesis. I hope to one day be reviled by you in a conference audience, like the good old days.

To **Yifan**, thank you for all of your advice and guidance. Your expertise with spectroscopy and OSCs, as well as your kind and generous nature, made you a crucial pillar in our group.

To **Neath**, I would not have come close to surmounting one of the greatest hurdles of this work without the help of you and *Mittens*. Midnight TeamViewer SOS-sessions aside, thank you for your encouragement and interest in my projects, but mostly for your support and friendship.

To **Polly**, I could never have imagined a greater companion with whom to attempt a PhD. Whether it was coffee, beer, or tears, we shared it and grew through it together. You truly have been my sanity everyday.

To **Jiaxin**, in the best way possible, you have been my *insanity* everyday. Thank you for the clouds of laughter that you leave behind you everywhere you go and for the fantastic energy that you bring to the group.

To **Alice**, the personification of sunshine and my electrochemical guru. Of course, I couldn't have attempted many of my experiments without our afternoons together accessorising with various electrical components. Thank you for your knowledge but more so, thank you for your sweet optimism that keeps us all warm on difficult days.

To **Ben**, thank you for being a fundamental lifeline in monotonous teaching labs. Thank you for your patient and empathetic ear when I needed to moan. I am sure our paths will cross in two years when you once again follow me in my career choices.

To **Marios**, how perfect that the person I jokingly named my cyanobacteria's Godfather will be the one to take care of them after I am gone. My final project would be nothing without your tireless efforts and your enthusiasm. Thank you for making my last few months in our lab so memorable. I will never forget the excitement of seeing oscillations in our spectra in real-time, nor will I forget the subsequent blow of realising it was just our sample dying.

To **Haoqing**, thank you for the blood, sweat and tears you shed over the spectrometer that granted me a final chapter to this thesis. Thank you for being just as excited as me when I was getting good data, and for being so helpful and knowledgeable when I wasn't.

To **Dima**, thank you for your kind companionship in the lab and in the office. Thank you also for your infinite electrical wisdom; the IPCE setup would have never seen life without your advice and your connecty-thing. I clearly still have a lot to learn.

To **Shawn**, thank you for your ingenuity and honesty that always brought insight to my projects in difficult moments. I hope you never change (although a touch less Red Bull could be good for the heart).

To **Tong**, thank you for your warm character that was a constant in our office at all hours of the day. Although I was never fortunate to work directly with you, I am not at all surprised that you chose to stay on in our group for a PhD, and I am glad that you did.

To **Ziyuan**, I am eternally grateful for your help on the IPCE project and even more so for the lovely company (and snacks) that you have provided over the last year. I sincerely hope that the next two years don't ruin your ever-cheerful nature.

To the long-awaited and very much needed postdocs **Ziming** and **Navendu**, thank you for coming to save us. Although I never had the privilege of working with you, I am excited to see all that you will conquer within our group as it continues to grow. I am sure your experience will be fundamental to the development of the Ultrafast Optoelectronics group.

To those that left us postdoc-less many years ago, **Ernest** and **Andrei**, your expertise was greatly missed after your departure. Thank you for all of the informative discussions in the early days of my PhD that helped me find my feet.

To **Pabitra** and **Li**, thank you for all that you do to keep the research operation running. The first port of call in a crisis, your help was essential to many experiments presented herein.

I would also like to thank all of the excellent scientists with whom I have been honoured to collaborate. Thanks to **Dr Jenny Zhang** and **Dr Laura Wey** for the infinite supply of cyanobacteria cultures that you allowed me to kill, as well as for your patient guidance as I struggled with them. Thanks to **Tomi Baikie** and **Pratyush Ghosh** for coming to Imperial and for having equally crazy ambitions pertaining to what we could achieve with the cyanobacteria, granting me the funnest experiments of my PhD. Thanks to **Prof Yana Vaynzof, Prof Ji-Seon Kim, Dr Andreas Weu, Chiara Labanti** and **Dr David Becker-Koch** for providing me with materials to attack with lasers and for rewarding and interesting projects.

Last but not least, I sincerely thank my family. To **my Grandad**, the most enthusiastic person in the world with regards to my career, and **my Grandma** who taught me the art of attention to detail right at her dressing table. To **my parents**, who fostered in me an (at times delusional) sense of ambition which led me to believe with steadfast certainty at various points in my life that I would one day be a doctor, a lawyer, a musician, an astronaut... thanks for your endless support. To **my brothers**, who in your own distinct and opposite ways are my biggest role models; thank you for your unwavering excitement not just for my PhD but for every component of my life, and for generally being my most supportive and favourite people. Above all, however, I would like to thank my extended family and Ben, who never fail to brighten the stressful or challenging moments thanks to their boundless supplies of fun and spirit.

From a letter to another mathematician, impeccably embodying the scientific process:

"I am in a charming state of confusion."

Ada Lovelace, 1843

Nomenclature

Frequently used acronyms

A	Electron-accepting component
AO	Atomic orbital
BHJ	Bulk heterojunction
BPV	Biophotovoltaic device
CS	Charge separation
CT	Charge transfer
D	Electron-donating component
ES	Excited state
ET	Energy transfer
ETL	Electron transporting layer
FRET	Förster resonance energy transfer
GA	Global analysis
GSB	Ground state bleach
HOMO	Highest occupied molecular orbital
HTL	Hole transporting layer
IPCE	Incident photon-to-electron conversion efficiency

LUMO	Lowest unoccupied molecular orbital
MO	Molecular orbital
NC	Nanocrystal
NFA	Non-fullerene acceptor
OD	Optical density
OPV	Organic photovoltaic
PCE	Power conversion efficiency
PES	Potential energy surface
PIA	Photoinduced absorption
PL	Photoluminescence
PSI	Photosystem I
PSII	Photosystem II
QDSC	Quantum dot solar cell
RC	Reaction centre
SCOM	Spectral centre of mass
SE	Stimulated emission
TA	Transient absorption
TCSPC	Time-correlated single photon counting
UV-Vis	Ultraviolet-visible
WOC	Water oxidation complex

Chemical names

$AgBiS_2$	Silver bismuth sulfide
BDT	Benzodithiophene

D18	Poly[(2,6-(4,8-bis(5-(2-ethylhexyl-3-fluoro)thiophen-2-yl)-benzo[1,2-b:4,5-b']dithiophene))-alt-5,5'-(5,8-bis(4-(2-butyloctyl)thiophen-2-yl)dithieno[3',2':3,4;2",3":5,6]benzo[1,2-c][1,2,5]thiadiazole)]
DCI	1,1-Dicyanomethylene-3-indanone
DRCN5T	2,2'-[(3,3"',3"",4'-tetraoctyl[2,2':5',2":5",2"':5"',2""-quinquethiophene]-5,5""-diyl)bis[(Z)-methylidyne(3-ethyl-4-oxo-5,2-thiazolidinediylidene)]]bis-propanedinitrile
EDT	1,2-Ethanedithiol
FTO	Fluorine-doped tin oxide
IDT	Indacenodithiophene
IO-ITO	Inverse-opal indium tin oxide
ITIC	3,9-bis(2-methylene-(3-(1,1-dicyanomethylene)-indanone)-5,5,11,11-tetrakis(4-hexylphenyl)-dithieno[2,3-d:20,30-d']-s-indaceno[1,2-b:5,6-']
ITO	Indium tin oxide
MoO_3	Molybdenum trioxide
P3HT	poly(3-hexylthiophene-2,5-diyl)
PBDB-T	poly[(2,6-(4,8-bis(5-2(ethylhexyl)thiophen-2-yl)-benzo[1,2-b:4,5-b']dithiophene))-alt-(5,5-(1',3'-di-2-thienyl-5',7'bis(2-ethylhexyl)benzo[1',2'-c:4',5'-c']dithiophene-4,8-dione)]
PbS	Lead sulfide
$PC_{71}BM$	[6,6]-phenyl-C71-butyric acid methyl ester
PTAA	poly-[bis-(4-phenyl)-(2,4,6-trimethylphenyl)-amine
PTB7	poly[[4,8-bis9(2-ethylhexyl)oxy]benzo[1,2-b:4,5-b']dithiophene-2,6-diyl][3-fluoro-2-[(2-ethylhexyl)carbonyl]thieno[3,4-b]thiophenediyl]
SeIn	3,9-bis(2-methylene-(3-(1,1-dicyanomethylene)indanone))- 4,4,9,9-tetrakis(3-((2-ethyl hexyl)-oxy)phenyl)diseleno[2,3-d:2,3-d]-s-indaceno[1,2-b:5,6-b]dithiophene

SeOut	3,9-bis(2-methylene-(3-(1,1- dicyanomethylene)indanone))-4,4,9,9-tetrakis(3-((2-ethyl hexyl)oxy)-phenyl)dithieno[2,3-d:2,3-d]-s-indaceno[1,2-b:5,6-b]-diselenophene
Y6	2,2'-((2Z,2'Z)-((12,13-bis(2-ethylhexyl)- 3,9-diundecyl-12,13-dihydro-[1,2,5] thiadiazolo[3,4-e]thieno [2,3":4',5']thieno [2',3':4,5]pyrrolo[3,2-g]thieno[2',3':4,5] thieno[3,2-b]indole-2,10-diyl)bis(methanylylidene)) bis(5,6-difluoro-3-oxo-2,3- dihydro-1H-indene-2,1-diylidene))dimalononitrile
ZnO	Zinc oxide

Physical constants

ϵ_0	Vacuum permittivity (8.85×10^{-12} F m^{-1})
$\hbar$	Reduced Planck's constant (1.05×10^{-34} J s)
k_B	Boltzmann constant (1.38×10^{-23} J K^{-1})
q	Elementary charge (1.60×10^{-19} C)
h	Planck's constant (6.63×10^{-34} J s)

Contents

Abstract **iv**

Acknowledgements **v**

1 Introduction **1**

1.1 Motivation 1

1.2 Photovoltaic materials 2

1.3 Photophysics in photovoltaic semiconductors 2

1.3.1 The quantisation of energy 2

1.3.2 Electronic structure in semiconductors 4

1.3.3 Optical transitions 5

1.3.4 Excitons 7

1.3.5 Energy transfer 9

1.3.6 Charge transfer 11

1.3.7 Charge transport and extraction 16

1.3.8 Recombination 17

1.4 Types of photovoltaic materials in this thesis 19

1.4.1 Nanocrystals 20

1.4.2 Organic semiconductors 21

1.4.3 Light-harvesting in cyanobacteria 24

1.5 Outline of this thesis 34

2 Experimental Details **36**

2.1 Sample fabrication 36

2.1.1 Film fabrication 36

2.1.2 Optoelectronic device fabrication 37

2.1.3 Cyanobacteria suspension sample preparation 38

2.1.4 Biophotovoltaic devices 38

2.2 Steady-state measurements 38

2.2.1 Ultraviolet-visible absorption spectroscopy 38

2.2.2 Photoluminesence spectroscopy 40

2.2.3 Incident photon-to-electron conversion efficiency 41

2.3 Time-resolved spectroscopy 44

2.3.1 Basic principles 44

2.3.2 Experimental setup for 100 fs time resolution 45

2.3.3 Interpretation of spectra 46

2.3.4 Analysis of spectra 48

2.3.5 Transient absorption spectroscopy with sub-10 fs pulses 50

2.4 Time-correlated single photon counting 52

3 Regioisomeric molecular tuning of small molecule-based OPVs 54

3.1 Context and motivation 54

3.1.1 Conformational twisting in a push-pull small molecule 55

3.1.2 Chalcogen substitution in an example non-fullerene acceptor 58

3.2 Experimental details 60

3.2.1 Sample preparation 60

3.2.2 Steady-state absorption spectroscopy 60

3.2.3 Transient absorption spectroscopy 61

3.3 Results and discussion 61

3.3.1 Conformational twisting in a push-pull small molecule 61

3.3.2 Chalcogen substitution in an example non-fullerene acceptor 66

3.4 Conclusions 71

4 Correlating photoinduced dynamics and stability in photovoltaic materials 72

4.1 Context and motivation 72

4.1.1 Photoprotection in fullerene-based solar cells 73

4.1.2 The relationship between stability and charge trapping in $AgBiS_2$ quantum dot solar cells 76

4.2 Experimental details 79

4.2.1 Sample preparation 79

4.2.2 Steady-state absorption characterisation 79

4.2.3 Transient absorption spectroscopy 79

4.3 Results and discussion 80

4.3.1 Photoprotection in fullerene-based solar cells 80

4.3.2 The relationship between stability and charge trapping in $AgBiS_2$ quantum dot solar cells 84

4.4 Conclusions 90

5 Time-resolved spectroscopic studies of photosynthesis in cyanobacteria 92

5.1 Context and motivation 92

5.1.1 Comparison of the photosynthetic processes within biophotovoltaic devices *in vitro* and cyanobacteria cells *in vivo* 92

5.1.2 The ultrafast photoinduced dynamics of photosynthesis *in vivo* 95

5.2 Experimental details 97

5.2.1 Sample preparation 97

5.2.2 Steady-state absorption spectroscopy 97

5.2.3 Steady-state photoluminescence spectroscopy 97

5.2.4 Time-correlated single photon counting 97

5.2.5 Incident photon-to-electron conversion efficiency 97

5.2.6 Transient absorption spectroscopy 98

5.3 Results and discussion 98

5.3.1 Comparison of the photosynthetic processes within biophotovoltaic devices *in vitro* and cyanobacteria cells *in vivo* 98

5.3.2 The ultrafast photoinduced dynamics of photosynthesis *in vivo* 105

5.4 Conclusions 111

6 Conclusions and Outlook **113**

6.1 Conclusions 113

6.2 Outlook 115

6.2.1 Maximising OPV performance 115

6.2.2 Towards operationally stable organic solar cells 116

6.2.3 Ultrafast spectroscopic techniques for investigating photosynthesis 117

A $PC_{70}BM$ absorption **119**

B $AgBiS_2$ absorption **120**

List of Tables

4.1 Time constants for the PIA centres of mass shift, and the percentage decrease of the time constant of the degraded device relative to the pristine device 89

5.1 Time constants for PL quenching in cyanobacteria cells in solution and those immobilised onto an electrode to afford a BPV device. 104

List of Figures

1.1 Atomic orbitals (top) and molecular orbital diagram for the C=C bond in ethene between two CH_2 fragments. 5

1.2 Jablonski diagram summarising electronic (straight lines) and vibrational (wavy lines) transitions induced by absorption of a photon. S_0, S_1 and S_2 represent the ground state, first singlet excited state and second singlet excited state respectively. T_1 and T_2 depict the first and second triplet state. 7

1.3 The typical nature of excitons in organic and inorganic semiconductors. 9

1.4 Schematic diagrams of radiative, Förster and Dexter energy transfer. Straight lines and wavy lines represent radiative and non-radiative processes respectively, while curved arrows depict transfer of electrons. 10

1.5 Plots summarising the key principles of Marcus theory and Onsager theory. . . . 12

1.6 Delocalised π-electron cloud (right) above and below molecular plane of electron-rich benzodithiophene due to conjugation of p-orbitals (left). Lone pair orbitals on S are not involved in conjugation. 22

1.7 Schematic of exciton generation, diffusion to the donor:acceptor interface, charge transfer state formation and charge separation in a typical organic donor:acceptor blend after excitation by a photon. 23

1.8 Cyanobacteria, PSI and PSII embedded in a thylakoid membrane, with the photosynthetic mechanism illustrated. 25

1.9 The structure of the PSII reaction centre annotated with the two charge separation pathways. Red, purple and orange (blue, teal and green) pigments represent the special pair chlorophyll, branched chlorophyll and pheophytin molecules respectively on branch D_1 (D_2). 33

2.1 Schematic for a typical absorption spectrophotometer. 39

2.2 Schematic diagram of a photoluminescence spectrometer. 41

2.3 Schematic diagram of IPCE setup. e^-=electrons in electrolyte solution. 41

2.4 Photocurrent spectra collected in the optimisation process of the IPCE setup for $BiVO_4$ using +0.5 V of applied bias and a 100 ms (a), 200 ms (b) or 2 s (c) time constant. d): Normalised photocurrent spectra for all time constants plotted on a log scale y-axis in order to emphasise the small signal at 700-800 nm. 44

2.5 Schematic diagram of a TAS experimental setup. BS=beam splitter. OPA=optical parametric amplifier. DS=delay stage. FL=focussing lens. BG=broadband generation. NDF=neutral density filter. OF= optical fibre. 46

2.6 Photoinduced processes occurring on pump excitation in a TAS measurement, with typically detected signals represented by straight arrows. 48

2.7 Diagram illustrating the origin of oscillations in time-resolved spectra and the reconstruction of the vibrational spectrum by Fourier transformation. Wavelength of photoinduced absorption (PIA) is given by λ. 51

2.8 Schematic diagram of a TCSPC experimental setup. 52

3.1 Structures of BTCN-M (left) and BTCN-O (right), with octyl chains (represented by **R** for figure clarity) at meta and ortho positions to each other respectively. . 56

3.2 Structure of the commonly employed NFA molecule, ITIC. 59

3.3 Structures of ITIC derivatives SeIn (left) and SeOut (right). 59

3.4 Spectra at selected time points for BTCN-M (a) and BTCN-O (d) and blends (b, c and e, f respectively) following 710 nm excitation. The greyed out region at 700 nm is included to remove pump scattering for clarity. Figure adapted from ref. 214 with author's permission. 61

3.5 GA-reconstructed spectra featuring excitons (red) and charges (black) for BTCN-M (a), BTCN-O (d) and blends (b, c and e, f respectively). Amplitudes are normalised to the maximum of each spectrum. Figure adapted from ref. 214 with author's permission. 63

3.6 Kinetics of photophysical components in BTCN-M (a), BTCN-O (d) and blends (b, c and e, f respectively). The factor of normalisation of the charge component is included for amplitude comparison. The red trace describes exciton decay while the black trace shows charge dynamics. Multiexponential fits are included as a guide to the eye. Figure adapted from ref. 214 with author's permission. . . 64

3.7 TA spectra (negative signals) following 725 and 720 nm excitation of SeIn (top) and SeOut (bottom) respectively, both blended with PBDB-T, shown alongside the visible absorption and photoluminescence spectra (positive signals) of the respective materials. Adapted from ref. 62 with author's permission. 66

3.8 Spectra of excitonic and charge components extracted by global analysis for the PBDB-T:SeIn (left) and PBDB-T:SeOut (right) blends. 68

3.9 Kinetics associated with the exciton and charge components for each of the PBDB-T:SeIn and PBDB-T:SeOut blends as extracted by global analysis, with corresponding exponential fits as solid traces. 69

3.10 a) Cartoon representing how smaller domains (SeIn, blue, left) give rise to faster charge separation lifetimes relative to more crystalline larger domains (SeOut, red, right) when blended with PBDB-T (green polymer chains). b) Schematic diagram of dynamic processes with their characteristic timescales probed by TAS and extracted by GA for SeIn (blue) and SeOut (red) blends. 70

4.1 Different ETL and HTL components affording the four different devices studied. 77

4.2 Normalised GA-derived spectra (left) and associated kinetics (right) for DRCN5T excitons (top) and charges (bottom) present in the DRCN5T:$PC_{70}BM$ blend extracted from TA spectra collected following 700 nm excitation (150 nJ) for varying extents of degradation. Only one exponential fit is included in each of the kinetic traces for figure clarity, taken from analysis of the pristine blend data and shown as black solid lines. 80

4.3 Time constants of the photophysical processes occurring in the studied blend following 700 nm excitation, determined by monoexponential fitting of the kinetic traces in figure 4.2, plotted as a function of degradation. 82

4.4 TA spectrum of the 250 nm pump experiment (150 nJ) with $PC_{70}BM$ and DRCN5T neat spectra at early times superimposed for clarity. 82

4.5 Normalised GA-derived spectra (left) and associated kinetics (right) for the TA spectrum measured using a 250 nm pump pulse to selectively excite the fullerene. Kinetics are plotted as moving averages with associated errors shown. 83

4.6 a-e): TA spectra for neat $AgBiS_2$ films at increasing extents of degradation, following excitation with a 700 nm pump (50 nJ). f): Normalised kinetics of PIA for each film. 85

4.7 a): Fluence dependence kinetics and exponential fits of PIA in pristine film. b): Spectral centre of mass as a function of degradation for early time delays vs late time delays. Fits are included as a guide to the eye to demonstrate the centre of mass trajectory. 86

4.8 TA spectra for $AgBiS_2$ devices (pumped at 700 nm) with different hole and electron transport layers, both pristine (left) and following 8 hours of degradation under light and O_2 (right). 88

4.9 Spectral centre of mass across the PIA region for each device as a function of time, as well as solid lines showing monoexponential fits used to quantify the blueshift. 89

5.1 a): Generation of photocurrent by continuous-wave illumination (675 nm, 255 μWcm^{-2}) switched on at 30 s, 90 s and 150 s, and switched off at 60 s, 120 s and 180 s. A bare electrode control measurement is also shown for evidence of cyanobacteria contribution. b): Linear relationship between photocurrent and light intensity. 99

5.2 a) Raw IPCE spectra for isolated PSII and Synechocystis cells. (b) Normalised IPCE spectra for isolated PSII and Synechocystis cells, as well as absorption spectra for Synechocystis cells in suspension. 100

5.3 Photocurrent detected with 675 nm excitation for a BPV comprising *in vivo* Synechocystis cells, as a function of laser modulation frequency given by an optical chopper. 102

5.4 Steady-state photoluminescence spectra of a) Synechocystis cells in suspension and b) Synechocystis cells immobilised onto electrodes. c) Steady-state photoluminescence spectrum of Synechocystis cells in suspension following 635 nm excitation. b) PL quenching dynamics of cells in solution and those wired to an electrode to afford a BPV device. IRF = instrument response function. 104

5.5 a):Transient absorption spectrum of cyanobacteria cells in suspension dispersed in MES buffer solution following 440 nm pump excitation (50 nJ, 100 fs time resolution). 105

5.6 a): Transient absorption spectrum for cyanobacteria cells *in vivo* in suspension dispersed in MES buffer solution with a 395-420 nm pump (320 μW, $\sim$12 fs time resolution). b) The kinetics extracted for the PIA and 695 nm GSB feature. . . 107

5.7 Spectra (a) and kinetics (b) for the two photophysical components extracted from the TA spectrum in figure 5.6 using global analysis. 108

5.8 Energy level diagram of the photophysical model proposed to rationalise the sub-picosecond dynamics observed in TA measurements. 109

5.9 Frequency-domain data extracted by Fourier transform of the sub-picosecond TA spectrum in figure 5.6 to afford excited state vibrational spectra of *in vivo* cyanobacteria cells from three different measurements to demonstrate reproducibility. 110

A.1 Steady-state near-IR absorption spectrum of neat $PC_{70}BM$ film. 119

B.1 Steady-state UV-visible absorption spectra of neat $AgBiS_2$ films at varying durations of exposure to light and O_2. 120

Chapter 1

Introduction

1.1 Motivation

It is no revelation that the current energy infrastructure needs uprooting, with over 80 % of the global demand, which currently exceeds 15 TW annually, being supplied by fossil fuels.[1] Energy-related CO_2 emissions flattened at 33 Gt in 2019 due to the increasing contribution from renewable sources. However, overall we continue on a trajectory that is predicted to displace 187 million people worldwide by the year 2100 due to land loss from rising sea levels.[2] It is therefore not enough to plateau in the energy generation industry, which alone accounts for around 70 % of total CO_2.[3] The role of renewables must surge significantly in order to actively drag the total down. To this end, it is intuitive to turn to the most ubiquitous and predictable energy source available: the Sun.

The Earth receives 120,000 TW of solar energy to its surface on average, which satisfies the global annual energy demand in less than one hour.[4] With 2018 seeing solar energy generation exceeding a 500 GW capacity and a further 500 GW anticipated by 2023, the present moment marks an exciting step in the career of solar power as it enters the league of terawatt sources.[5]

1.2 Photovoltaic materials

In actual fact, solar power is not a futuristic concept but a historical one: the photovoltaic effect was first demonstrated in 1839, at the midpoint on the timeline between the debut of electrical batteries and Edison's lightbulb.[6–8] The first solar cell came much later in 1954 with a power conversion efficiency (PCE) of just 6 % and was composed of crystalline silicon, which monopolises the market to this day with commercial efficiencies of around 24 %.[9,10] While the rapid growth in the performance of these devices appears promising, the theoretical limit of solar cell efficiency at 33.7 % grants little room for improving their efficiency relative to the unsustainable yet cheap resources that power our grid.[11] It is thus clear that we need to reduce the cost of fabricating these devices in order to compete with the high power-to-cost ratios exhibited by fossil fuels. To achieve this, the photovoltaic field is increasingly turning to new alternatives due to their flexibility and light weight as well as low processing and application costs compared to silicon photovoltaics.

1.3 Photophysics in photovoltaic semiconductors

In order to examine the properties of photovoltaic materials which influence their performance and stability, it is necessary to first discuss the physical theory behind their photoinduced behaviours. This section discusses the basic photophysics determining the electronic structure and properties of semiconductors and thus outlines the systems at play when photons are harnessed by matter to generate electrical current.

1.3.1 The quantisation of energy

The energetic and electronic states of any quantum system are constrained to take discrete values as a consequence of the wave-particle duality of the electrons which carry electrical charge. The de Broglie equation illustrates this duality by describing wavelength λ as a function

of a particle's mass m and velocity v:

$$\lambda = \frac{h}{mv} = \frac{h}{p} \tag{1.1}$$

where h is Plank's constant and p is the particle's momentum. The Heisenberg uncertainty principle relates the product of the standard deviations associated with the position and momentum of a particle to a constant.[12] This hence asserts that it is not possible to precisely define a particle's position and momentum simultaneously; a greater precision in one value renders a greater uncertainty associated with the other. It is therefore more prudent to describe electrons by a wavefunction: an equation expressing the region of space where the electron is likely to be found.

The wavefunction of a single electron is described according to the "particle in a box" model which considers the electron as confined to a one-dimensional box of length L. The amplitude of the wave inside the box describes the probability of the electron being found at a given point in space and the derivative of the wavefunction gives its energy.[13] The boundaries of the box are defined by nodes at which the wave has an amplitude of zero and therefore the total probability of finding the electron inside the box must be unity. Likewise, the potential energy at the walls of the box is infinitely large while the potential energy across the inside of the box is zero. The wavefunction must therefore vanish at the walls of the box and its amplitude must be continuous inside the box (i.e. its momentum must be continuous). These conditions establish that the equation of the wavefunction is restricted to take certain allowed forms and ultimately arise at an equation to prescribe the energy of the particle:

$$E_n = \frac{\hbar^2 \pi^2 n^2}{2mL^2} \tag{1.2}$$

Where $\hbar$ is the reduced Planck's constant, m is the mass of the particle and n is the principal quantum number of the particle, which must be an integer. It therefore follows that the particle's energy may only take discrete values that are spaced by a multiple of the constant for a given particle in a given box, with the spacing equal to $\hbar^2\pi^2/2mL^2$. The quantisation of energy therefore arises, restricting the energy of the electron to discrete energy levels determined

by the quantum number of the particle.

1.3.2 Electronic structure in semiconductors

Of course, the particle in a box model describes an isolated electron and thus is far too simple to express the complex electronic structure of atoms and molecules. Atomic orbitals (AOs) denote the one electron wavefunctions representing the region in space in the atom at which it is likely to find an electron. For molecules the wavefunctions are expressed as linear combinations of these AOs, affording molecular orbitals (MOs) which arise when AOs overlap in a molecule.

All orbitals intrinsically contain positive and negatively phased lobes. Hence the combination of AOs can result in either constructive or destructive interference, giving rise to bonding and antibonding orbitals respectively. The constructive sharing of electron density in bonding MOs results in a lower energy MO than the high energy destructive antibonding MO. Consequently, the energy of two overlapping AOs affords a "splitting" of the energy, placing the energy levels of the bonding and antibonding orbitals above and below the relevant AOs, respectively. This results in a general structure of the electronic energy levels that is illustrated in figure 1.1.

An example of a molecular bonding diagram for a carbon bond is also shown in figure 1.1. The valence electrons involved in carbon bonds reside in the p orbitals. These orbitals can achieve overlap by head-on alignment, denoted a σ MO, or by parallel alignment such that the electron density is shared on an axis perpendicular to the lobes, realising a π MO. Depending on the relative phase of the relevant orbital lobes, both of these families of MOs can be either bonding or antibonding, symbolised as σ/π or $\sigma*/\pi*$ respectively.

A pertinent consideration is that there must be an equal number of MOs as there are AOs. This rule arises from the fact that two overlapping AOs will unwaveringly afford exactly one bonding and one antibonding MO. For relatively small molecular systems, such as an organic molecule, these MOs are sufficiently few that their spacing is significant and the electronic structure remains restricted to discrete levels. However, for bigger systems such as a large inorganic crystalline lattice, the infinitely high quantity of these discrete energy levels renders them

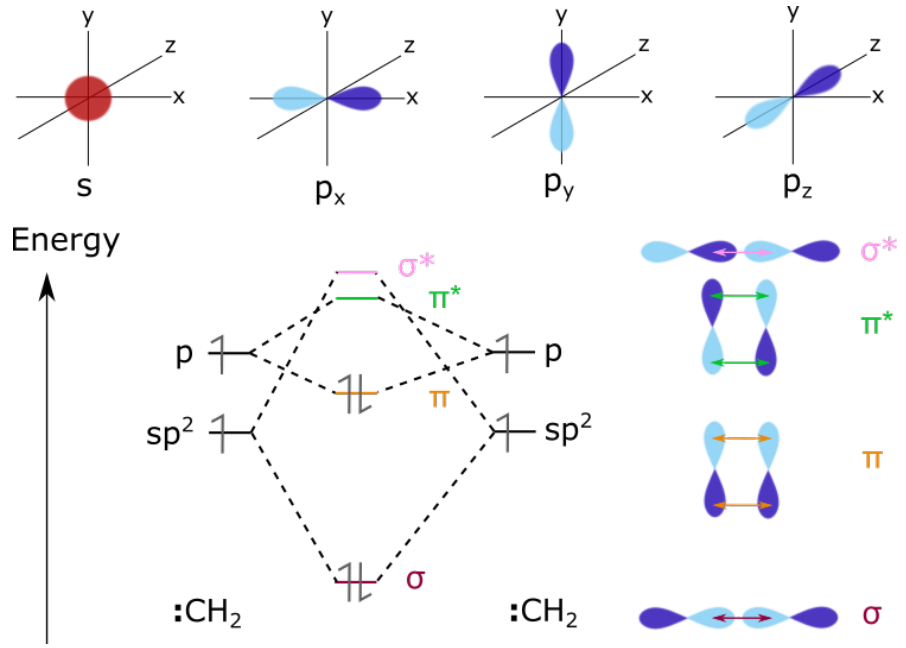


Figure 1.1: Atomic orbitals (top) and molecular orbital diagram for the C=C bond in ethene between two CH_2 fragments.

indistinguishable on the energetic scale of the whole lattice. This effect causes the electronic structure of crystalline systems to instead be represented by a "density of states", generally described as "bands" of continuous MO energy levels as opposed to distinct MOs.[14] The Aufbau principle asserts that electrons must fill the lowest energy states before occupying higher-lying energy levels.[13] In molecular systems, this determines that the electrons fill up the orbitals in increasing energy to the highest occupied molecular orbital (HOMO), with the lowest unoccupied molecular orbital (LUMO) lying consecutively above it. In the band structure of crystal systems, the bands are differentiated as the valence band and the conduction band for the continuum of filled and empty states, respectively. When the HOMO-LUMO energy gap or the gap between the valence band and conduction band, termed band gap or E_g, is below 3 eV then the material is termed a semiconductor.

1.3.3 Optical transitions

Satisfaction of the Aufbau principle occurs on the assumption that the system is in its lowest possible energy state or "ground state". However, an atom or molecule may absorb a photon resulting in the transition of the system from the ground state to a higher-lying excited state.

An electron is thus excited from the HOMO or valence band to the LUMO or conduction band. The energy of the incident photon must be resonant with the energy of the band gap in order to be absorbed. Furthermore, in order for a transition to be allowed, the spin or angular momentum of the electrons in the system must be conserved.

Excited states resulting from a transition in which spin is conserved are termed singlet states while transitions which do not conserve the overall spin of the system are technically forbidden and give rise to triplet states. However, they are in fact not truly forbidden and are weakly allowed transitions which occur with a very low probability compared to technically allowed transitions. As a result, absorption by the ground state typically occurs with excitation to the first singlet excited state, and triplet states can be accessed via the singlet excited state in a processed termed intersystem crossing.

Following excitation from the ground state, denoted S_0, to the first excited singlet state, S_1, there are a number of photoinduced electronic processes that can ensue which are summarised in the Jablonski diagram in figure 1.2. The system can relax back down to the ground state, resulting in the excess energy being dissipated either by radiative or non-radiative decay. Radiative decay encompasses both fluorescence and phosphorescence which refer to emission from excited singlet and triplet states respectively. Kasha's rule states that emission occurs with significant quantum yield exclusively from the lowest lying state of a given multiplicity.[15] Hence the S_1 state is assumed to account for all fluorescence while phosphorescence is exhibited only from the first excited triplet state, T_1.

The excited states may also absorb further photons to yield higher-lying excited states $S_2 \ldots S_n$ or $T_2 \ldots T_n$ (where n is an integer), in a process termed excited state absorption. Furthermore, the ground state may actually absorb higher energy photons of $E_{h\nu} \geq nE_g$ (where $n = 2,3,4\ldots$) however the system will then undergo rapid internal conversion to S_1. The process of internal conversion embodies transfer from one electronic state to another state of the same multiplicity. The excited state may also undergo transfer to another excited state of different spin, termed intersystem crossing. The intrinsically spin-forbidden nature of intersystem crossing and phosphorescence processes renders their rates far slower than the spin-conserving processes

of internal conversion and fluorescence.

Each electronic state is coupled to a manifold of vibrational states and thus the first photoinduced process to occur following excitation to an excited state is vibrational relaxation to the lowest-lying vibrational state within the electronic state. The excess energy from the vibrational relaxation is dissipated as heat. Non-radiative decay can occur via vibrational relaxation within a given electronic state or via the coupling of an electronic state to a vibrational state within the manifold of a lower-lying electronic state. This allows the system to relax to lower-lying electronic states without emission of a photon and instead with the dissipation of heat. This is understood to be a major consideration in the possible routes by which photovoltaics may suffer energy loss and thus detriment their efficiency.

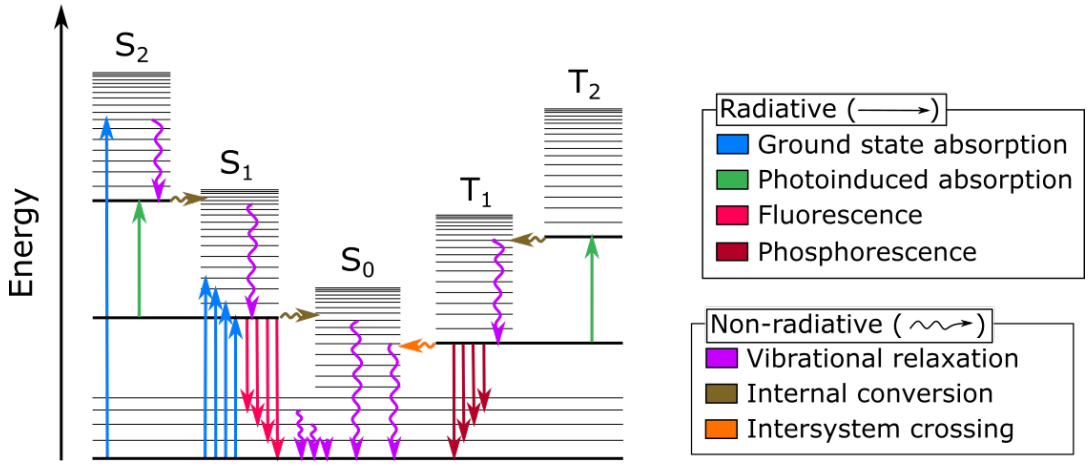


Figure 1.2: Jablonski diagram summarising electronic (straight lines) and vibrational (wavy lines) transitions induced by absorption of a photon. S_0, S_1 and S_2 represent the ground state, first singlet excited state and second singlet excited state respectively. T_1 and T_2 depict the first and second triplet state.

1.3.4 Excitons

On photoexcitation of a system from the ground state to the excited state, an electron is promoted across the band gap from the HOMO to the LUMO or from the valence band to the conduction band in organic and inorganic semiconductors, respectively. This also leaves a positive charge, denoted a "hole", on the HOMO or valence band. The Coulombic attraction between the electron and hole bind them to each other and collectively both charges together

with their electrostatic attraction are termed an "exciton". The distance between the electron and hole is called the Bohr radius, R_{ex}:

$$R_{ex} = \frac{4\pi\epsilon_0\epsilon_r\hbar}{\mu_{eh}q^2} \tag{1.3}$$

Where μ_{eh} is the reduced mass of the electron-hole pair, q is the electron charge, ϵ_0 is the vacuum permittivity and ϵ_r is the relative permittivity, a measure of the ratio of the electric permeability of the material to that of a vacuum. This value therefore quantifies the factor by which the electric field between two point charges is decreased relative to a vacuum.

The proper operation of a photovoltaic material requires the electrical current to be collected and therefore the overall neutral exciton is required to separate into free charges in order for photocurrent to be generated. This necessitates the provision of a sum of energy greater than the Coulombic binding energy, E_B, which can be calculated as a function of the Bohr radius by rearrangement of equation 1.3:

$$E_B = \frac{q^2}{4\pi\epsilon_0\epsilon_r R_{ex}} \tag{1.4}$$

It follows that the exciton binding energy is a function of the relative permittivity of the material. As discussed in section 1.3.2, the electronic structures of organic and inorganic semiconductors are vastly different, which in turn establishes a stark contrast in the relative permittivity of organic versus inorganic semiconductors. Organic molecules typically exhibit a small relative permittivity and hence a large exciton binding energy, manifesting tightly bound electrons and holes with small excitons that are localised to molecular units. Such excitons are known as Frenkel excitons. Conversely, inorganic semiconductors usually exhibit a large relative permittivity compared to that of organic semiconductors, affording large Bohr radii and weakly bound excitons termed Wannier-Mott excitons. The binding energy of excitons in inorganic materials generally is so low that they undergo separation spontaneously at room temperature, giving rise to large populations of free charge carriers and thus efficient photocurrent generation. Figure 1.3 illustrates the difference between Frenkel and Wannier-Mott excitons in terms of how they percolate in space.

As the excitons in organic semiconductors do not readily separate at room temperature, the exciton binding energy must be offset in order to achieve photocurrent generation. An exciton will travel through the material as a tightly bound entity by hopping between molecules until it reaches an interface with an electron-accepting material in order for charge separation to be instigated.

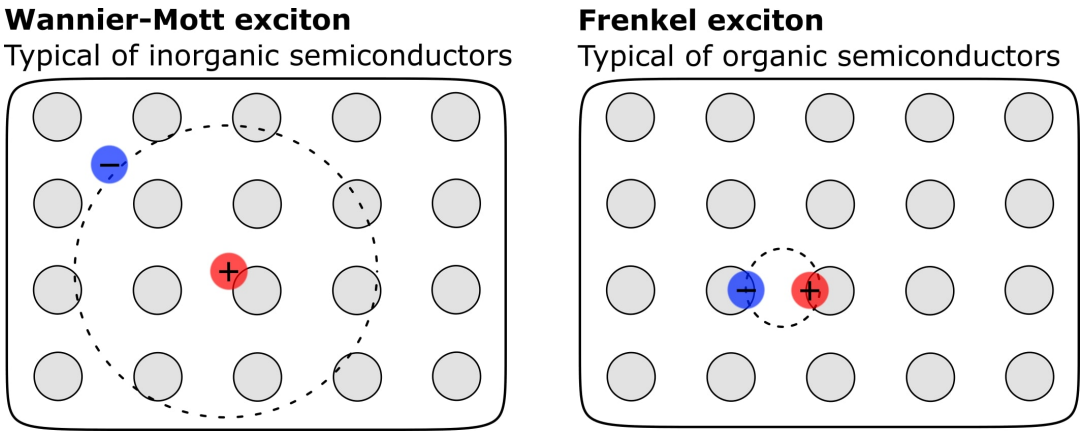


Figure 1.3: The typical nature of excitons in organic and inorganic semiconductors.

1.3.5 Energy transfer

Organic photovoltaics (OPVs) require that an exciton diffuses through the material to meet an interface between two domains in order to generate photocurrent. In the event that an exciton does not reach this domain boundary within its lifetime (before recombination occurs), the absorbed energy will be wasted. Typically, the diffusion lengths of singlet excitons in OPVs tend to be on the order of tens of nanometres,[16] and the bulk heterojunction morphology was introduced to facilitate the separation of charges within this distance.[17] This is explained in more detail in section 1.4.2.

The process of exciton diffusion requires energy transfer (ET) where the excitation energy is relocated from the energy donor site to the energy-accepting site, resulting in a ground state donor and an exciton on the acceptor. In general, the simplest mechanism of this process entails radiative emission of a photon from the donor molecule that is absorbed by the acceptor molecule, resulting in relaxation of the donor to its ground state and formation of an exciton on

the acceptor. This process therefore requires a strong overlap of the donor's emission spectrum and acceptor's absorption spectrum, where the probability of an ET event scales with the spectral overlap integral of these two functions.

However, ET in OPVs usually occurs by one of the two single-step non-radiative mechanisms whereby the donor relaxes from its excited state to the ground state, inducing synchronous excitation of the acceptor via a direct coupling.[18] The three possible energy transfer mechanisms are summarised schematically in figure 1.4.

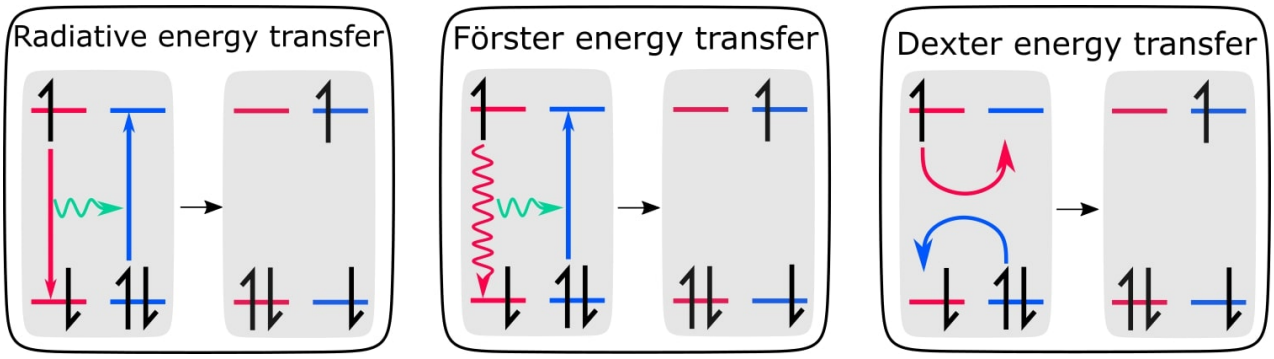


Figure 1.4: Schematic diagrams of radiative, Förster and Dexter energy transfer. Straight lines and wavy lines represent radiative and non-radiative processes respectively, while curved arrows depict transfer of electrons.

For singlet excitons, Förster resonance energy transfer (FRET) takes place through space via intermolecular dipole-dipole coupling and can be observed significantly for ranges up to 5 nm.[19] FRET vaguely resembles radiative energy transfer (RET) in that a virtual photon is emitted from the excited state donor molecule, D*, and is instantaneously absorbed by the ground state acceptor molecule A, to afford D and A*. However, the distinction for FRET compared to RET is underpinned by the fact that the coupling between D and A occurs via the weak Coulombic interaction between the resonant dipoles on the two molecules. Hence FRET does not actually entail the physical exchange of a photon, while it does maintain the prerequisite for spectral overlap of donor emission and acceptor absorption. As implied by its dependence on dipole-dipole interactions, the relationship between the rate of FRET and donor-acceptor distance reflects that of London dispersion forces, being inversely proportional to the sixth

power of the donor-acceptor separation, r:

$$k_{FRET} = k_D(\frac{R_0}{r})^6 \tag{1.5}$$

Where R_0 is the Förster radius and k_D is the rate of decay of the donor.

In the case of triplet excitons, transition between a triplet excited state on the donor, D_3*, and its singlet ground state, D_1, is classically spin-forbidden. As such, triplet excitons are unable to undergo FRET and instead transfer energy via the Dexter mechanism. In this case, electrons are physically exchanged between donor and acceptor to afford the singlet ground state D_1 and excited triplet state A_3*, therefore achieving overall conservation of spin. This mechanism thus forgoes the necessity for overlap of absorption and emission spectra and instead requires significant overlap of the wavefunctions of the relevant orbitals involved in the exchange. It follows that far stronger coupling is required and that Dexter ET is observed only at very short ranges of 0.1 – 1 nm, exhibiting approximately exponential depletion at increasing donor-acceptor distances.[2,20]

1.3.6 Charge transfer

Once an exciton is formed following absorption of a photon, its subsequent dissociation into free charges is critical for efficiency in the photovoltaic process.[21–23] As discussed in section 1.3.4, the exciton binding energy in organic semiconductors tends to be relatively high, typically reaching around 0.1-0.5 eV[24] compared to 0.01 eV for silicon.[25] The lowest binding energies found for organic systems were calculated to be at approximately 0.05 eV which still far exceeds the thermal energy at room temperature (0.026 eV).[26,27]

When the exciton binding energy exceeds the thermal energy, the electron and hole may be too tightly bound to separate into free charges and the competitive process of exciton recombination becomes significant.[24] Contributions to the binding energy include the Coulombic attraction between the electron and hole as well as electron-electron and electron-lattice interactions.[28] For the latter, the formation of polarons gives rise to localised relaxation of the excited state

which contributes to the strong exciton binding energy in organic semiconductors compared to inorganic counterparts (in which the rigid crystalline structure means that this lattice deformation does not occur to such an extent). Therefore, the consideration of exciton dissociation is crucial in organic semiconductors, for which there are two fundamental theories which are widely accepted. These will be discussed in depth in the subsequent sections and are illustrated in figure 1.5.

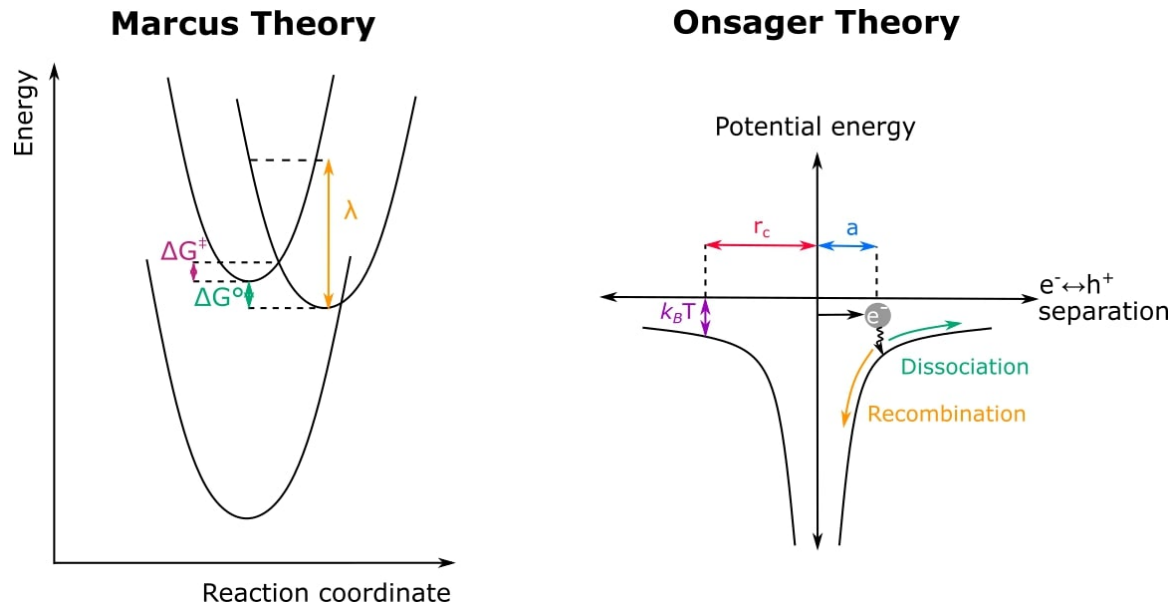


Figure 1.5: Plots summarising the key principles of Marcus theory and Onsager theory.

Marcus theory

Marcus theory, now universally applied for the understanding of charge transfer in organic photovoltaics[29–34] was suggested in 1956 shortly after the realisation of the first solar cell.[35] It refers to the excitonic state and the charge transfer (CT) state as reactant and product states respectively and considers their potential energy surfaces (PESs) to be harmonic oscillators on which the nuclei of each state may propagate. The Franck-Condon principle asserts that electron transfer occurs at a rate far faster than motion of nuclei such that electron transfer can be assumed to occur with no change in the relevant nuclear coordinates. It follows that electron transfer may only take place at an intersection between the PESs in order to satisfy the Franck-Condon principle; hence the intersectional coordinate on the CT state PES defines

the energy that the reactant state is required to reach in order to achieve electron transfer. Electron transfer is thus associated with an activation energy barrier, $\Delta G^{\ddagger}$, which must be overcome in order for the process to be energetically possible:

$$\Delta G^{\ddagger} = \frac{(\lambda + \Delta G^{\circ})^2}{4\lambda} \tag{1.6}$$

Where $\Delta G^{\ddagger}$ is a function of Gibbs free energy, ΔG°, and reorganisation energy λ: the energy required in order for the reactant state and its solvent lattice to reach the nuclear geometry of the product state. From equation 1.6, it can be seen that in the regime where $-\Delta G^{\circ} < \lambda$, as ΔG° becomes less negative the activation energy decreases such that the rate of electron transfer increases. This is until $-\Delta G^{\circ} = \lambda$ at which point the activation energy reaches its minimum and the rate of electron transfer achieves its maximum. Surpassing this point, where $-\Delta G^{\circ} > \lambda$, the activation energy increases thus decreasing the rate of electron transfer. This is denoted the inverted region, the boundaries of which are governed by λ.

From this activation energy, the rate constant k_{ET} can be derived from the Arrhenius relation to be:

$$k_{ET} = \frac{2\pi}{\hbar\sqrt{4\pi\lambda k_B T}} V^2 exp(-\frac{(\lambda + \Delta G^{\circ})^2}{4\lambda k_B T}) \tag{1.7}$$

Where the pre-exponential term captures the reactant and product states' electronic coupling, dependent on the overlap of the donor and acceptor wavefunctions.

While Marcus theory has been extensively demonstrated to account for experimental results in organic blends,[36] modifications must be taken into account for some systems. For example, in solid films the energy levels should be considered as a continuous band of states as opposed to discrete levels. This requires the integration of equation 1.7 over the density of possible states where previously the equation treated discrete acceptor states. A further expansion of Marcus theory is underpinned by the Marcus-Levich-Jortner equation which explicitly accounts for the influence of vibrational energy levels and the subsequent possibility of tunnelling and its effects on electron transfer rate,[37] which has also been applied to organic photovoltaics.[24] Overall, while some disputes have arisen suggesting that excitons are directly coupled to separated

charges such that charge transfer states should not be considered,[38] Marcus theory is widely employed for the modelling of charge transfer in organic semiconductors.

Onsager theory

Another model that has been extensively applied to the study of charge separation from the CT state in organic photovoltaics[39–43] is Onsager theory.[44] As mentioned above, dissociation of the Coulombically bound electron-hole pair into free charge carriers can be hindered in organic materials by the high exciton binding energy. If the exciton does not dissociate within the lifetime of the CT state then geminate recombination will occur, where the hole and electron from the same exciton will recombine and the ground state will be regenerated. The energy lost by relaxation from the excited state to the ground state will be emitted and this is a major consideration in the discussion of efficiency and loss thereof in OPVs. The competition between charge separation and geminate recombination was first modelled by Onsager by derivation of the probability of the exciton overcoming the binding energy and separating into free charges.

The model describes photoinduced formation of a localised hole and a "hot" electron which subsequently thermalises at some distance, the thermalisation length a, from the hole location. This localised hole and thermalised electron pair are together denoted the CT state. The competition between recombination of the two charges and their separation is determined by the Coulombic attraction binding them in this CT state. Onsager introduced a threshold distance for dissociation beyond which the Coulombic attraction is exceeded by the thermal energy k_BT, denoted the Coulomb capture radius r_c:

$$r_c = \frac{q^2}{4\pi\epsilon_r\epsilon_0 k_B T} \tag{1.8}$$

where q is the electronic charge, ϵ_r is the dielectric constant of the surrounding material, ϵ_0 is the vacuum permittivity, k_B is the Boltzmann constant and T is temperature. At electron-hole separations greater than r_c, the charges are predicted to fully dissociate to form free charge carriers. The electron and hole are vulnerable to geminate recombination at distances below

r_c, where they are described by Onsager theory to have a probability of their separation *P(E)*, equal to 1-*P(E)* of recombination:

$$P(E) = exp(\frac{-r_c}{a})(1 + \frac{qr_c}{2k_BT}E) \tag{1.9}$$

where E is the electric field strength. In organic materials, r_c and a are usually around 4 nm and 0.5 – 1 nm respectively,[24,45] and thus the importance of the other variable terms in equation 1.9, specifically temperature and the electric field, become clear. Comparisons of experimental and theoretical results in application of this model to investigate probability of charge separation as a function of electric field strength have been carried out on a variety of systems.[46–49] Furthermore, equation 1.8 evidences the influence of the dielectric constant in determining r_c and hence the exponential factor in the probability equation. In organic materials, ϵ_r tends to be significantly smaller than that of inorganic semiconductors, typically below 4 and exceeding 10 in the former and latter respectively, and as high as 11.7 in silicon.[50] Hence the probability of exciton dissociation is greatly diminished in OPVs compared to inorganic materials. As such, design and modelling of OPVs with the aim of maximising ϵ_r has been the focus of some important research.[51–53]

Onsager theory was later expanded to Onsager-Braun theory when Braun revised the model to account for the finite lifetime of CT states.[45] In Onsager theory, an assumption is made that when $a = 0$, recombination occurs irreversibly with 100 % probability. The Braun modification allows for the CT state to have some lifetime, τ, during which several dissociation and recombination attempts may occur, all of which are reversible. The probability of charge separation as a function of electric field strength is then given by:

$$P(E) = k_d(E)\tau(E) \tag{1.10}$$

Where k_d is the rate constant for dissociation and τ the lifetime of the CT state.

Further modifications to Onsager-Braun theory include taking into account that disordered systems may exhibit a distribution of CT state separations, in which case the probability should

be integrated over the range of a values.[41] Other work by Tachiya has developed Onsager-Braun theory to allow consideration of high electron mobility[46] which facilitated the application of the model to charge generation in conjugated polymers.[54]

It is worth noting that organic semiconductors exhibit large contributions from energetic disorder[55] and high reorganisation energies along the charge separation reaction coordinate, which is not explicitly treated in Onsager-Braun theory as it is in Marcus theory. However, there have still been several successful applications of the model to organic photovoltaics, acquiring data that are consistent with experimental results of photocurrent dependence on field strengths, temperature and applied voltage.[41,42,56]

1.3.7 Charge transport and extraction

Once excitons have successfully dissociated into free carriers, they must be extracted at electrodes in order to generate photocurrent. This necessitates the complete transport of charge carriers from the site of their separation to the respective electrodes. In conjugated organic molecules, delocalised π-systems persist across the individual molecular units which facilitates fast intramolecular charge transport. However, intermolecular charge mobility necessitates appropriate delocalisation of MOs towards neighbouring molecules, determined by intermolecular packing within a domain.[57] The charge mobility in organic semiconductors is thus highly sensitive to structural and energetic disorder giving rise to fluctuations in non-covalent intermolecular interactions.[58] Particularly in conjugated polymers, the relative conformations of the polymer backbone establishes the uniformity of the structures across the domain and also determines the ability of electronic wavefunctions to delocalise along the chain.[59] Venkateshvaran et al. showed that even conjugated polymers with relatively low crystallinity exhibit a much lower degree of energetic disorder than more crystalline polymers due to the distribution of the polymer backbone conformation throughout the material.[60] This result demonstrates that it is the uniformity of the molecular conformation distribution that controls the charge mobility in polymer semiconductors, as opposed to the crystallinity of individual molecular units.

In the case of molecular semiconductors comprising donor-acceptor blends, efficient charge

transport is promoted by enhanced crystallinity of materials, favouring large and ordered domains.[61] Conversely, smaller and more thoroughly intermixed domains benefit charge separation rates and quantum yields, simply due to the fact that excitation events have a higher probability of occurring near to an interface with an electron-acceptor.[62] These circumstances establish an important compromise in the consideration of active layer morphology in the optimisation of photovoltaic devices, which is addressed in chapter 3.

1.3.8 Recombination

As outlined in the previous section, excitons formed as a result of the absorption of a photon must separate into free electrons and holes in order to achieve photocurrent generation. Those free charges must also be subsequently collected at electrodes, requiring their transport through the material and their successful completion of the journey from the site of charge separation to the electrode. However, at several stages during this process the electron and hole may recombine, resulting in a relaxation from the excited state back to the ground state, effecting a loss of energy.[63] The fate of the excitation energy is determined by the mechanism by which the recombination occurs.

Radiative and non-radiative recombination processes result in the emission of photons and phonons respectively and have different implications for device optimisation. Radiative recombination is understood to be unavoidable in solar cell devices as an intrinsic property of a photovoltaic material.[64] Conversely, materials and device configurations can be optimised in an attempt to attenuate non-radiative recombination.[65–71] The understanding of non-radiative recombination mechanisms therefore grants opportunity to suppress charge carrier recombination and thereby maximise device efficiencies in photovoltaics.

Geminate recombination (GR) refers to the monomolecular recombination of an electron and hole which originate from one common exciton. When an exciton dissociates and forms a charge transfer state, it must overcome the Coulombic binding energy and separate into free charges within the charge transfer state lifetime, otherwise the “geminate pair” will recombine. GR can occur either radiatively or non-radiatively, typically on the timescale of picoseconds to

tens of nanoseconds, and competes with the crucial charge separation process.[72] Among the key conditions which influence the competition between geminate recombination and charge separation are energetic driving forces[73,74] and material morphology.[75–77]

In the case that electrons and holes successfully avoid GR and achieve charge separation, they are still vulnerable to non-geminate recombination (NGR) if they encounter another charge carrier during their diffusion towards the electrodes. In NGR, an electron and hole originating from distinct excitation events collide somewhere in the material, resulting in relaxation of the relevant excited states to their respective ground states. Once again, the wasted excitation energy may be spent radiatively or non-radiatively. NGR is a bimolecular process, dependent on the populations of both excitons and holes, and hence scales linearly with the product of their densities. This is a far slower process than GR, occurring on the timescale of nanoseconds to milliseconds.

At lower charge carrier densities there is the additional contribution from trap-assisted recombination, the theoretical description of which was devised by Shockley, Read and Hall.[78] Free charge carriers may encounter an energy level that lies within the material band gap, known as a "trap state". If this state is sufficiently deep that the thermal energy cannot surmount the barrier to its release, then the charge will become localised or "trapped". If a free electron encounters a trapped hole, or vice versa, they may annihilate one another, bringing about relaxation to the ground state and loss of excitation energy in the form of non-radiative decay.[79] Trap-assisted recombination is the dominant energy loss mechanism in solar cells in the typical case;[80] therefore, optimisation of materials in order to minimise populations of trapped charges is essential.

Trap states can arise from defects[81] which in some cases are intrinsic to the material. Otherwise, trap states are established as a result of extrinsic defects which may be introduced intentionally via doping or unintentionally by exposure to environmental effects or interfaces with other materials, among many other factors.[82] Hence trap states may also develop over time as a result of degradation of devices, provoking a depletion in optoelectronic performance.[83,84] Materials can thus be engineered in order to suppress their susceptibility to this evolution and therefore

to minimise densities of trap states in an attempt to boost device performance and longevity, which is investigated in detail in chapter 4.

1.4 Types of photovoltaic materials in this thesis

In commercially available photovoltaics composed of crystalline silicon, covalently bound lattices yield rigid structures with large costs of preparation, installation and operation. High processing temperatures are required for doping in order to induce semiconducting properties, which further increases manufacturing properties. These criteria, together with their inferior efficiency compared to fossil fuels, preclude solar power from fully replacing mankind's currently employed sources of electricity.[85]

This thesis explores a variety of photovoltaic systems which strive to surmount these obstacles, associated by their exploitation of "soft" materials. Chapters 3 and 4 address "next-generation" photovoltaic materials comprising organic components, either as the active material or as ligands to nanocrystals. Chapter 5 examines biological systems, which can be regarded as the upper limit of complexity in the realm of organic molecules. Nanocrystals and organic molecules exhibit weaker interactions compared to those in conventional solar cells, in the form of ionic bonds and Van der Waals forces, granting them their soft nature. In synthetically produced photovoltaic materials this enables simple, low-cost processing techniques from solution, while facile chemical structure tuning facilitates the control of optoelectronic properties.[86] Soft materials afford lightweight, flexible and printable films, thereby further reducing the complexity of preparing photovoltaic devices while also granting access to curved structures with greater potential for commercial implementation than rigid lattices.[87]

The studied materials also bear comparable optoelectronic properties. All systems exhibit excitonic character - requiring separation of charges after photon absorption - in contrast to silicon photovoltaics which spontaneously generate free charges on excitation. Furthermore, their large extinction coefficients establish enhanced photon absorption as well as energy transfer, due to efficient absorption by the energy acceptor.[50] However, discussions pertaining to nanocrystal,

organic and biological materials naturally present some distinct traits exhibited by each system. The subsequent sections therefore introduce the individual optoelectronic behaviours of the materials considered in this thesis in greater detail.

1.4.1 Nanocrystals

One major factor requiring optimisation in order to maximise the efficiency of photovoltaic devices is the absorption spectrum of the active material. Ideally materials will harness as many photons as possible but are restricted by their band gap, E_g. Photons of energies $E_{h\nu} < E_g$ are not absorbed, while the excess energy associated with photons $E_{h\nu} > E_g$ is wasted as heat. Therefore, materials for which the band gap can be tuned are amongst the most promising for the future of photovoltaic devices.

Arguably the best examples of this class of material are quantum dots: colloidal semiconductor nanocrystals (NCs) usually 1 – 10 nm in diameter. Here the NC radius is exceeded by the exciton Bohr radius resulting in "quantum confinement". If this condition is met, the band gap of the material is not only determined by the exciton binding energy E_B - as is the case in bulk materials - but is also influenced by the radius of the NC, R_{NC}, as dictated by the confinement energy term (E_C) in the equation:[88]

$$E_g = E_{bulk} + E_C + E_B = E_{bulk} + \frac{h^2}{8\mu_{eh}R_{NC}^2} - \frac{1.8q^2}{4\pi\epsilon_0\epsilon_r R_{NC}} \tag{1.11}$$

where E_{bulk} is the binding energy in the bulk material and μ_{eh} is the reduced mass of the electron and hole. The quadratic dependency of the denominator on the positive E_C term in conjunction with the linear tendency of the denominator on the negative E_C term together determine that for any given material (i.e. where E_{bulk} is constant), an increasing R_{NC} corresponds to a decreasing E_g. Hence the band gap can be modified according to the size of the quantum dot in question, in some materials permitting up to a 1 eV tuning range.

As the exciton is also confined in all three dimensions in space, the continuum of energy levels exhibited by a bulk inorganic semiconductor is lost and energy becomes quantised into discrete

levels. The spacing of these levels is dependent on R_{NC} and hence the electronic properties of the material can also be tuned, as established by the size of the nanocrystal. Together the power to determine these two characteristics affords great control over the optoelectronic properties - and thus the photovoltaic performance - of active materials when NCs are employed.

The quantum confinement effect was first suggested in 1982 by the Efros brothers and in 1988 the nomenclature "quantum dot" was coined.[89] By the turn of the century, commercial production of colloidal NCs was accessible. The last decade has seen easy fabrication of NC films such that solid-state NC solar cells have emerged and are now at the forefront of photovoltaic research. Of these, the most thoroughly studied are quantum dot metal halide perovskite solar cells which recently exhibited a PCE above 16 % placing them in the league of front-runners in the hunt for novel photovoltaic materials.[90]

1.4.2 Organic semiconductors

Organic semiconductors are composed of π-conjugated carbon-based molecules, for which photoconductivity was first demonstrated in 1906.[91] Half a century later saw the first demonstration of photoconductivity in polymers, which are often incorporated into organic photovoltaic (OPV) materials as the electron donating, or "donor", component due to their electronic properties.[92]

In organic molecules, the flexible nature of the molecular structures causes a reduced degree of crystallinity compared to inorganic semiconductors, such that the orbitals cannot delocalise infinitely. Instead, molecular orbitals are formed from the sharing of electron density between p- and d-atomic orbitals across the molecule itself. This provides molecular delocalisation in the form of conjugated π-systems across the molecule, in which the lowest energy electronic transition is excitation of an electron from the HOMO to the LUMO.

As electrons and holes in organic semiconductors are tightly bound by the exciton binding energy, they cannot be separated unless exposed to an energetic offset which facilitates overcoming the Coulombic attraction between them. To this end, OPV devices typically comprise a blend of an electron-rich donor (D) component with a comparatively electron-deficient acceptor (A)

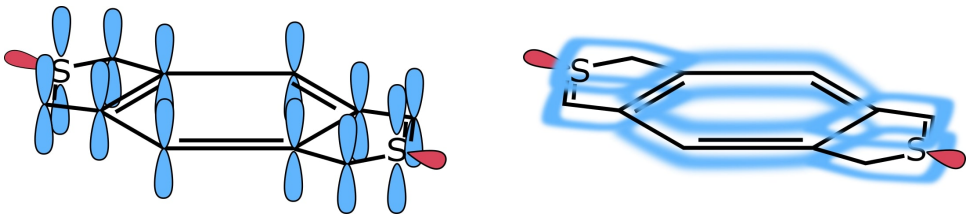


Figure 1.6: Delocalised π-electron cloud (right) above and below molecular plane of electron-rich benzodithiophene due to conjugation of p-orbitals (left). Lone pair orbitals on S are not involved in conjugation.

component. In the typical case, the D and A components are selected to have LUMO-offsets sufficient to overcome the exciton binding energy, by design. Hence the interface between D and A domains provides an energetic driving force for the separation of the electron and hole. The donor and acceptor are blended in a thoroughly intermixed morphology denoted a bulk heterojunction (BHJ), in order to provide sufficient surface area between donor and acceptor and therefore overcome the large exciton binding energies inherent to most organic materials (e.g. 0.7 eV in P3HT compared to 15 meV for silicon) and thus allow charge separation.[93] The BHJ was a major breakthrough in OPV performance, first suggested in 1986 by Tang et al., and since has been widely accepted as the most efficient method by which to efficiently generate photocurrent in organic semiconductors.[94,95]

The exciton must first diffuse to the interface by random hopping through the domain. During this process, the exciton may also recombine to restore the ground state and therefore the rate of diffusion must outcompete that of recombination. The diffusion length is normally on the order of 10 nm in organic materials,[24] therefore the blend morphology must be carefully optimised to ensure that a sufficient population of excitons reach an interface to afford substantial device efficiency. It follows that charge separation is most efficient in thoroughly mixed D:A blends with small domains and a large surface area of interface. Hence there is a fine balance of D:A blend morphology to be achieved in order to maximise the device performance.

The mechanism of photovoltaic charge generation in a representative case is shown in figure 1.7. Within the donor material, an incident photon causes excitation of an electron from the HOMO to the LUMO, affording an exciton. The exciton remains bound as it travels through the donor domain until it meets an interface with the acceptor material, which introduces the

exciton to the molecular orbitals on the acceptor. Electron transfer to the lower energy acceptor LUMO provides the energetic offset to separate the exciton and to form a CT state. Here the two charge carriers are less tightly bound relative to the exciton and thus can dissociate into free charges to form a charge separated state where the carriers can travel through the material independently and give rise to photocurrent. Due to strong coupling between electrons and phonons in organic molecules, the newly generated free charges also distort the surrounding lattice to afford polarons.

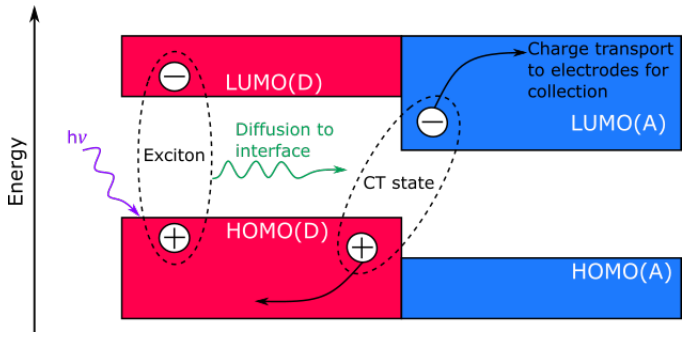


Figure 1.7: Schematic of exciton generation, diffusion to the donor:acceptor interface, charge transfer state formation and charge separation in a typical organic donor:acceptor blend after excitation by a photon.

Historically, polymers have been widely employed as the donor component although small molecule donors are recently gaining traction in the field. The polymer that has dominated the field over several decades is P3HT, first synthesised in 1993 and now the focus of over a thousand publications focusing on the properties arising when it is blended with a fullerene acceptor.[96] Other prominent polymers which have gained notable attention are PffBT4T-2OD[97] and PBDB-T, with the latter affording impressive PCEs in a number of OPV devices, in some cases as high as 17 %.[98]

The ultimate electron accepting material was long considered to be a derivative of a fullerene molecule C_{60}, first demonstrated to act as electron acceptors due to photoinduced charge transfer from a polymer in 1992.[99] The C_{60} and C_{70} derivatives phenyl-C_x-butyric acid methyl ester ($PC_{61}BM$ and $PC_{71}BM$) received the vast majority of attention in the discussion of acceptors. They are strongly electron-accepting and promote high electron mobility, owing to the molecular orbital structure in which the LUMO is delocalised over the whole molecule.[93] They also

allow isotropic charge transport and reversible electrochemical reduction as well as yielding favourable morphologies in blends with polymer donors.[100]

Employing fullerene-based acceptors, however, grants very little freedom in chemical structural manipulation and thus restricts the tuneability of frontier orbitals and band gaps.[101] This limits the possibility to improve their poor absorption of visible and near-infrared light while photooxidation processes and photoinduced aggregation afford an inherent lack of operational stability.[102] Attempts have been made to tune the properties of donors in blends with fullerene-based acceptors in order to combat these barriers to progress. However, the requirements of fullerenes give such a restricted specification that transitioning to small organic molecules as electron-accepting components in D:A blends has been the focus of recent work.[103–105]

Non-fullerene acceptors (NFAs) typically comprise a planar, conjugated and electron-rich core flanked by electron-withdrawing side chains to afford an A-D-A motif for promotion of charge transport within the material. This "push-pull" effect also induces a spectral shift due to absorption of light at longer wavelengths, owing to intramolecular charge transfer between the electron-donating and electron-accepting parts of the molecule.[106] NFAs may also exhibit a lower band gap than that of the donor component in an OPV blend, enabling absorption of light into the near IR region.[107] Moreover, the opportunity to manipulate the chemical structure of a small molecule acceptor allows control of the electronic properties of the molecule and thus grants tuneability of its absorption spectrum.[108] The first NFA OPV device to surpass the performance of fullerene-based blends comprised a blend of the small molecule acceptor IT-4F with the commonly employed polymer donor, PBDB-T, in 2017.[109] More recently, the blend of a D-A copolymer D18 with the NFA Y6 yielded a noteworthy result by advancing the highest recorded efficiency in an OPV system to 18 %, demarcating an exciting turning point in the field.[110]

1.4.3 Light-harvesting in cyanobacteria

In reality, it is inaccurate to credit the first demonstration of photovoltaic technology to inorganic materials in 1839 when the advent of harnessing photons to yield free charge carriers

dates back 3.4 billion years.[111] Photosynthetic bacteria were the first innovators to optimise the capture of solar energy, followed by cyanobacteria 2.3 – 2.7 billion years ago with the introduction of photon capture in conjunction with synergistic oxygen production.[112,113] The diverse array of pigments found in cyanobacteria grants them the capacity to absorb photons spanning 400–700 nm.[114] This, in conjunction with large pigment densities and a highly efficient charge separation pathway, grants cyanobacteria their light-harvesting quantum efficiencies of 95 % or more.[115]

The pigments and the reaction centre (RC) are organised into large pigment-protein complexes called photosystem I (PSI) and photosystem II (PSII) in oxygenic photosynthetic cyanobacteria. These complexes are transmembrane proteins embedded in the membranes of particular organelles designated to carry out the photosynthetic process, called thylakoids.[116] PSII carries out the oxidation of water and simultaneous production of molecular oxygen.[117] This cell structure and the processes triggered by photon absorption are shown in figure 1.8.

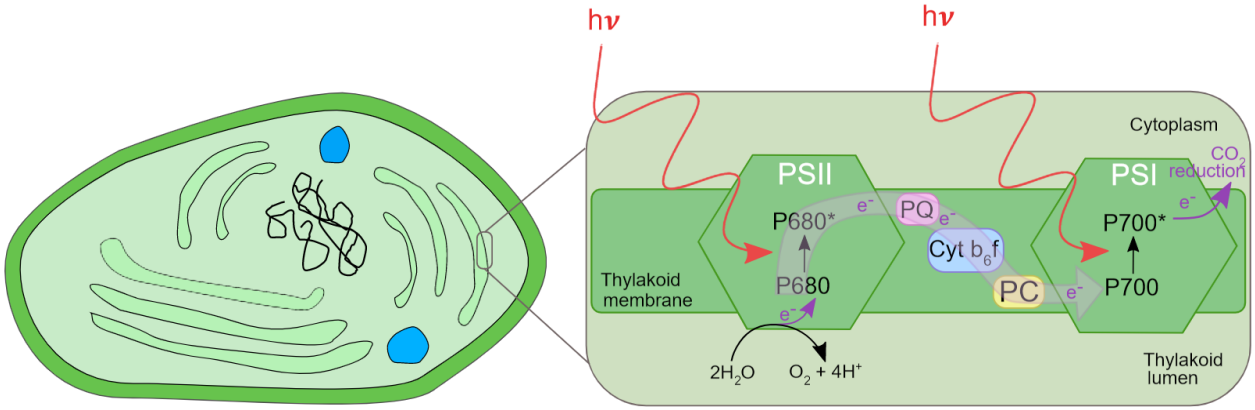


Figure 1.8: Cyanobacteria, PSI and PSII embedded in a thylakoid membrane, with the photosynthetic mechanism illustrated.

PSII comprises the RC, for which the primary function is charge separation - named P680 owing to its absorption maximum at 680 nm. A range of antenna pigments also reside in PSII, which absorb specific wavelengths of light and shuttle the excitation energy into the RC. The pigments on the 700 kDa complex include chlorophyll-*a*, carotenoids and phycobilisomes, together accomplishing an absorption spectrum that spans from blue to red.[118] The dominant PSII absorptions are exhibited by chlorophylls at 675 nm and 420–440 nm while PSI primarily contains P700, with an absorption maximum at 700 nm.[119]

The photosynthetic process begins on formation of an excited state on P680, denoted P680*. This can occur either by absorption of a photon by P680 itself, or absorption within an antenna pigment followed by energy transfer to P680. Subsequent charge separation generates a pair of charge carriers - a hole and an electron. The hole is filled by extraction of an electron during water splitting by the water oxidation complex (WOC), simultaneously producing O_2. The WOC cycle generates four electrons and four holes to afford one molecule of diatomic oxygen, by splitting two water molecules.[117] This process occurs at a turnover frequency of 1000 s^{-1} *in vivo*.[120] Meanwhile, the free electron navigates through a cascade of redox processes optimised to mediate the transfer of the electron from PSII to PSI, known as the electron transport chain. The electron is first accepted by plastoquinone (PQ), then passed to enzyme cytochrome b_6f (Cyt b_6f) before being accepted by plastocyanin (PC) and finally reduced PC passes the electron to P700 in PSI. Further absorption of a red photon by PSI excites the electron to a higher electronic energy level, constituting PSI*. The excited PSI is then able to donate the electron to nicotinamide adenine dinucleotide phosphate ($NADP^+$) to generate NADPH, which is the reducing agent consumed in the process of fixing CO_2 to form glucose. This mechanism thereby stores solar energy as chemical energy in carbohydrate bonds, providing energy for the cyanobacteria's cellular processes.[121]

Biophotovoltaic devices

Due to the energy crisis and the infinite supply of solar energy relative to the timeframes of human consumption, there is enormous motivation to mimic the biological mechanisms of harnessing photons for the generation electrical energy.[122] As described above, electrons extracted from water splitting in natural photosynthesis are used to reduce carbon in CO_2 and store energy in chemical bonds in biomass. Although the quantum efficiency of light-harvesting nears unity, the efficiency of biomass production is under 1 % and has a theoretical maximum efficiency of only 4.5 %.[123] However, the efficiency of the preceding water splitting step has a theoretical maximum efficiency of 70 %.[124] The most promising route for mimicking the photosynthetic apparatus for solar energy harvesting - in terms of absolute efficiency - therefore lies in the direct coupling of photosynthetic water splitting to electrical energy production, as

opposed to the storage of energy in biomass. To this end, oxygenic photosynthetic microorganisms have sparked interest in the field of renewable energy generation due to their ability to transfer electrons extracted by water splitting into external materials, in a phenomenon termed exoelectrogenesis.[125–127]

Biophotovoltaic devices (BPVs) take advantage of exoelectrogenesis and can be considered to be "living solar cells".[128] BPVs, of which the first was described over forty years ago,[129] specifically use only water and light to generate electrical current, in contrast to microbial fuel cells which are powered by an organic fuel.[130] Such devices employ the natural photosynthetic machinery to induce water splitting, extracting electrons that are subsequently transferred to an anode via direct and/or mediated indirect electron transfer. By connection of the anode to an external circuit, the electrons are passed to the cathode. Meanwhile, the oxygen that is oxidised at the anode diffuses across to the cathode where it is reduced in the counter reaction to form water, which in turn diffuses to the anode. The potential difference across the electrodes gives rise to electrical current.[131]

Historically, BPVs comprised a dual-chamber system where the electrochemical cell was divided by a partially permeable membrane. This ensured the separation of the components within the electrolyte to ensure their activity at the correct electrodes.[132,133] However, degradation and clogging of the membrane over long operation periods, as well as an increased device resistance, caused suboptimal device performances.[134] It has recently been argued that cells are sufficiently strongly immobilised onto the anode that they will not come into contact with the cathode, negating the need for two separate chambers.[135] Hence, in recent years, single chamber systems are the most popular configuration for electrochemical implementation of BPVs.

Either a two- or three-electrode system may be employed. In a two-electrode system, a potentiostat connected across the electrodes applies a bias potential and simultaneously detects current across the circuit. The measured power output is a commonly reported metric by which BPV performances are compared.[136] The two-electrode system has been successful in many electrochemical experiments with diverse biological applications, from BPVs employing the green algae *Chlorella* to investigating the role of photosystems in power output.[137–139] In a

three-electrode system, the addition of a reference electrode (typically composed of Ag/AgCl) facilitates precise control of the potential at the anode.[140] Therefore, the three-electrode system is the most prominent approach for probing the redox processes at the electrodes with precise quantitative measures.[141] Regardless, in the case of either a two- or three-electrode system, platinum is most frequently used as the counter electrode to promote the cathodic reduction of oxygen.[142–144]

The anode material has seen enormous development for the optimisation of BPV performance over the last four decades. The key design principles require the anode to exhibit strong electrical conductivity, electrochemical stability, optical transparency and biocompatibility, as well as being a suitable material for the adsorption of microorganisms.[130] First generation electrodes composed of platinum and tin oxide originated in 1979 which possessed most of the necessary properties. Nonetheless, their flat surface topologies gave rise to poor and inconsistent cell loading, which in turn led to unimpressive photocurrent densities.

Second generation electrodes were established in order to introduce surface roughness for enhanced cell immobilisation yields. They were composed of nano- and micro-structured carbon fibre with impressive surface areas which also offered the benefits of conductivity, robustness and low cost.[142] However, their opaqueness meant that microorganisms embedded within the microstructure were poorly illuminated due to the lack of light penetration through the anode material. Moreover, chemical tuning of the surface was required in order to combat its hydrophobicity such that they could be biocompatible.[130]

Lessons from the preceding generations of anode materials led to the design of state-of-the-art third generation electrodes, exhibiting porous 3D structures composed of inverse opal-indium tin oxide (IO-ITO) which outperformed carbon-based electrodes.[137] They offered improved electrical conductivity and transparency, while the high cell loading afforded by large surface areas in second generation materials was preserved due to the 3D microstructure.[145] Adhesion of cells was enhanced both by their nanoscale roughness and also by employing a more suitable hydrophilic material in order to counter the intrinsic lack of biocompatibility of carbon electrodes. Furthermore, IO-ITO anodes present the possibility for adaptation of the structure

for different applications.[146] Pore dimensions could be tuned according to microorganism sizes and also to promote light transmission. In the last decade, ITO and fluorine-doped tin oxide (FTO) have become the benchmark anode material.[129,137,147,148]

The last twenty years have seen emerging interest in employing whole living microorganisms as the active photosynthetic material in BPVs.[149–151] Among these, cyanobacteria are the most commonly employed, either as pure cultures[152] or as environmental samples.[153,154] They are readily available, have well understood spectroscopic characteristics[155] and are considered to be the "future workhorses in photobiotechnology".[122] To prepare a BPV device, cyanobacteria cells are immobilised onto an electrically conductive anode by direct dropcasting and are subsequently allowed to dry in order to mature into a biofilm before electrochemical use.[156]

The highest-performing cyanobacteria BPV was reported by Kaushik et al. in 2017 to have a power density of 610 mW m^{-2} using the *Synechococcus* cyanobacteria strain in a three-electrode system.[157] In the same year a similar result of 600 mW m^{-2} was obtained for the green algal species *Chlamydomonas* by Longatte et al. in a three-electrode system.[158] The record photocurrent density for a two-electrode system was reported to be 538 mW m^{-2} by Saar et al. in 2018 by employing genetically modified *Synechocystis* cyanobacteria.[134] However, it has been calculated by McCormick et al. that power densities up to 7.7 W m^{-2} could be achieved if these devices are further optimised and therefore the enhancement of BPVs poses a worthy focus of investigation.[159]

While a variety of different cyanobacteria species have been applied, the most prominent is *Synechocystis* sp. PCC6803 (hereafter referred to as Synechocystis).[144,155,160,161] This cyanobacterium is a single-celled microorganism of 1.6 μm diameter which has repeatedly been a model organism in the research of photosynthesis.[130] Although its power densities are currently surpassed by analogous systems employing other strains, its well-understood energetics and its availability for facile genetic manipulation grant Synechocystis its position as favourite in the field.[162]

As well as sessile microorganisms, several studies have employed representative systems for BPVs. Thylakoid membranes,[137,163] chloroplasts[164] and photosystems[144] can be isolated and

immobilised onto anodes for generation of electrical current.[165,166] Mesoporous IO-ITO architectures were especially designed with correct roughness for isolated photosystems, which afforded a 1600-fold improvement in biocatalyst loading and a consequent thousand-fold enhancement of power density compared to flat electrodes.[167] However, isolated complexes are markedly less stable than complete cells due to their lack of exposure to their native environment. Unlike *in vivo* cells, they cannot self-repair and therefore exhibit device lifetimes of minutes to hours,[117] while BPVs implementing whole microorganisms survive for several days.[138] Aside from isolated photosystems, a number of artificial derivatives inspired by the photosynthetic water oxidation catalyst have been investigated as photocatalysts for water splitting including those based on ruthenium,[168,169] iridium,[117] manganese,[170] cobalt[171,172] and nickel.[173] However, the remarkably lower cost of employing natural microorganisms, as well as their ability to self-repair, maintains the ever-growing interest in the application of complete-cell microorganisms for BPVs.

The field of BPVs stands at an exciting time with perpetual advances in their performance. However, their study very much remains in its preliminary stages and lacks crucial areas of fundamental understanding which present integral challenges. Importantly, the transfer of electrons between the photosystems and the electrode is poorly understood and the discussion around disentangling this complex process is ambiguous.[122] The field itself and the nature of reporting results lacks standardisation, obscuring the monitoring and continuation of progress. Studies report varying units of current output and power density. Some neglect the essential considerations of illumination intensity and wavelength, BPV surface area, cell culture and loading conditions as well as experimental conditions such as temperature, pH and buffer conditions of the electrolyte.[130] The application of a two-electrode system means that the potential at the anode cannot be precisely controlled, giving rise to doubt pertaining to the electrochemical parameters. Strong cell-electrode interactions are also crucial, which require meticulously controlled environmental conditions for culture growth and sample preparation, which are likely to vary from lab to lab. Altogether, the comparison between different architectures, experimental and preparation conditions is not always straight forward.

Normalisation of cell loading and activity is a further factor that varies across the field. In

cyanobacteria studies, BPV efficiency is typically normalised according to total content of chlorophyll-*a* pigments, which carry out the majority of light absorption.[137,174] However, chlorophyll content is known to vary dramatically with the microorganism's environment and hence this metric does not necessarily quantify the active pigment content during operation with any accuracy.[130] Some studies normalise power outputs according to cell loading biomass which introduces further uncertainties in the comparison of efficiencies. Other abiotic factors may also respond to the environment during experiment, such as sample heating or decomposition as a consequence of light irradiation.[122] Overall, these elements give rise to results which are not only difficult to compare from study to study, but also difficult to accurately report for a single experiment. The field of BPVs thus requires extensive optimisation, standardisation and development in order to gain clarity on factors that influence device efficiencies, in order to enhance performance such that these exciting devices could be considered industrially applicable. In chapter 5, spectroscopic and spectroelectrochemical characterisation techniques are employed in order to explore the behaviours of cyanobacteria cells incorporated into BPVs.

Ultrafast processes in photosynthesis

As mentioned in the previous section, the absorption of light in cyanobacteria is carried out either in the RC or in pigments which shuttle the excitation energy into the RC for the subsequent charge separation (CS) step. The light absorption takes place on the femtosecond timescale, but the excitons have lifetimes of only a few nanoseconds. Energy transfer towards the RC must therefore be both ultrafast and irreversible. Typically, the conversion of solar energy into electrochemical energy occurs within a few tens of picoseconds with efficiency nearing unity.[175] There therefore exist compelling resolutions to the energy crisis concealed within the photosynthetic machinery, which could grant mankind a pathway to efficient and abundant renewable sources.

Several studies have revealed that the RC structure is crucial to the efficiency of photosynthesis, by means of enhancing the yield of photon absorption, the rate of energy transfer and the efficiency of CS.[176–178] Emerson and Arnold first proposed the concept of a photosynthetic RC

in 1932.[179] Later Duysens demonstrated experimentally that most chlorophyll molecules in the PSII structure act as pigments to absorb solar photons and then transfer energy to a "special pair" of chlorophylls.[180] The PSII RC structure, shown in figure 1.9, has been confirmed by x-ray crystallographic studies with atomic resolution.[181,182] Chlorophyll pigments are arranged amongst two branches, denoted D_1 and D_2, which are linked at the two central special pair chlorophylls. The special pair chlorophylls leading to the D_1 and D_2 branches are labelled P_{D1} and P_{D2} respectively. They are each connected to another chlorophyll molecule denoted Chl_{Dn}, which binds a pheophytin molecule Phe_{Dn} (where n=1,2 depending on the branch).[175] The RC can absorb light directly or receive it via energy transfer from the antenna pigments.[183]

Due to the close-packed nature of the chromophores, absorption of photons results in the formation of Frenkel excitons which can be delocalised over multiple pigments.[184,185] Excitons on the RC have been shown to relax to the lowest-lying excited state in a few hundred femtoseconds, from which a CT state is formed by the localisation of an electron and hole on separate pigment molecules.[186] The final fully separated state, $P_{D1}{}^{+}Phe_{D1}{}^{-}$, forms within a few tens of picoseconds hence kinetically outcompeting back-transfer from the CT state. The precise mechanism by which this CS occurs has been investigated extensively where the removal,[187] replacement[188] or mutation[189] of pigments and nearby protein complexes allows targeted assignment of spectral signatures. Experimental results measured by Romero et al. in 2010 indicated the activity of two distinct charge transfer pathways in a finding that was corroborated by theoretical studies, which are also illustrated in figure 1.9.[190,191]

The CT and CS pathways were historically assumed to occur by random incoherent hopping from site to site, as is exhibited in organic semiconductors.[115] However, recent development of two-dimensional electronic spectroscopy[192] has facilitated the direct interrogation of the dynamic electronic structure of photosynthetic complexes.[193–195] Application of this technique unveils coherent effects, where direct coupling of states that are delocalised over multiple pigments allows the electronic excitation to sample multiple states simultaneously.[196] A considerable number of studies have suggested that electronic and vibronic (electronic-vibrational) coherences contribute to CS in a vast array of biological light-harvesting complexes.[197–202] In 2007 Engel et al. first found evidence of coherent effects in the Fenna-Matthews-Olson complex

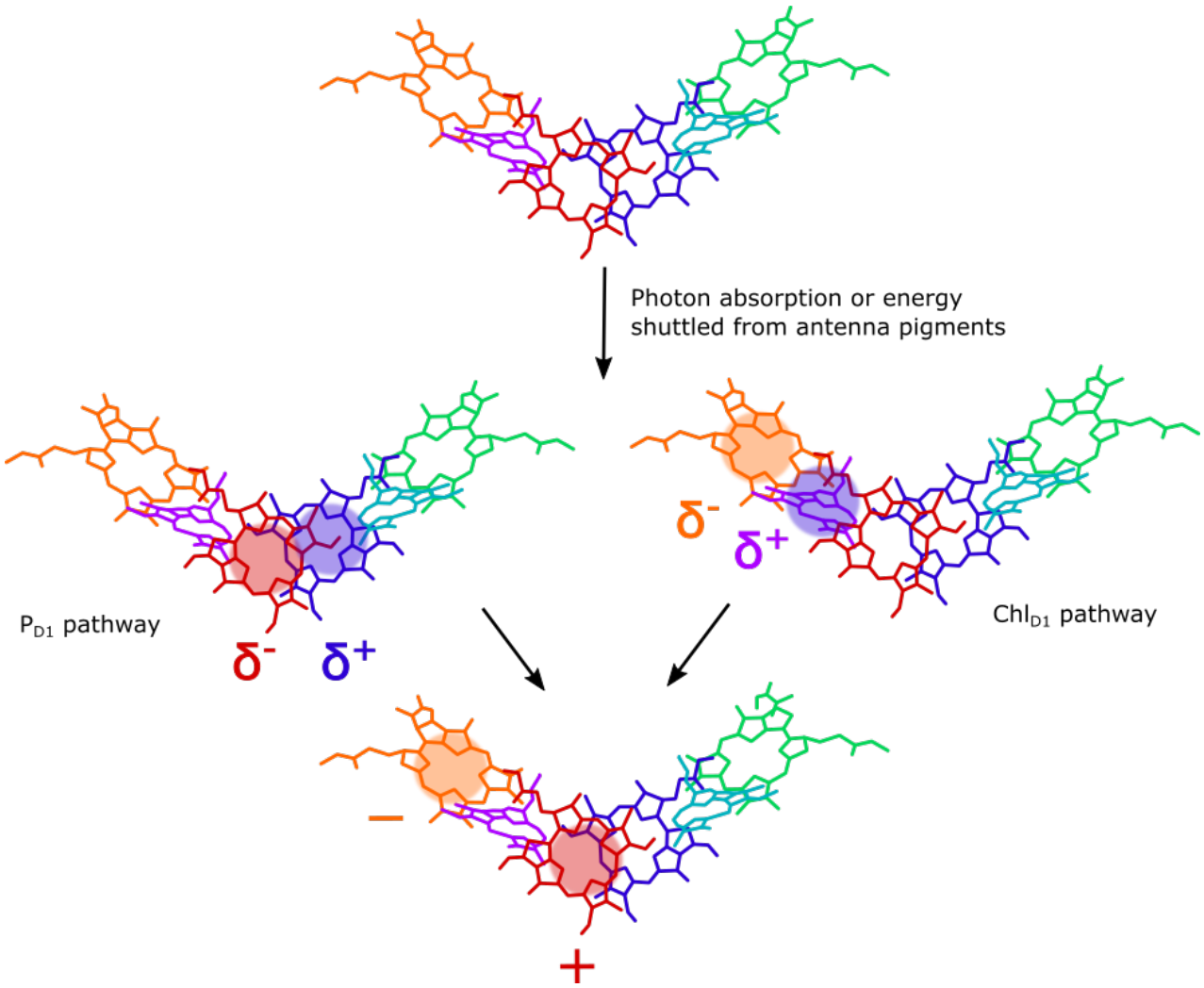


Figure 1.9: The structure of the PSII reaction centre annotated with the two charge separation pathways. Red, purple and orange (blue, teal and green) pigments represent the special pair chlorophyll, branched chlorophyll and pheophytin molecules respectively on branch D_1 (D_2).

(that shuttles energy from pigments to the RC in bacteria) at cryogenic temperature.[203] Later in 2010 Panitchayangkoon et al. detected the same coherences at room temperature.[204] Similar works have established evidence of coherences in other photosynthetic systems,[183] polymers[205] and J-aggregates.[206] Electronic[207] and vibronic[208–210] coherences have also been discovered within the bacterial RC and more recently within the PSII RC.[211] These have been demonstrated to persist for at least a picosecond at physiological as well as cryogenic temperatures.[212] In the PSII RC, the dominant vibronic coherence on the first excited state has been suggested to promote energy and electron transfer between states involved in CS and thus enable ultrafast and efficient separation.[175]

Spectroscopic data may contain evidence of coherent effects in the form of periodic modulations of the signal, which should exhibit frequencies resonant with the difference frequency between relevant delocalised excited states.[203] Most materials typically exhibit coherent effects to some extent but the complexity of biological systems demands the application of coherent spectroscopy in order to extract information about excited state populations. Ultrafast photophysical processes and state delocalisation establish intricate relationships between the densely-packed pigments. It is thus necessary to generate defined phase relations between the excited state wavefunctions in order to probe their dynamic behaviours, by employing coherent spectroscopic techniques.[213] Chapter 5 demonstrates the application of coherent excitation of cyanobacteria *in vivo* for the elucidation of sub-picosecond dynamics within the PSII RC and also for the exploration of the vibrational manifold on the excited state.

1.5 Outline of this thesis

This thesis examines the photophysical behaviours exhibited by various types of photovoltaic materials in an effort to understand and enhance the optoelectronic performance and operational stability of next-generation devices. While the investigated systems span from organic to inorganic semiconductors and even to *in vivo* photosynthetic microorganisms, the common theme is that time-resolved spectroscopic techniques are implemented in order to interrogate the relevant photoinduced processes. These techniques allow the direct photoexcitation of the studied material to an excited state of interest and the subsequent characterisation of the excited state as it evolves over time. In doing so, time-resolved spectroscopy facilitates the observation of the fate of excitation energy and hence provides fundamental understanding of the nature and mechanisms of the photovoltaic process within the material.

The chapters can be summarised according to the following breakdown:

Chapter 2 addresses the experimental details of the spectroscopic techniques that have been developed and employed for the work presented in this thesis. This section describes sample preparation, steady-state absorption and photoluminescence spectroscopy, incident photon-to-

electron conversion efficiency (IPCE), time-correlated single photon counting (TCSPC) and transient absorption spectroscopy setups with both ∼100 fs pump pulses and sub-10 fs pump pulses.

Chapter 3 investigates the effects of structural tuning on small organic molecules for OPV applications. Two chemical modifications are studied. The first study explores the effects of a 1-carbon displacement of an alkyl chain substituent, which manifests a stark contrast in π-stacking and thus blend morphology, manifesting considerable consequences on OPV device performance. The second study investigates the outcome of altering the molecular position of a selenium substitution on a commonly employed NFA. In both cases, transient absorption spectroscopy is implemented to investigate the charge separation and transport dynamics within the OPV material.

Chapter 4 considers the intrinsic stability of photovoltaic devices under operational conditions. In the first study, a small molecule donor DRCN5T is blended with a fullerene acceptor to afford a device that has been reported to exhibit impressive stability, uncharacteristic of fullerene-containing OPVs. Transient absorption spectroscopy is applied to interrogate the photoinduced mechanisms that grant this blend its longevity, revealing that this unique system has access to unprecedented photoprotective mechanisms. The second study examines a set of lead-free NC solar cells with different hole- and electron-transporting layers, which have been reported to exhibit dramatically different operational stabilities. Transient absorption spectroscopy is used to quantify charge trapping lifetimes in order to rationalise these device performance trends.

Chapter 5 explores photosynthetic systems, namely isolated PSII and cyanobacterial microorganisms *in vivo*. IPCE and TCSPC measurements are employed to characterise the behaviours of the systems in BPVs. Transient absorption spectroscopy is implemented to investigate the ultrafast photophysical mechanisms of cyanobacteria *in vivo*, both on the picosecond to nanosecond timescale and also on the sub-picosecond timescale.

Chapter 6 presents the key conclusions of this work and suggestions for the future outlook of the field of next-generation photovoltaic materials.

Chapter 2

Experimental Details

2.1 Sample fabrication

2.1.1 Film fabrication

The films studied in chapter 3.3.1 were prepared by Dr Deping Qian (Imperial College London). $PC_{71}BM$ blend films were prepared from solutions of 10 mg mL^{-1} concentration in chloroform. PBDB-T blend films were prepared from solutions of 10 mg mL^{-1} concentration in a mixed solvent (dichlorobenzene:chlorobenzene=1:1, v/v). Films of neat materials were prepared from solutions of 10 mg mL^{-1} concentration in cholorobenzene or chloroform. Solutions were spin-coated onto clean glass substrates at 2000 rpm for 30 s to achieve a film thickness of approximately 100 nm.[214]

The films studied in chapter 3.3.2 were prepared by Chiara Labanti (Imperial College London). 3,9-bis(2-methylene-(3-(1,1-dicyanomethylene)indanone))- 4,4,9,9-tetrakis(3-((2-ethylhexyl)oxy)-phenyl)-diseleno[2,3-d:2,3-d]-s-indaceno[1,2-b:5,6-b]dithiophene (SeIn) and 3,9-bis(2-methylene-(3-(1,1- dicyanomethylene)indanone))-4,4,9,9-tetrakis(3-((2-ethylhexyl)-oxy)phenyl)dithieno[2,3-d:2,3-d]-s-indaceno[1,2-b:5,6-b]-diselenophene (SeOut) molecules were synthesised by the group of Prof. Yun-Hi Kim (Gyeongsang National University). PBDB-T was used as received commercially from Sigma-Aldrich. Neat films and blend films (donor:acceptor=1:1, w/w) were

prepared from 20 mg mL^{-1} solutions in chlorobenzene and 0.5 % 1,8-diiodooctane additive. The solutions were stirred at 60 °C overnight and filtered through 0.45 μm polytetrafluoroethylene filters. Neat solutions and blends were spin-coated onto clean glass substrates to achieve film thicknesses of 40-80 nm.[62]

The films studied in chapter 4.3.1 were prepared by Dr Andreas Weu (Heidelberg University). DRCN5T and $PC_{70}BM$ were used as received commercially from Ossila and Solenne. Thin films of blends were prepared from solutions in chloroform (donor:acceptor=15:12.5 mg mL^{-1}). Solutions were spin-coated onto clean glass substrates and annealed for 30 min at 200 °C to obtain a film thickness of approximately 100 nm.[215]

The $AgBiS_2$ films studied in chapter 4.3.2 were prepared by Dr David Becker-Koch (University of Dresden).[216]

2.1.2 Optoelectronic device fabrication

The devices studied in chapter 4.3.2 were prepared by Dr David Becker-Koch (University of Dresden). ITO-coated glass was sonicated in isopropanol and acetone and treated with oxygen plasma (100 W, 0.4 mbar, 10 min). ZnO sol-gel was prepared in air by dissolving 0.46 mol L^{-1} zinc acetate and 0.46 mol L^{-1} ethanolamine in 2-methoxyethanol and the solution was stirred at 70 °C for 2 h. ZnO sol-gel was spin-coated in air at 2000 rpm for 60 s and annealed at 300 °C for 30 min. Nanoparticle ZnO was spin-coated in air from 60 mg mL^{-1} solution at 3000 rpm for 30 s and annealed at 200 °C for 10 min. $AgBiS_2$-TMAI nanocrystals were fabricated as described by Bernechea et al. to afford 30-35 nm films on top of electron transport layers.[217] Organic hole transport layers were fabricated in an inert nitrogen environment. PTB7 films were spin-coated on top of nanocrystal layers from 5 mg mL^{-1} solution in anhydrous dichlorobenzene at 2000 rpm for 60 s. Doped PTAA was fabricated by mixing 6 mg mL^{-1} PTAA in anhydrous chlorobenzene with 3 mg mL^{-1} $C_{60}F_{48}$ in anhydrous chlorobenzene. Doped PTAA films were spin-coated onto nanocrystal layers at 6000 rpm for 30 s and annealed at 100 °C for 10 min. A 3 nm MoO_3 layer was deposited by thermal evaporation in the case of PTB7 devices, and the silver electrode was evaporated for all devices.[216]

2.1.3 Cyanobacteria suspension sample preparation

Wild type *Synechocystis* sp. PCC6803 cultures were prepared by Dr Laura Wey (University of Cambridge) and dispersed in solution buffered at pH 6.5. MES buffer was prepared by dissolution of KCl (50 mM, Sigma-Aldrich), $CaCl_2$ (15 mM, Sigma-Aldrich), $MgCl_2$ (15 mM, Sigma-Aldrich) and 2-ethanesulfonic acid (MES, 40 mM, Sigma-Aldrich) in distilled water.

2.1.4 Biophotovoltaic devices

Planktonic cells of *Synechocystis* sp. PCC. 6803 (Synechocystis, 2 μm diameter) were used as provided by Dr Jenny Zhang (University of Cambridge). ITO-coated glass substrates were cleaned in an ultrasonic bath in a sequence of water, acetone and isopropanol and then air-dried. For *in vivo* cyanobacteria devices, a 4 μL suspension of Synechocystis was dropcast onto the clean substrates. For PSII devices, 2 μL of isolated PSII pigment-protein complexes (provided by Dr Jenny Zhang) were dropcast onto mesoporous IO-ITO electrodes. The droplets were covered for protection against fibres and airborne particles and allowed to mature into a film in the dark at room temperature for approximately 30 mins. For device measurements, electronic connections were made with adherence of conductive Ag tape to the ITO layer.

2.2 Steady-state measurements

2.2.1 Ultraviolet-visible absorption spectroscopy

The illumination of a material results in the incident light being absorbed, reflected or transmitted. In the steady state, light may only be absorbed by the material if it is resonant with an allowed electronic transition from the ground state (GS) to a higher-lying excited state (ES). Therefore, the particular wavelengths of ultraviolet (UV) and visible light that are absorbed by a material provide a fingerprint of the electronic transitions accessible to the GS. In the photovoltaic materials discussed in this thesis, the prominent transition from the GS to the

lowest-lying ES lies in the UV-visible range. The spectrum of absorption amplitude as a function of wavelength in the UV-visible (UV-vis) range is therefore valuable in characterising the electronic structure of the material.

The absorption amplitude at a given wavelength, $A(\lambda)$, is measured by detecting the intensity of transmitted light, $I(\lambda)$, through a sample and contrasting this value with the intensity of the incident beam, $I_0(\lambda)$. The ratio is logarithmically related to absorption $A(\lambda)$ according to the equation:

$$A(\lambda) = -logT(\lambda) = -log_{10}\frac{I(\lambda)}{I_0(\lambda)} \tag{2.1}$$

$A(\lambda)$ can also be expressed in terms of the molar extinction coefficient, $\epsilon(\lambda)$, the concentration of absorptive species, c, and the optical path length l according to the Beer-Lambert Law:[218]

$$A(\lambda) = \epsilon(\lambda)cl \tag{2.2}$$

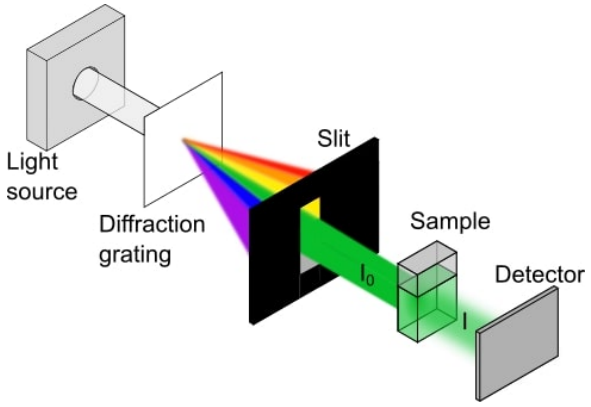


Figure 2.1: Schematic for a typical absorption spectrophotometer.

Figure 2.1 is a schematic diagram of a typical UV-visible spectrophotometer setup. White light from a continuous wave Xe lamp is passed through a diffraction grating and a slit in order to generate monochromatic light. Varying the position of the slit relative to the diffracted beam alters the wavelength of incident light $I_0(\lambda)$ which is scanned during the experiment. The intensity of transmitted light, $I(\lambda)$, at each wavelength is detected.

Absorption spectra in this thesis were measured under ambient conditions with a spectropho-

tometer, (Cary 60 UV-Vis spectrophotometer, Agilent). Film samples were measured on glass substrates and solution measurements were carried out in quartz cuvettes of 10 mm path length. Corrections to the baseline of the spectra were carried out by subtracting the absorption spectrum of either the pristine substrate (in film samples) or pure solvent (in solution measurements).

2.2.2 Photoluminesence spectroscopy

There are several potential fates for a photon that is absorbed by a photovoltaic material, one of which is its spontaneous emission and the concomitant relaxation of the material to the GS. Kasha's rule states that the rate of internal conversion from high-lying electronic energy levels to the lowest-lying ES (S_1) is significantly greater than the rate of spontaneous emission.[15] It follows that significant spontaneous emission occurs only from S_1. In photoluminescence (PL) spectroscopy, the intensity of this emission as a function of emission wavelength is measured for a given excitation wavelength.

Figure 2.2 shows a schematic diagram of a typical PL spectrometer. White light from a continuous wave Xe lamp passes through a diffraction grating and a slit in order to generate monochromatic excitation light. The light impinges on the sample and may give rise to emission which is passed through a second monochromator before detection. In typical PL measurements, a monochromatic excitation is used, with the detection wavelength scanned across a desired range to generate a spectrum of PL intensity as a function of emission wavelength. In synchronous PL measurements, the excitation wavelength is also scanned in order to generate a matrix of PL intensity as a function of both emission and excitation wavelengths.

All PL measurements presented in this thesis were carried out under ambient conditions using a commercial spectrometer. Measurements of film samples were carried out on glass substrates in a front-facing 90 ° geometry with a Fluorolog-3 spectrofluorometer (FL 3-22, HORIBA Jobin Yvon). A Cary Eclipse fluorescence spectrophotometer (Agilent) was used for PL detection of samples in solution, which were measured inside a 10 mm quartz cuvette.

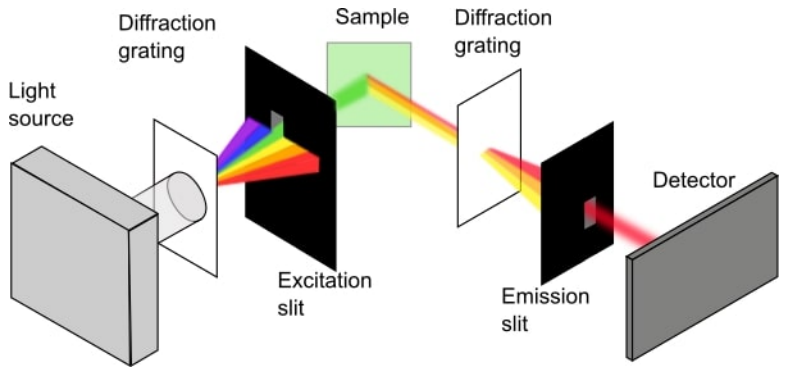


Figure 2.2: Schematic diagram of a photoluminescence spectrometer.

2.2.3 Incident photon-to-electron conversion efficiency

In photovoltaic systems, the absorption of light may result in the dissociation of free charges. When incorporated into an electrical circuit, a photovoltaic material can thus generate photocurrent, which can be detected. It is useful to measure the amplitude of photocurrent as a function of wavelength in the visible range, to determine the material's applicability to solar technology, as well as to better understand the relevant photoconversion mechanisms.

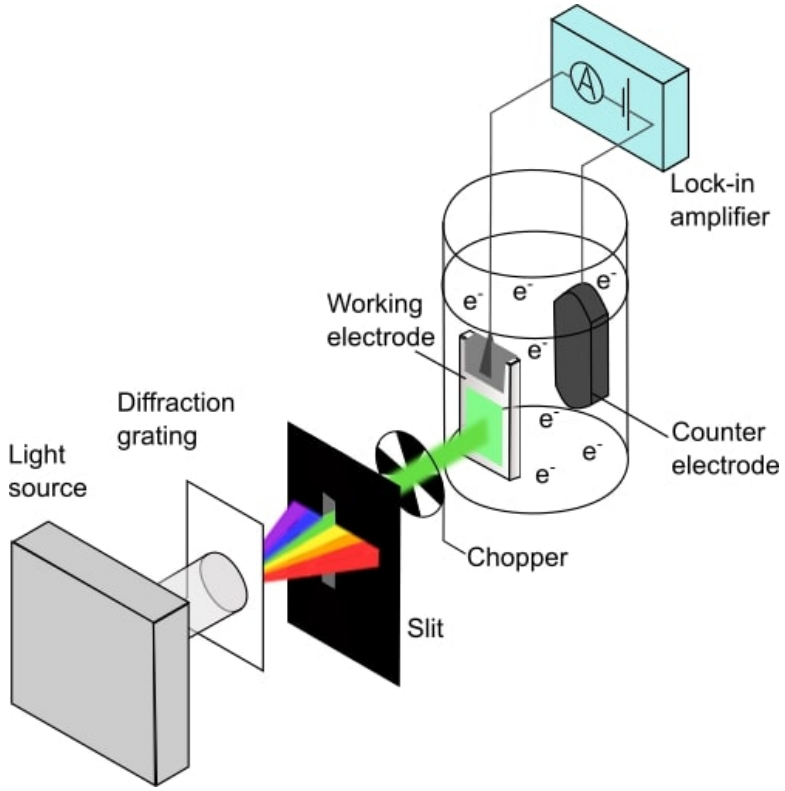


Figure 2.3: Schematic diagram of IPCE setup. e^-=electrons in electrolyte solution.

An experimental incident photon-to-electron conversion efficiency (IPCE) setup was built with the help of Nathaniel Gallop and Ziyuan Ge (Imperial College London). A custom programme for collecting data was written by Nathaniel Gallop and Ziyuan Ge using LabVIEW.

White light from a 75 W Xe lamp was passed through a diffraction grating, a 10 nm slit and a 400 nm long pass filter in order to generate monochromatic visible light. An optical chopper modulated the light. The light illuminated a working electrode, the preparation of which is discussed in section 2.1.4. The working electrode and a platinum counter electrode were submerged in electrolyte (1 mM dichlorobenzoquinone in BG-11 freshwater cyanobacterial solution, Sigma-Aldrich). A lock-in amplifier (MFLI, Zurich Instruments AG) was used to detect photocurrent by connection to the working electrode and also to apply voltage to the circuit by connection to the counter electrode. Data of photocurrent as a function of wavelength were collected using LabVIEW.

The IPCE value is equal to the ratio of number of electrons in the circuit (N_e) to the number of incident photons per unit time (N_p). It can be calculated from the raw photocurrent data according to the equation:[219]

$$IPCE(\lambda) = \frac{N_e}{N_p} = \frac{1240 \times J_{sc}(\lambda)}{\lambda \times P_{in}} \times 100 \tag{2.3}$$

where J_{SC} is the short-circuit photocurrent density (mA cm^{-2}) resulting from monochromatic light of wavelength λ (nm) and of power P_{in} (mW cm^{-2}). A custom programme was created in MATLAB for the processing of raw photocurrent data and conversion to IPCE values.

A very involved optimisation process of the IPCE setup was required in order to detect nanoamp photocurrents of cyanobacteria cells as are presented in section 5.3.1. Such current amplitudes are comparable to electronic background signals and therefore direct observation of photocurrent was often problematic due to convolution of the experimental signal with background noise. First the lock-in amplifier was implemented in order to isolate the photoinduced electronic signals. The LabVIEW code was written to allow automated measurement of repeat scans over long time periods to improve the signal-to-noise ratio, where the previously existing setup was

manually controlled. Finally, the addition of a Faraday cage to isolate the electrochemical cell allowed further exclusion of external electromagnetic radiation to reduce the background noise. The resolution of the setup was improved from the μA level to be able to detect picoamps when operating at its optimum parameters.

The setup was then further optimised with photoanodes comprising well-characterised $BiVO_4$. Photoanodes were prepared by spin-coating $BiVO_4$ onto conductive FTO coated glass by Zhu Meng (Imperial College). The resultant photocurrent spectra are presented in figure 2.4 for three different time constants for data collection, all measured with +0.5 V of applied bias. Comparison of the spectral shape to previous studies confirmed that the experimental setup was well-calibrated.[220] The baseline noise level was observed to decrease from large spikes of approximately 10 % of the peak signal amplitude with a 100 ms time constant (figure 2.4a), to negligible noise with a 2 s time constant (figure 2.4c). However, the added measurement time caused by using a long time constant caused gradual depletion of the signal due to sample degradation under external bias. It was therefore concluded that a compromising 200 ms time constant (figure 2.4b) allowed sufficient signal averaging to minimise baseline noise while simultaneously keeping the measurement time short enough that photocurrent suppression was not observed.

All of the spectra presented in figure 2.4 were measured using a 400 nm long-pass filter (LPF) after the diffraction grating in order to eliminate contributions from higher-order harmonics of the fundamental beam. However, figure 2.4d reveals that all spectra showed photocurrent signals between 700 nm and 800 nm, which are not characteristic of $BiVO_4$ according to prior reports. Repeat measurements were therefore carried out using a variety of filters in order to establish the origin of the low-energy signal. It was found that a 600 nm LPF eliminated this signal, indicating that the photocurrent detected in the 700-800 nm range actually originated from photons at 400-600 nm. Although the beam at 750 nm is theoretically monochromatic, scattering of intense higher energy photons at the diffraction grating can allow minor populations of photons of undesired energies to pass through the slit. Wavelengths above 700 nm were therefore demonstrated to be energetically ambiguous despite the use of a monochromator. Resolution of this issue could be achieved by employing various filters, adjusted according to

the desired wavelength. However, this would negate the objective of automating the measurement. It was therefore determined that experiments would be carried out only in the 400-700 nm range as to not include contributions to the signal from photons of an unknown energy.

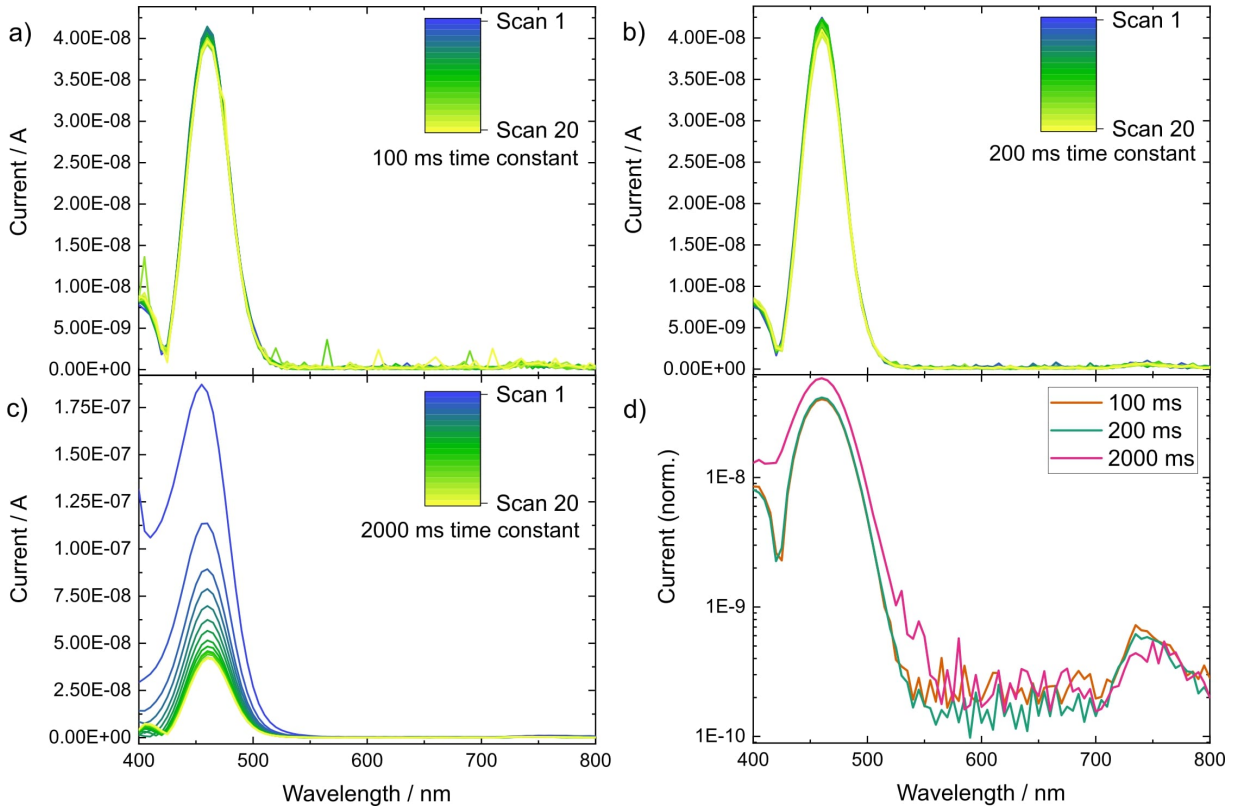


Figure 2.4: Photocurrent spectra collected in the optimisation process of the IPCE setup for $BiVO_4$ using +0.5 V of applied bias and a 100 ms (a), 200 ms (b) or 2 s (c) time constant. d): Normalised photocurrent spectra for all time constants plotted on a log scale y-axis in order to emphasise the small signal at 700-800 nm.

2.3 Time-resolved spectroscopy

2.3.1 Basic principles

Transient absorption (TA) spectroscopy is a form of time-resolved spectroscopy that can be employed to study the dynamics and mechanisms of photoinduced processes in semiconducting materials. The most fundamental subcategory of this experiment is the pump-probe measure-

ment, comprising two pulses of incident light. First a pump pulse creates a population of ESs within the material. The probe pulse follows and measures the absorption spectrum of the ESs in the sample, analogous to steady-state absorption spectroscopy. The probes discussed in this thesis all refer to broadband pulses and span either the visible region or the near-infrared region. The time delay between the pump and probe pulses is scanned throughout the experiment by mechanically varying the path length of the probe pulse with a delay stage. The ES absorption spectrum is thus measured for each of a range of timepoints after the pump. Hence by stitching together these spectra to generate a time-dependent absorption spectrum, it is possible to observe the evolution of photoexcited states as a function of time. At each timepoint, a spectrum is measured both with and without the pump in order to generate a difference spectrum depicting the difference in optical density, OD, as a consequence of excitation. This is achieved by employing an optical chopper operating at a frequency of 0.5× the repetition rate of the laser in order to block every other pump pulse. The resulting dataset is a matrix of OD as a function of both time and probe wavelength.

2.3.2 Experimental setup for 100 fs time resolution

Figure 2.5 shows the TA experimental setup used for all measurements. A Ti:Sapphire regenerative amplifier (Spectra Physics Solstice, Newport Corporation) pumps seed pulses (800 nm, <200 fs, 1 kHz) to an optical parametric amplifier (TOPAS, Light Conversion) coupled to a frequency mixer (NIRUVis, Light Conversion) to generate tuneable wavelength pump pulses. Seed pulses are also directed to a mechanical delay stage before being focussed into a crystal (Sapphire for visible probe and YAG for NIR probe) to generate a broadband probe. The probe is split into a signal beam, which continues onto the sample, and a reference beam which is directed into an optical fibre (OF) coupled sensor (a charge-coupled device for visible detection and InGaAs for NIR detection). The pump (modulated at 500 Hz) and the probe signal beam are focussed onto the same spot on the sample. The sample is contained in a nitrogen-purged cuvette for measurements. After transmitting through the sample, the probe signal is directed to a second OF coupled sensor. The signal spectrum is corrected for fluctuations in the data by

subtraction of shot-to-shot noise according to the reference probe beam. The spectrum is also averaged over several repeated scans for an improved signal-to-noise ratio. Transient spectra are processed using functions built into the software *SurfaceXplorer*, including chirp correction and the subtraction of scattered pump light and background noise.

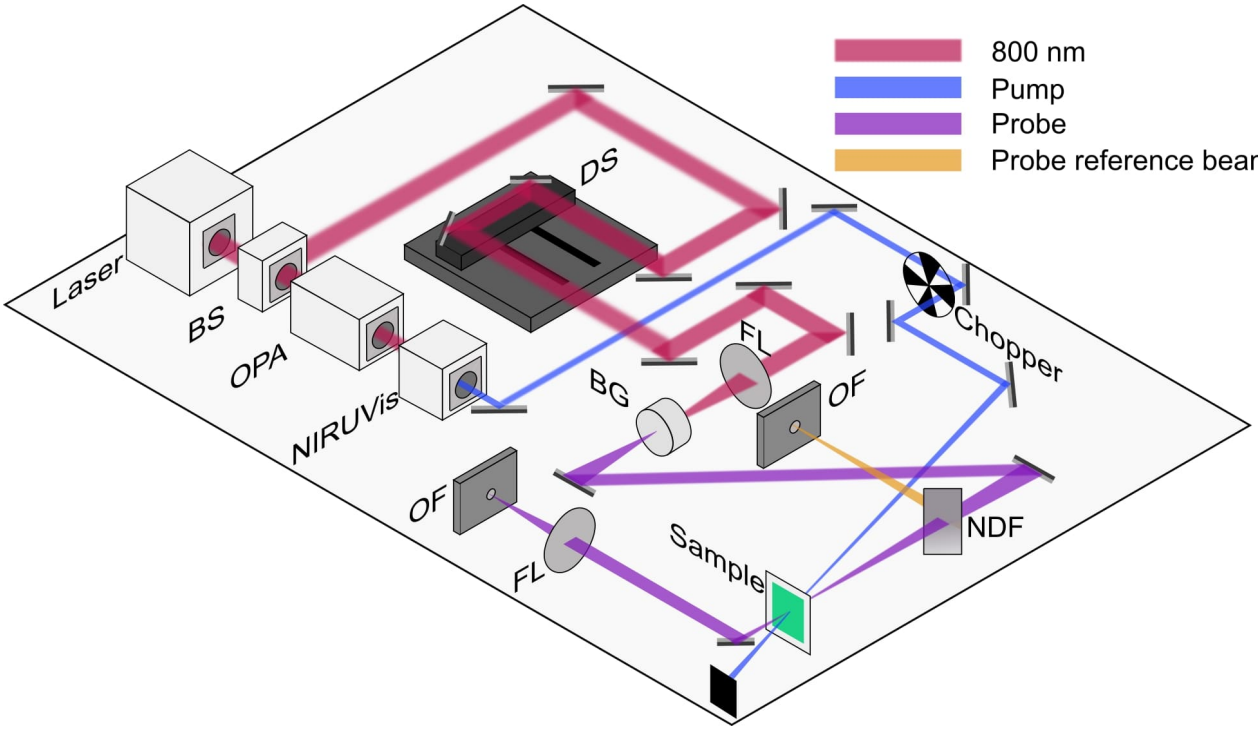


Figure 2.5: Schematic diagram of a TAS experimental setup. BS=beam splitter. OPA=optical parametric amplifier. DS=delay stage. FL=focussing lens. BG=broadband generation. NDF=neutral density filter. OF= optical fibre.

2.3.3 Interpretation of spectra

The transmittance of the probe pulse through a sample is measured with and without pump excitation in order to extract a difference in transmittance as a result of pump excitation. For each datapoint there are therefore three light intensities to consider: the intensity of the incident beam, I_0, the intensity of the beam transmitted through a pump-off sample, I_1, and the intensity of the beam transmitted through a pump-on sample, I_2. According to equation 2.1's definition of T in terms of absorbance, the change in optical density can be expressed in

terms of the relevant beam intensities:

$$\Delta OD = OD_2 - OD_1 = -log\frac{I_2}{I_0} - -log\frac{I_1}{I_0} = -log\frac{I_2}{I_1} \tag{2.4}$$

This equation can be rearranged and approximated due to the difference in light intensity being relatively small, thus arriving at the equation:

$$\Delta OD = -log(1 + \frac{I_2 - I_1}{I_1}) = -\frac{1}{2.3} \times \ln(1 + \frac{\Delta I}{I_1}) \approx -\frac{1}{2.3} \times \frac{\Delta I}{I_1} \tag{2.5}$$

This therefore gives a direct proportionality between OD and the difference in light intensity before and after the pump excited sample, $I_2 - I_1$, or ΔI. As given in equation 2.2, this can also be expressed in terms of the concentration of absorptive species within the sample. As such, it is possible to extract the relative populations of photoexcited states within a material by measuring the amplitude, ΔOD, of TA signals. Hence, the decay and growth timescales of TA signals directly reveal the lifetimes of photophysical processes within the sample and, in semiconducting materials, can thus represent the timescales of charge transfer and charge separation, amongst other processes.

The wavelength, amplitude and shape of the fundamental signals detected in a TA measurement will invariably depend on the material studied. However, the typical features can be summarised into three classes, depicted in figure 2.6.[221]

• Ground state bleach (GSB): the absorption of pump photons by the ground state excites the system to the first excited state S_1 and depletes the population of ground state species within the sample. Thus, a GSB signal gives a negative ΔOD feature which reflects the steady-state absorption spectrum of the material.

• Stimulated emission (SE): a photon from the probe pulse induces the emission of a photon from the excited state S_1, which is only notably populated following pump-induced excitation. As the emission causes a greater number of photons to impinge on the detector, SE therefore manifests as a negative ΔOD signal. Its shape typically follows the steady-state PL spectrum and is thus slightly lower in energy than the GSB due to vibrational relaxation within S_1.

• Photoinduced absorption (PIA): following pump excitation to S_1, the system may further absorb photons from the probe pulse on the condition that they are resonant with an allowed transition from S_1 to a higher-lying excited state, S_n. Due to their absorption by the sample, a decreased fraction of the incident probe photons will reach the detector therefore giving rise to a positive ΔOD signal in the TA spectrum.

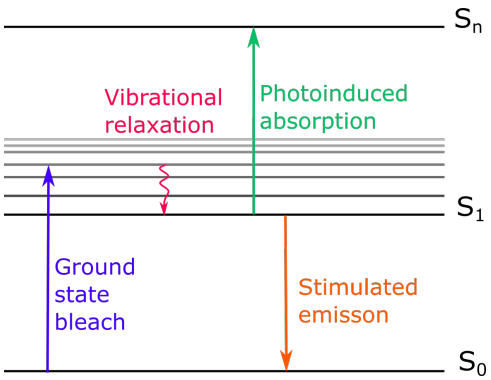


Figure 2.6: Photoinduced processes occurring on pump excitation in a TAS measurement, with typically detected signals represented by straight arrows.

From these descriptions, it follows that monitoring the amplitudes of these signals as they evolve in the time domain allows the elucidation of the growth and decay rates of excited species. TA data thereby illustrate the movement of excitation energy within a material.

2.3.4 Analysis of spectra

Unfortunately, it is incredibly rare that meaningful time-resolved signals can be directly extracted from TA spectra. This is because time-resolved spectra most often comprise features of multiple components, such as excitons of donor and acceptor species as well as free charge carriers in a typical photovoltaic blend. The inspection of the dynamics inside the spectra are hence complicated due to overlapping signals, resulting in conglomerated amplitudes and kinetics. The lifetimes of photoinduced processes cannot be accurately quantified directly from this information as the decay lifetime at a given wavelength will comprise a sum of multiple monoexponential components evolving in time.

In these cases, global analysis (GA) is implemented in order to deconvolute spectra into separate

photophysical components which may be assigned to species with distinct kinetics. It is then possible to extract the necessary information in order to derive photophysical models and build a story of the excited state processes within a material. This method is especially crucial in complex systems such as biological species where a huge number of charge and energy transfer processes occur simultaneously with similar energetics, and the extent to which they affect each other is not precisely understood.

GA is carried out by employing a computational algorithm denoted a genetic algorithm due to its imitation of Darwin's "survival of the fittest" model.[222] For a time-resolved spectrum represented by a matrix representing change in optical density ΔOD as a function of i probe wavelengths (λ) and j time delays (t):

$$\Delta OD(\lambda_i, t_j) = OD_{ij} \tag{2.6}$$

a global fitting algorithm is applied to fit the data. The number of linearly independent components, n, is determined as an input parameter. A population of non-identical guesses of OD_{ij} for each of n is generated and modelled as an monoexponential function of t. The weighted sum of squared residuals is determined by a non-linear least-squares method in order to evaluate the quality of the fit for each guess.

The best fit is selected for each component and a new population of spectra is generated by the random addition of gaussian functions to the spectrum. The spectra with the lowest residuals are "bred" together and this process is iteratively repeated until the algorithm converges on a spectrum for each of n that fits sufficiently well to be accepted, according to a threshold of residuals. The evolution of the resulting spectra in the time domain is then calculated to give the kinetics for each component.

Variable parameters for the algorithm include reference spectra and guess spectra which may be fed into the algorithm in order to steer the iterations towards meaningful results. A reference spectrum is fixed throughout the calculation and does not undergo the evolutionary process. This differs from a guess spectrum which provides a starting point however is not fixed and does

undergo the evolutionary process. References and guesses can be extracted from the spectra of the neat materials within the studied blends at very early times (0.5–2 ps, averaged to reduce noise) to provide pure excitonic components. Alternatively, they can also be obtained from blend spectra at very late times (approximately averaged over 1 ns between 3-6 ns) when it is assumed that all species other than free charges have decayed entirely, in order to provide pure charge components.

Despite the rigorous procedure, the outcome of a GA operation can be completely dependent on the input parameters rather than there existing one correct mathematical solution to the fit which also makes physical sense. GA robustness is hampered by a number of typically occurring challenges including (but not limited to) stark differences in signal amplitudes, overlapping spectral features and data noise. These are common; it is widely accepted that the computational deconvolution of time-resolved spectra affording kinetic components which can be assigned to physical processes is non-trivial.[223] Therefore many different iterations of the input parameters, yielding many possible methods for each GA reconstruction presented in this work, had to be trialled. The results that best described the dynamics within the system were selected according to expectation of physically meaningful kinetics and timescales, as well as comparison of component spectra to those of neat materials in order to verify their validity.

2.3.5 Transient absorption spectroscopy with sub-10 fs pulses

TAS as described above allows the interrogation of ultrafast processes on the picosecond to nanosecond timescale, elucidating the photophysical behaviours of many systems. However, sub-picosecond processes are obscured by the instrument response function arising due to pulse durations of approximately 100 fs. In order to investigate photoinduced processes with femtosecond timescales, pulses can be temporally compressed in order to achieve higher time resolutions. Employing ultrashort pulses enables the creation of a coherent superposition of states on photoexcitation by the pump, as well as granting access to observe the temporal evolution of this coherent superposition of states.

Pulses with ∼100 fs duration are passed through an argon-filled hollow fibre to achieve spectral

broadening owing to the Kerr non-linearity of the medium.[224] A pulse propagating through the fibre experiences intensity-dependent phase shifts due to the intensity-dependent refractive index of the medium. Varied transmission phases are therefore established for the different intensities across the pulse, resulting in frequency broadening. The spectrally broadened pulse is guided to a pair of chirped mirrors for temporal compression, producing a broadband (395-420 nm) pulse of under 10 fs duration.

Application of this method to the classic pump-probe technique allows a much finer time resolution which enables observation of oscillations to the signal due to the temporal evolution of the vibrational wavepacket. Projection of the time-dependent signal onto the frequency domain by the Fourier transform affords a spectrum presenting peaks at energies corresponding to the oscillation frequency. The peaks are resonant with frequencies of vibrational degrees of freedom exhibited by the studied system, thus generating the vibrational spectrum of the electronic state. An example is illustrated in figure 2.7 for a photoinduced absorption signal.

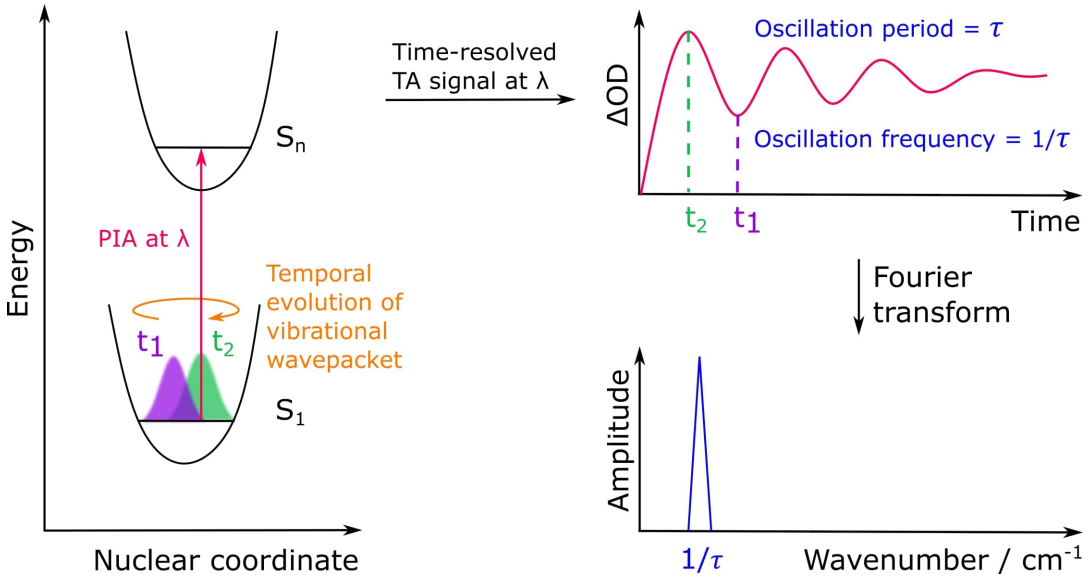


Figure 2.7: Diagram illustrating the origin of oscillations in time-resolved spectra and the reconstruction of the vibrational spectrum by Fourier transformation. Wavelength of photoinduced absorption (PIA) is given by λ.

2.4 Time-correlated single photon counting

Incorporating time-domain resolution into PL spectroscopy allows the direct observation of the temporal evolution of emissive processes. Time-resolved PL measurements probe radiative recombination pathways in photoexcited materials by measuring the decay of PL intensity over time after an initial photoexcitation process. This technique therefore measures a decay lifetime (τ) for the detected emission, which is equal to the time taken for the PL intensity to decay to $1/e$ of its initial intensity. This lifetime can be expressed as the reciprocal of the sum of the rate constants for radiative and non-radiative recombination processes according to the equation:

$$\tau = \frac{1}{k_r + k_{nr}} \tag{2.7}$$

where k_r and k_{nr} are rate constants for the processes of radiative and non-radiative recombination, respectively.

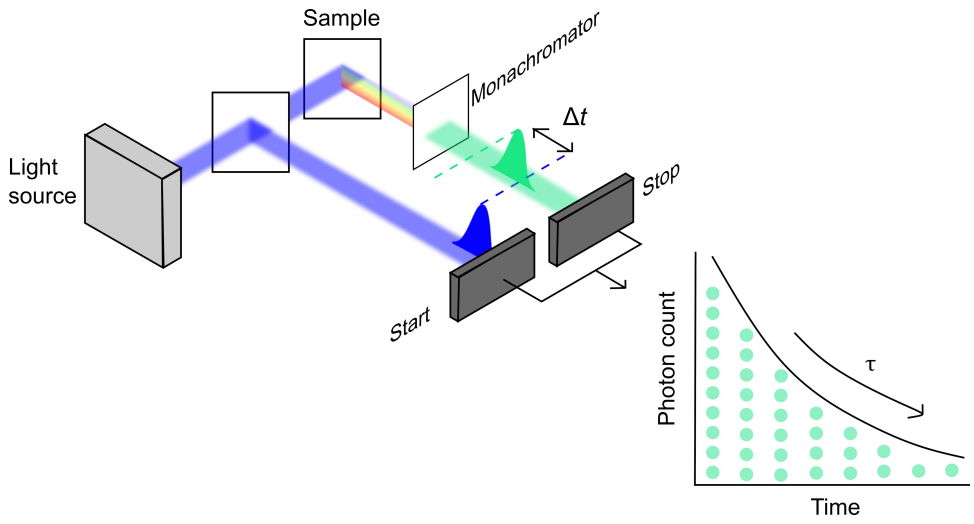


Figure 2.8: Schematic diagram of a TCSPC experimental setup.

To measure time-resolved PL intensity, the time-correlated single photon counting (TCSPC) method is most commonly employed and is depicted schematically in figure 2.8. A diode emits excitation pulses (∼100 ps, ∼MHz) which activate a time digitiser on reaching a photomultiplier detector denoted the "start" detector. The excitation pulse also impinges on the sample, initiating the fluorescence of photons which are passed through a monochromator, fixed to pass

photons of a single emission wavelength of interest for the experiment. The monochromatic emission is then collected by a sensitive photomultiplier "stop" detector which terminates acquisition on detection of a single photon. The time delay, Δt, between the excitation photon and the emitted photon reaching their respective detectors is thus recorded. This single photon process is repeated and a histogram is plotted representing photon counts at each Δt, the shape of its decay curve depicting the fluorescence decay lifetime τ.

Chapter 3

Regioisomeric molecular tuning of small molecule-based OPVs

3.1 Context and motivation

The bulk heterojunction (BHJ) is universally recognised as the optimum active layer structure for OPV device efficiency.[225] Pure domains of donor (D) and acceptor (A) components in a BHJ manifest the best possible charge carrier mobility and minimum charge carrier recombination. Meanwhile, the large area of D:A interface ensures a high quantum yield of charge separation. Device performances are hence strongly influenced by donor-acceptor blend morphology, with key roles being played by domain size, domain purity and charge transport efficiency.[226] Domain size is significant due to its correlation with the proximity of generated excitons to domain boundaries; if photoexcitation occurs too far from a D:A interface then exciton recombination is more likely, thus favouring smaller domains. A trade-off exists between this effect and the fact that large crystalline domains afford the best charge carrier mobility and minimum bimolecular recombination.[227–229] It is understood that better domain purity results in a higher amplitude of charge generation,[230] with evidence revealing a drop in device performance in over-mixed blends containing both fullerene and NFA components.[231–233]

In many examples, the chemical structure of molecular components has been seen to influence

the nanoscale morphology of D:A blends.[234–236] Small molecule solar cells have recently risen to the forefront of OPV research, largely due to the ease of chemical structure modification and control compared to polymers, which exhibit larger degrees of batch-to-batch variation.[237–241] The focus on the molecular tuning of small molecule components in OPV blends now sees the PCE of devices typically exceeding 10 %.[242] Computational modelling can inform the effects of molecular modifications on these properties to an extent.[38,243–246] However, understanding the nuances of the relationship between molecular structure and photovoltaic performance in practice can grant us the power of direct design of photovoltaic components in order to achieve desired effects.

The ability to fine-tune the electronic and optical properties of a material is especially accessible in push-pull organic molecules. These comprise alternating D and A moieties, separated by a conjugated π-system. In the ADA configuration the electron-donating core is flanked by electron-withdrawing groups. This class of small molecule facilitates efficient intramolecular charge transfer, which can be controlled by structural modification of the D and A groups to increase or decrease their electron-donating or withdrawing ability. As such, it is possible to realise the optimum electronic and optical properties of the molecule.[169] Additionally, it is possible to adjust the intra- and intermolecular forces and as a result control the domain crystallinity and morphology that arise when the small molecule components are incorporated into photovoltaic blends.[247]

3.1.1 Conformational twisting in a push-pull small molecule

This chapter presents an investigation into the effects of a minor structural modification on a small molecule based on a benzodithiophene (BDT) core, which is well-studied in its molecular design and the consequences on resulting optoelectronic properties.[248] The BDT unit is one of the most prevalent components in OPV materials due to the planar, rigid conjugated structure which favours intermolecular $\pi - \pi$ stacking thus benefiting charge transport.[249,250] BDT first appeared in the OPV field in 2008 when it was shown that the optical and electronic properties of BDT-containing polymers could be easily tuned.[251] Chen et al. then achieved a PCE of 5

% with a BDT-based small molecule solar cell in 2011, with x-ray diffraction data suggesting that efficient charge transport was established by a highly crystalline domain morphology.[252] They went on to show that the solubility, molecular organisation, frontier molecular orbital energy levels, absorption spectra and blend morphology can all be influenced by manipulating the side-chains of the BDT core unit,[253,254] with prominent successes of side-chain modification eventually achieving PCEs of 9.58 %[255] and 9.3 %.[256]

A small molecule derivative of BDT was reported by Liu et al., in which a BDT core is bonded to four moieties, two of which are octyl-disubstituted thiophene units and two are 3-oxo-2,3-dihydroinden-1-ylidene units. Two regioisomers of this structure were studied and are shown in figure 3.1, with the octyl chain represented as **R**. Denoted BTCN-M and BTCN-O, the molecules are structurally identical except for a 1-carbon displacement of an octyl chain on the peripheral thiophene rings. Octyl chain substitutions are found at the 3- and 5- carbon positions in BTCN-M (denoted a "meta substitution") while the chains are found on the 4- and 5- ring positions on BTCN-O (giving an "ortho substitution").

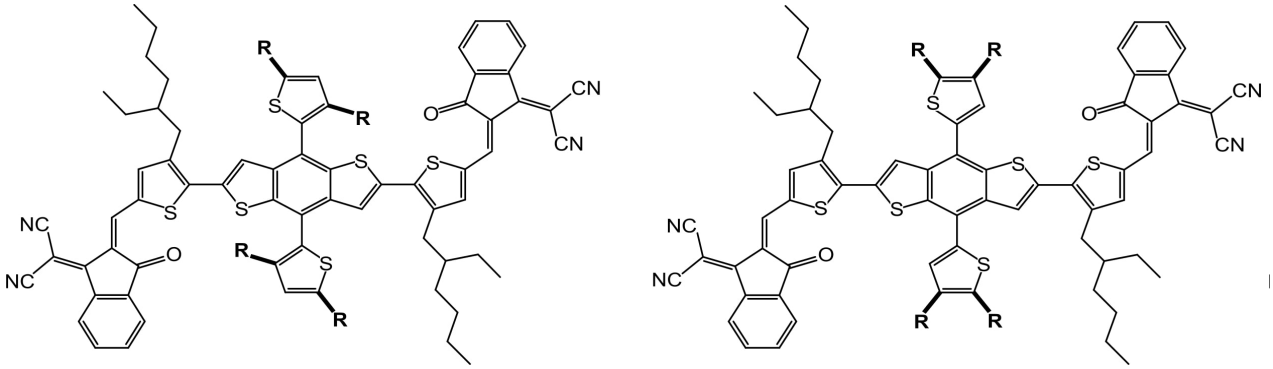


Figure 3.1: Structures of BTCN-M (left) and BTCN-O (right), with octyl chains (represented by **R** for figure clarity) at meta and ortho positions to each other respectively.

The different positioning of the bulky alkyl chains causes dramatic consequences for the molecular conformation of the two molecules. The substituted thiophene unit is far narrower in BTCN-O compared to BTCN-M, where one of the octyl chains extends towards the electron-withdrawing moieties in the latter case. This steric hindrance in the meta relationship manifests a greater energetic barrier to rotation of the thiophene ring about the chemical bond to BDT, relative to the ease of rotation in the ortho-positioning. This prevents BTCN-M from accessing a planar configuration of the peripheral thiophene ring relative to the central BDT unit. This

was confirmed by Liu et al. using density functional theory (DFT) calculations to determine the molecular energy as a function of the dihedral angle about the thiophene-BDT bond. For the meta relationship, the totally planar conformation (where the thiophene ring lies parallel to the core BDT unit) was found to have an energy of 110 kJ mol^{-1} above its lowest energy conformation, compared to just a 35 kJ mol^{-1} barrier to rotation in the ortho-substituted molecule. BTCN-O thus achieves a planar conformation across the entire molecule much more readily than BTCN-M.[257] BTCN-O therefore exhibits greater $\pi - \pi$ stacking between molecules, which is enhanced by planar conformations of the aromatic π groups, than BTCN-M in bulk. Grazing incidence wide-angle x-ray scattering (GIWAXS) studies have confirmed a greater degree of π-π stacking in BTCN-O than BTCN-M, as well as showing enhanced crystallinity in domains of BTCN-O-containing blends.[214]

Liu et al. found that this minor difference in the two molecules' chemical structures causes them to behave with opposite functionalities when blended with the benchmark donor polymer poly[(2,6-(4,8-bis(5-2(ethylhexyl)thiophen-2-yl)-benzo[1,2-b:4,5-b']dithiophene))-alt-(5,5-(1',3'-di-2-thienyl-5',7'bis(2-ethylhexyl)benzo[1',2'-c:4',5'-c']dithiophene-4,8-dione)] (PBDB-T) or acceptor [6,6]-phenyl-C71-butyric acid methyl ester ($PC_{71}BM$). The investigation entailed blending each of the small molecules in figure 3.1 with both PBDB-T and $PC_{71}BM$ separately, providing four blends in total and investigating their device performances. It was found that BTCN-O exhibited much greater performance when blended with $PC_{71}BM$ compared to when blended with PBDB-T and hence performs better as a donor component. Conversely, BTCN-M demonstrated an inverted preference for $PC_{71}BM$ and therefore performs better as an acceptor.[257]

This chapter describes the work carried out to justify these performance differences in terms of the charge carrier dynamics within the four blends, with reference to morphological consequences of the structural modification. In this work, transient absorption spectroscopy was carried out in order to determine the excited state dynamics. Subsequently global analysis was applied to extract specific amplitudes and kinetics for excitons and charges in the respective blends. The results of global analysis reveal that analogous BTCN-O and BTCN-M blends exhibit comparable exciton quenching and charge formation dynamics but differ vastly in their

charge recombination dynamics, giving rise to the observed contrast in device performances. These differing charge recombination dynamics are herein rationalised in terms of the disparity in $\pi - \pi$ stacking.

3.1.2 Chalcogen substitution in an example non-fullerene acceptor

Another subset of small molecules that is of increasing interest to the OPV field and offers remarkable tuneability is NFAs. The band gap of a NFA can be tuned in order to attain absorption of near-infrared light, which ensures minimum waste of photons accounting for the low-energy edge of the solar spectrum. The maximum open-circuit voltage of a device comprising NFAs can be achieved by tuning the NFA's electronic properties with respect to the electronic properties of the donor component.[258] Furthermore, the morphology of a blend composed of a NFA with a donor component can also be controlled by fine tuning the molecular structure in order to adjust intermolecular interactions.[226] As such, devices comprising small molecule NFAs now regularly demonstrate PCEs of over 11 %.[101]

The push-pull molecular motif has also achieved and maintained popularity in the NFA field. The indacenodithiophene (IDT) unit emerged as a prominent building block in this family of molecules, with IEIC being one of the first NFAs to incorporate it in 2014.[259] The derivative of IEIC that has received the greatest attention is ITIC, shown in figure 3.2, initially exhibiting a PCE of 6.8 %.[260] ITIC has an electron-rich core comprising a conjugated series of fused thiophene, cyclopentadiene and benzene rings flanked by quaternary carbon centres bonded to para-alkyl substituted aromatic rings. Electron-deficient 1,1-dicyanomethylene-3-indanone (DCI) moieties bookend the core, granting the molecule efficiency of intramolecular charge transfer. Possible structural customisations available to the ITIC subset of NFAs and their effects on photovoltaic proficiency have been widely studied.[261] Notable implementations of ITIC include PCEs of 11.34 % and 11.2 % when blended with polymer donors PBQ-4F[262] and PBDB-T[263] respectively. Molecular tuning of ITIC derivatives has shown some focus on the morphological influence of conjugation length. Larger conjugated structures favour $\pi - \pi$ stacking and aggregation, with an optimum balance being achieved between too much

aggregation, giving rise to exciton recombination, and too little aggregation, which offers poor charge transport through the material.[101]

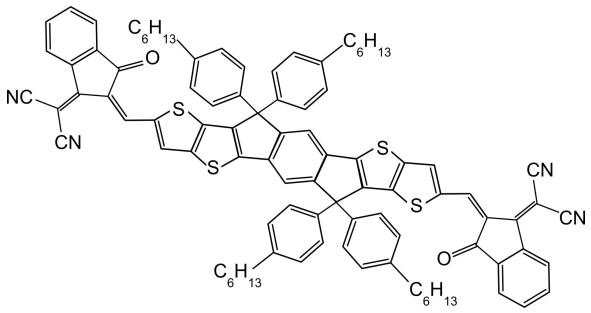


Figure 3.2: Structure of the commonly employed NFA molecule, ITIC.

The second study in this chapter investigates the effects of a regioisomeric structural modification on ITIC. Two derivatives of ITIC were studied where in both cases the para-alkyl benzene substitution is instead a meta-alkoxy substitution, and two of the four sulfur positions on the conjugated backbone are replaced by selenium atoms. In the isomer 3,9-bis(2-methylene-(3-(1,1-dicyanomethylene)indanone))- 4,4,9,9-tetrakis(3-((2-ethylhexyl)oxy)phenyl)-diseleno[2,3-d:2,3-d]-s-indaceno[1,2-b:5,6-b]dithiophene, hereafter referred to as SeIn, the internal thiophene ring bears this substitution whereas 3,9-bis(2-methylene-(3-(1,1- dicyanomethylene)indanone))-4,4,9,9-tetrakis(3-((2-ethylhexyl)-oxy)phenyl)dithieno[2,3-d:2,3-d]-s-indaceno[1,2-b:5,6-b]-diselenophene, hereafter referred to as SeOut, denotes the isomer with the substitution on the external thiophene ring. The structures of the studied molecules are shown in figure 3.3.

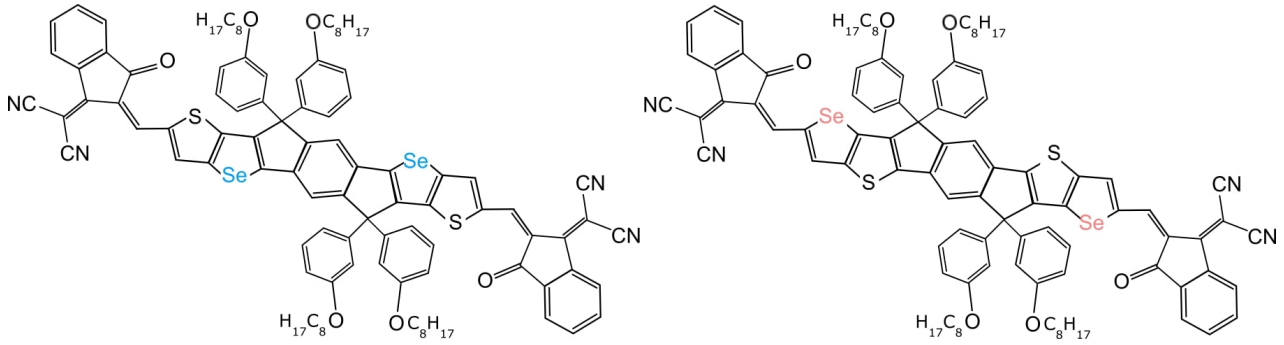


Figure 3.3: Structures of ITIC derivatives SeIn (left) and SeOut (right).

Selenium exhibits greater polarisability relative to sulfur and therefore the larger and more diffuse atomic orbitals form stronger non-covalent interactions with nearby atoms. Se atoms also experience weaker chemical bonding to vicinal carbon atoms than S atoms which reduces

aromaticity over the chalcogenophene. Furthermore, it is understood that this reduction in aromaticity raises the HOMO level slightly and hence narrows the band gap of the NFA.[101] However, the influence of altering the specific position of a Se substitution has not been investigated to date.[62]

As an investigation into the effect of the regioselectivity of this chalcogenophene substitution, this chapter discusses the difference between these two NFAs with a focus on their charge dynamics and photophysical properties. The NFAs were each assessed as acceptor components in photovoltaic blends and hence were each blended with the benchmark donor polymer PBDB-T. Transient absorption spectroscopy was used to measure the photoinduced dynamics of the two blends and global analysis was employed to extract spectra and kinetics pertaining to the excitonic and free charge species within the blends. This study reveals that the inner selenium position effects faster charge separation relative to the outer selenium position. This observation is rationalised in terms of a greater crystallinity in domains of SeOut relative to SeIn resulting in larger domains and hence a longer path for the exciton to meet an interface with PBDB-T.

3.2 Experimental details

3.2.1 Sample preparation

All samples studied were prepared according to the description in section 2.1.1.

3.2.2 Steady-state absorption spectroscopy

Steady-state absorption spectra were measured for all samples using the instrument outlined in section 2.2.1.

3.2.3 Transient absorption spectroscopy

Transient absorption (TA) spectra were obtained using the experimental setup outlined in section 2.3.2. For the results presented in section 3.3.1, the TA spectra were measured by Dr Tom Hopper (Imperial College London).

3.3 Results and discussion

3.3.1 Conformational twisting in a push-pull small molecule

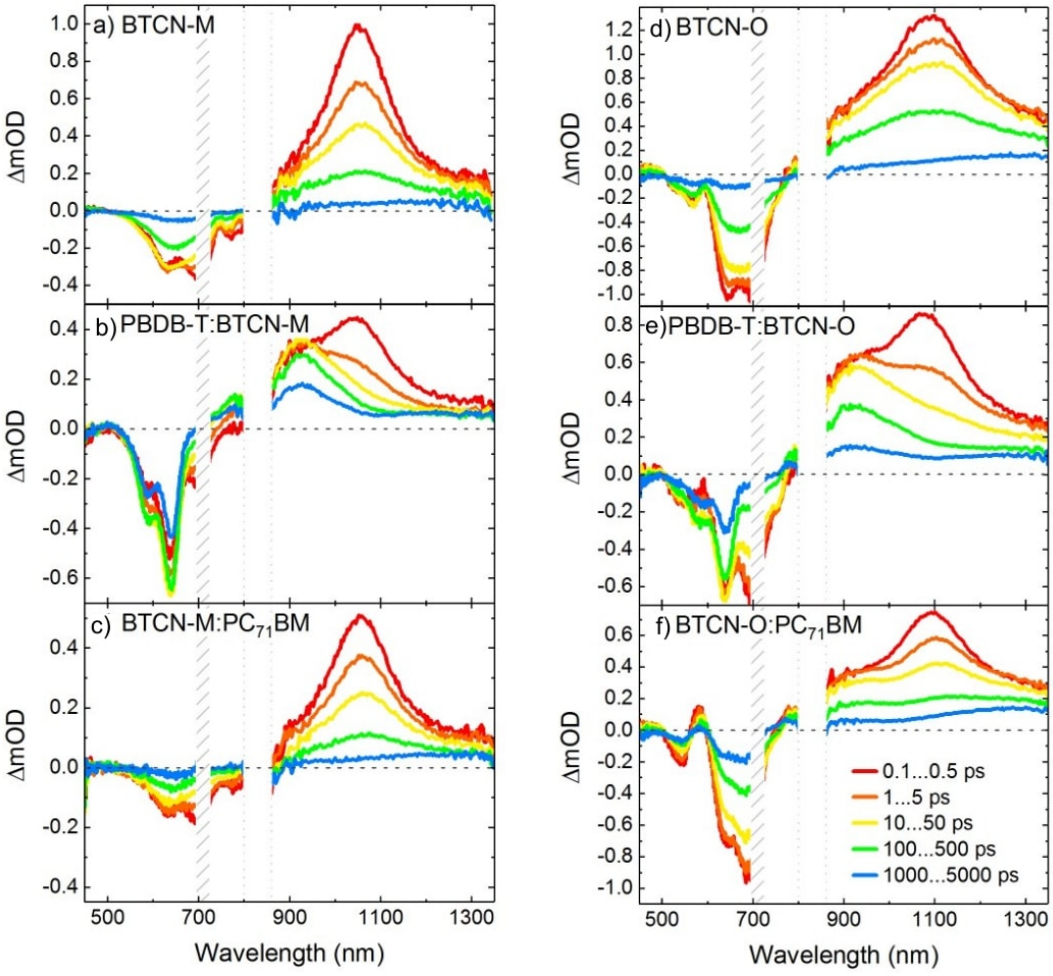


Figure 3.4: Spectra at selected time points for BTCN-M (a) and BTCN-O (d) and blends (b, c and e, f respectively) following 710 nm excitation. The greyed out region at 700 nm is included to remove pump scattering for clarity. Figure adapted from ref. 214 with author's permission.

Figure 3.4 shows ultrafast spectra for BTCN-M, BTCN-O and associated blends at selected

timepoints. The spectra were collected following excitation at 710 nm. This pump wavelength was selected due to resonance with ground state absorption by BTCN-O and BTCN-M as well as negligible absorption by PBDB-T and $PC_{71}BM$ at this wavelength. All spectra contain a large positive feature due to a photoinduced absorption (PIA) on the BDT core which occurs at 1050 nm in BTCN-M blends and 1100 nm in BTCN-O counterparts. A ground state bleach of the same molecular unit gives rise to the negative signal observed at 600–700 nm. The positive feature at large wavelengths discernible only at late times demonstrates generation of free charges within the blends. It is evident that overlapping features give rise to intertwined dynamics that do not accurately characterise the lifetimes of the photophysical species present, specifically of the large PIA signal and free charges. Hence global analysis (GA) was applied in order to deconvolute the separate components making up the spectrum.

The IR region comprises positive features assigned to both excitons and charges and hence it was selected for analysis as the most informative window. Figure 3.5 shows reconstructed spectra generated by GA for the different blends, with each material comprising two components, assigned to excitons and charges. The excitonic feature for each material was extracted from the spectrum of neat BTCN-M/BTCN-O at early times and used as the reference, while the charge spectrum was freely optimised. The exciton spectra are consistent across all six materials and the charge spectrum for each BTCN-M material is highly comparable to its BTCN-O counterpart. The global analysis method extracts only the best mathematical model to the data; it falls to the user to identify where this mathematical description meets with a model that also makes the most physical sense. The consistency of the spectra across the different materials shows that they accurately represent a meaningful photophysical component and hence this validates the respective spectral assignments.

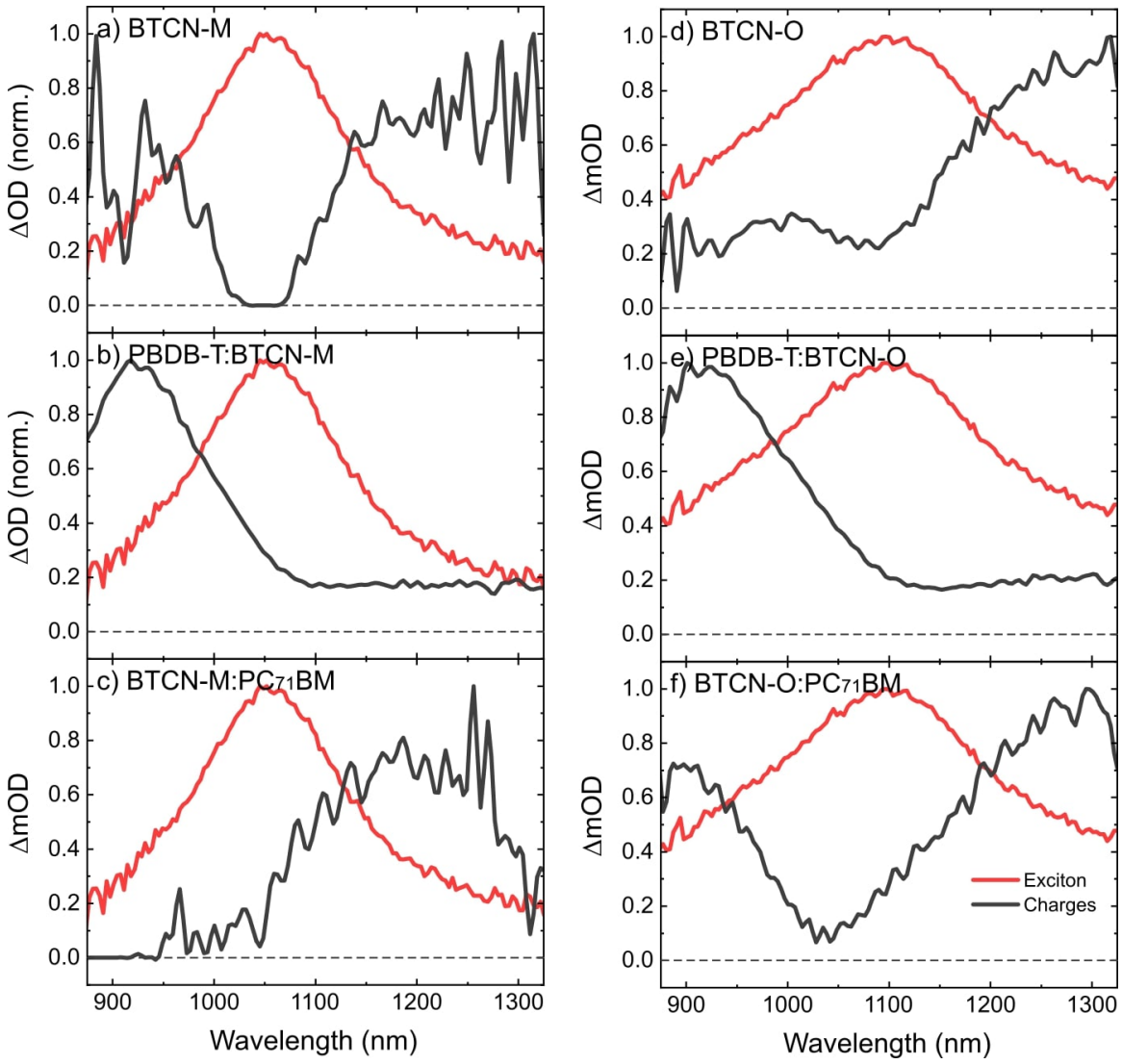


Figure 3.5: GA-reconstructed spectra featuring excitons (red) and charges (black) for BTCN-M (a), BTCN-O (d) and blends (b, c and e, f respectively). Amplitudes are normalised to the maximum of each spectrum. Figure adapted from ref. 214 with author's permission.

Figure 3.6 shows the GA-derived kinetics corresponding to the spectra in figure 3.5. First observing the traces for BTCN-M and blends, the rate of exciton quenching (depicted by the rate of decay of the red trace) in BTCN-M appears unaffected by blending with $PC_{71}BM$ but occurs on a faster timescale in PBDB-T:BTCN-M. Furthermore, as represented by the normalisation constant, the amplitude of charges per exciton is comparable for the neat material and BTCN-M:$PC_{71}BM$ and thus the number of charges formed in the BTCN-M:$PC_{71}BM$ blend (where BTCN-M acts as a donor) is negligible. Conversely, the amplitude of charges formed by PBDB-T:BTCN-M (where BTCN-M takes on the role of acceptor) is significant. However, this can be seen to decay to a low population on the 6 ns timescale of the experiment.

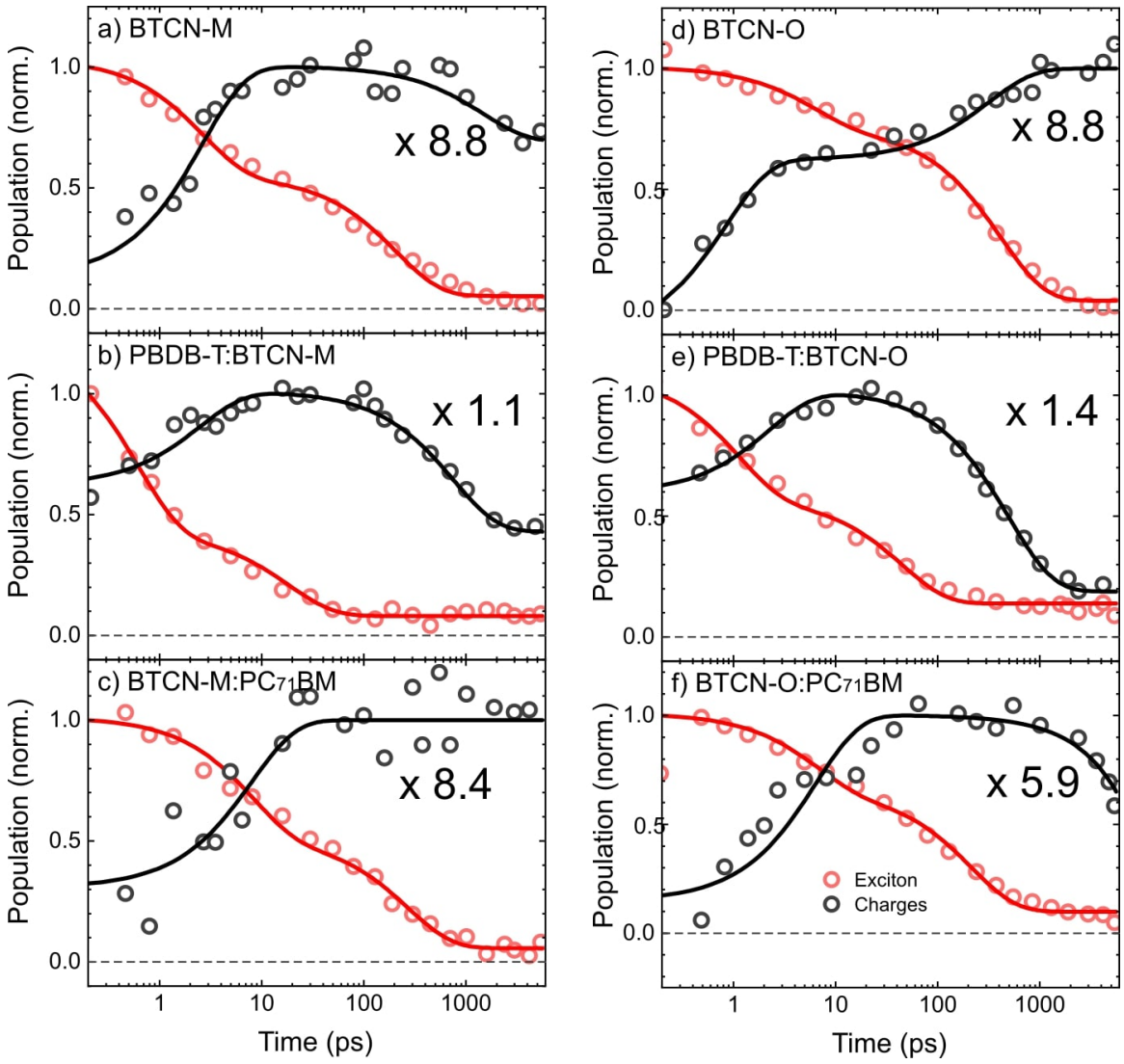


Figure 3.6: Kinetics of photophysical components in BTCN-M (a), BTCN-O (d) and blends (b, c and e, f respectively). The factor of normalisation of the charge component is included for amplitude comparison. The red trace describes exciton decay while the black trace shows charge dynamics. Multiexponential fits are included as a guide to the eye. Figure adapted from ref. 214 with author's permission.

Parallel observations can be made for BTCN-O. Exciton quenching timescales for the neat material and for BTCN-O:$PC_{71}BM$ are approximately equal while a much shorter lifetime is observed in PBDB-T:BTCN-O. A high amplitude of charges is observed for PBDB-T:BTCN-O relative to the neat material and in this case this decays entirely to zero on the timescale of the experiment. The amplitude of charges is again low in the $PC_{71}BM$ blend for BTCN-O, alike its BTCN-M counterpart, however in this case it is somewhat greater than that of the neat material. Moreover BTCN-O:$PC_{71}BM$ is the only material where a non-negligible population of charges is generated and does not decay entirely on the timescale of the experiment.

Drawing on these observations the following can be stated to explain the trend in device performances observed by Liu et al.[257] As BTCN-O:$PC_{71}BM$ is the only blend with any significant amplitude of charges surviving longer than 6 ns, the device built from this blend yields the best performance with a PCE of 7 %. The two PBDB-T blends demonstrate intermediate device performances at 6 % and 2 % PCE for BTCN-M and BTCN-O respectively; they exhibit fast exciton quenching and therefore efficient generation of free charges. However, despite the large population of free charges generated, the device performances are unimpressive due to subsequent rapid recombination of these charged species. With a PCE of 0.3 %, the worst performing blend is BTCN-M:$PC_{71}BM$, which has a negligible population of charges and thus exhibits poor optoelectronic behaviour.

Combining the excited state dynamics obtained from TA spectra with previously published morphological data[229] it is possible to understand these observations in terms of molecular rationalisations. Due to the strong $\pi - \pi$ stacking between planar BTCN-O molecules, there is some partial segregation between donor and acceptor in the best performing blend. This gives rise to a morphology of sufficiently intermixed donor and acceptor domains which aids charge separation while crystalline regions of $\pi - \pi$ stacked BTCN-O and clusters of $PC_{71}BM$ facilitate subsequent charge transport within the domains. Comparably, the lack of $\pi - \pi$ stacking between twisted BTCN-M molecules in its blend with $PC_{71}BM$ gives rise to a dominance of fullerene clusters causing excessively strong phase separation. This prevents excitons from reaching a donor:acceptor interface and thus causes slow exciton quenching. In PBDB-T:BTCN-M, low $\pi - \pi$ stacking affords an excessively amorphous morphology, responsible for the efficient exciton quenching but also for the strong geminate recombination of charges. For PBDB-T:BTCN-O, the strong $\pi - \pi$ stacking in combination with polymer chains gives rise to aggregation of materials again leading to strong geminate recombination due to the rate of recombination outcompeting the rate of charge separation in large domains. Hence it is demonstrated how a seemingly negligible structural alteration can modify how a molecule behaves when blended and ultimately invert the device performance trends observed.

3.3.2 Chalcogen substitution in an example non-fullerene acceptor

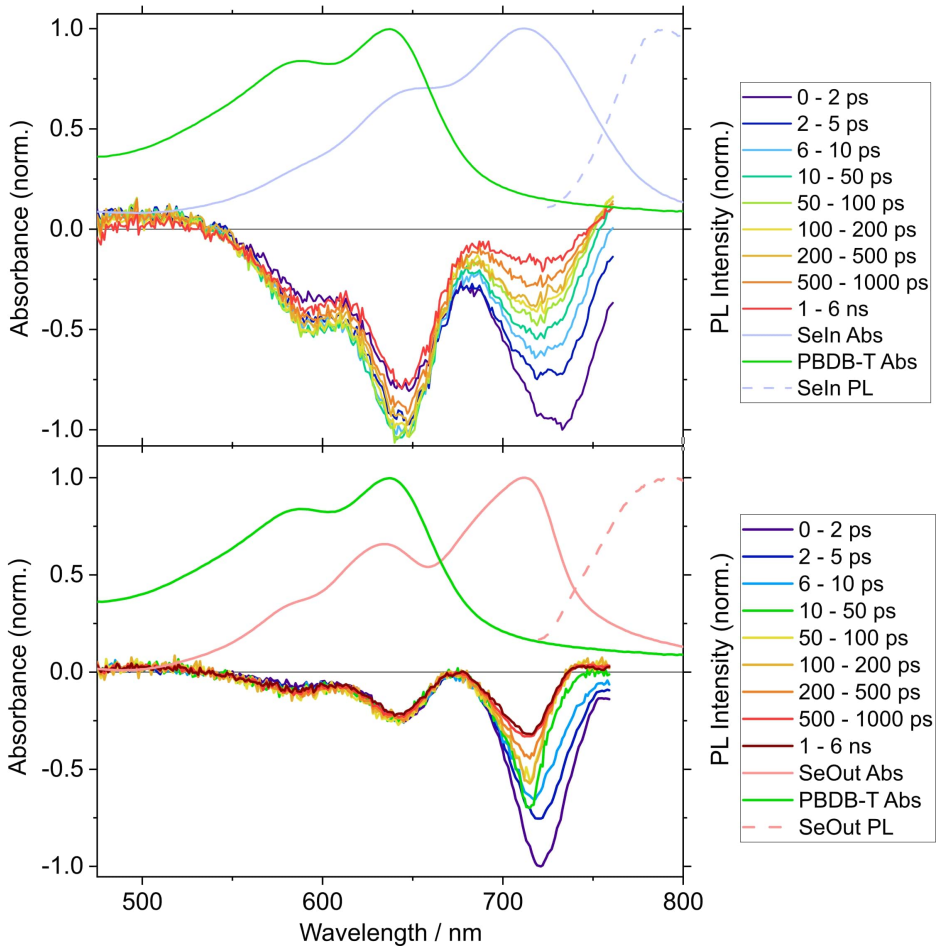


Figure 3.7: TA spectra (negative signals) following 725 and 720 nm excitation of SeIn (top) and SeOut (bottom) respectively, both blended with PBDB-T, shown alongside the visible absorption and photoluminescence spectra (positive signals) of the respective materials. Adapted from ref. 62 with author's permission.

Figure 3.7 shows the time-resolved absorption spectra following 725 nm and 720 nm excitation for SeIn and SeOut respectively (corresponding to NFA absorption maxima) when blended with PBDB-T. The excitation wavelength was selected in order to ensure direct pump-induced excitation of the ground state absorption of the NFA molecules as well as negligible absorption by the donor component. For comparison, the plots are overlaid with those of the ground state absorption spectra of the neat materials in the respective blends. Both blends show a large ground state bleach at the most prominent absorption of the neat NFA, found at approximately 725 nm. As there is negligible absorption by PBDB-T at this wavelength region, this initial pump-induced absorption can be assumed to be an excitonic component, accounted for wholly

by the NFA ground state absorption. Unsurprisingly, therefore, a steady decay over the 6 ns timescale of the experiment is observed in both cases for this spectral feature. Moreover, a blueshift of this peak can be observed in both blends before 10-50 ps.

The two higher-energy features of the ground state absorption spectrum are far more prominent in SeIn than SeOut, but it is clear in both cases that these spectral regions do not comprise exclusively excitonic components as the kinetics do not exhibit steady decay like those of the 725 nm bleach. In PBDB-T:SeIn there is an evident growth in signal until around 50-100 ps and a subsequent decay, with a large proportion of the feature's amplitude persisting at 6 ns. This spectrum also reveals a positive PIA feature at wavelengths below 550 nm, with rising and then decaying kinetics. PBDB-T:SeOut displays no evolution in the bleach features in the region of 550-675 nm within the signal-to-noise limits of the measurement. This spectrum also contains the PIA feature at the high energy edge of the spectrum, although again it has a far less significant amplitude than its SeIn counterpart. The multidimensional kinetics observed in the region below 675 nm can be attributed to the fact that both the donor and acceptor materials absorb at these wavelengths and therefore there are multiple photophysical contributions to the amplitude and evolution of the features.

Global analysis was applied in order to deconvolute the photophysical components in the time-resolved spectra. The resultant normalised exciton and charge spectra for each blend are shown in figure 3.8. In both cases, the technique identified two components, which were assigned to the blends' respective excitons and charge carriers. The excitonic component was assigned as such due to its spectral resemblance to the steady-state absorption spectrum of the neat NFA. In each case the charge carrier spectrum does not appear as an excited state absorption but as a bleaching of the ground state with contributions from both donor and acceptor, due to presence of excited states in both domains after the formation of charge carriers. The charge spectra therefore resemble that of the ground state absorption spectrum of PBDB-T, with some NFA absorption character remaining at around 725 nm. As controlled by the pump energy, excitons are formed in the NFA domains and are able to separate into charges on meeting an interface with a donor domain, allowing the free charges to travel through the donor and acceptor domains. Therefore ground state bleach features on both NFA and PBDB-T molecules

are a confirmed representation of charged species within the blend.

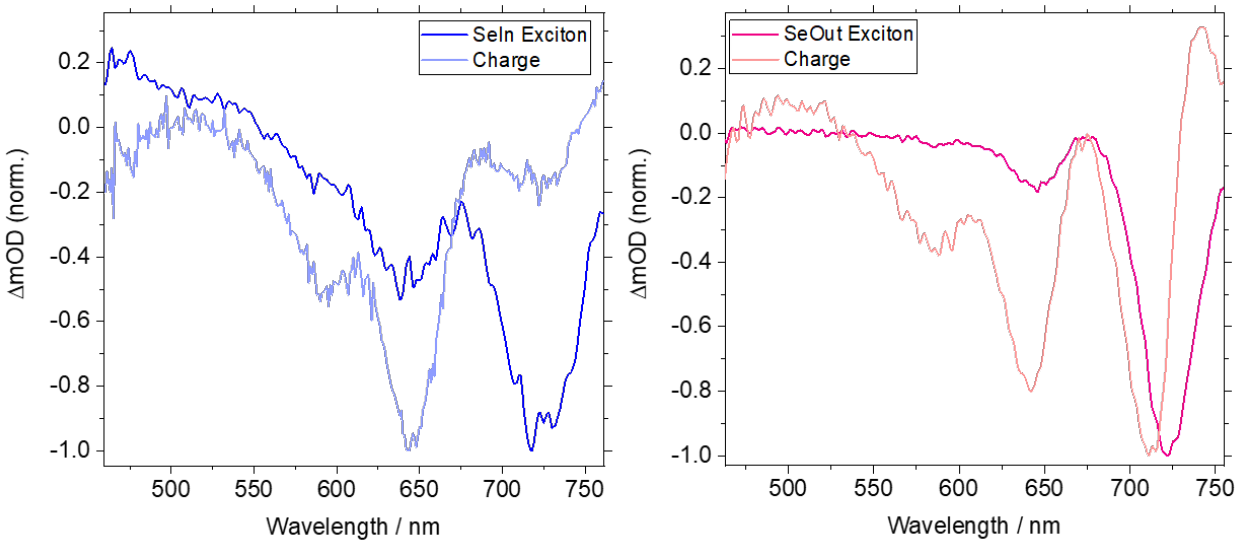


Figure 3.8: Spectra of excitonic and charge components extracted by global analysis for the PBDB-T:SeIn (left) and PBDB-T:SeOut (right) blends.

Figure 3.9 shows the kinetics associated with each of the four components represented spectrally in figure 3.8 as well as exponential fits to quantify lifetimes. The temporal evolution of each species confirms their respective assignment to excitons and charges. In both blends, the NFA excitonic components are at maximum amplitude at 0 ps and therefore are pump-induced, consistent with the use of an excitation wavelength that is resonant with the maximum absorption of the NFA ground state. The excitonic components then decay exponentially over the timescale of the experiment, further confirming the successful extraction of a purely excitonic species. The charge species of each blend is at its minimum amplitude at 0 ps and grow in amplitude until approximately 50 ps in both cases with an exponential time constant that is equal to the decay lifetime of the exciton. This observed synchronicity between exciton decay and charge growth further confirms their assignments due to the nature of the well understood mechanism of charge formation in photovoltaic blends. Furthermore, the persistence of the species at 6 ns supports the assignment as free charges because excitons and charge transfer states do not have such long lifetimes typically.

Monoexponential fits of the excitonic components reveal exciton decay lifetimes of 2.9 ± 0.3 ps and 9.7± 0.6 ps for SeIn and SeOut respectively. The agreement of these figures with the

timescales of the simultaneous onset of the charge components (3.1 ± 0.2 ps and 10.1 ± 0.8 ps for SeIn and SeOut respectively) confirms that this time constant represents the timescale of charge separation in each blend. The longer lifetime of this process in in PBDB-T:SeOut suggests that larger, more crystalline domains of donor and acceptor are formed, as pump-generated excitons are likely to be formed further from a D:A interface than in the comparatively more thoroughly mixed PBDB-T:SeIn blend. This observation was confirmed by GIWAXS measurements, which concluded that the outer Se position improved crystallinity in the blends.[62] The subsequent decay of the charge component, denoting charge recombination, occurs slowly in both blends and the signal does not decay fully on the 6 ns timescale of the experiment.

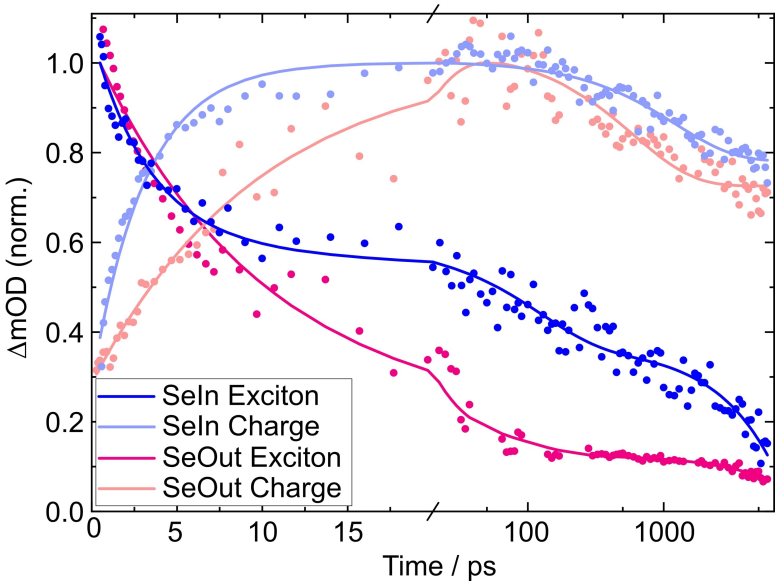


Figure 3.9: Kinetics associated with the exciton and charge components for each of the PBDB-T:SeIn and PBDB-T:SeOut blends as extracted by global analysis, with corresponding exponential fits as solid traces.

The different timescales for charge separation dynamics indicate that more ordered packing is facilitated by the outer Se position compared to the inner Se substitution, as represented schematically in figure 3.10. The increased crystallinity of NFA domains gives rise to poorer D:A miscibility, affording larger donor and acceptor domain sizes. SeOut thus exhibits three times slower charge separation than SeIn, which is a dramatic consequence of such a minor structural modification. It is suggested that the larger and more diffuse atomic orbitals on selenium compared to sulfur afford stronger non-covalent interactions with nearby atoms arising from π-orbital overlap. This means that in SeOut, where the Se atom is on the same side as the

enone oxygen on the pyrrole ring, strong intramolecular interactions between Se and O can act as a conformational lock to rigidify the planar conformation of the electron-withdrawing end groups relative to the electron-rich core. Such intramolecular non-covalent Se-O interactions have been well-studied in the literature since they were first experimentally demonstrated by x-ray crystallography in 1977, in a study that also confirmed that the Se-O interaction was stronger than the sulfur analogue.[264–266] For SeIn, where the Se substitution is on the opposite side of the molecule to the O atom, the non-covalent interactions occur between the O and the unsubstituted S atom on the outer thiophene ring. This therefore gives rise to a weaker interaction that is not sufficiently strong to hold the molecule in a planar conformation. Hence SeIn remains aromatic and planar in its BDT core but the electron-withdrawing end groups are free to rotate with respect to the core and hence the molecule can adopt alternative conformations. Meanwhile, SeOut exhibits a rigid and planar conformation spanning the full length of the molecule.

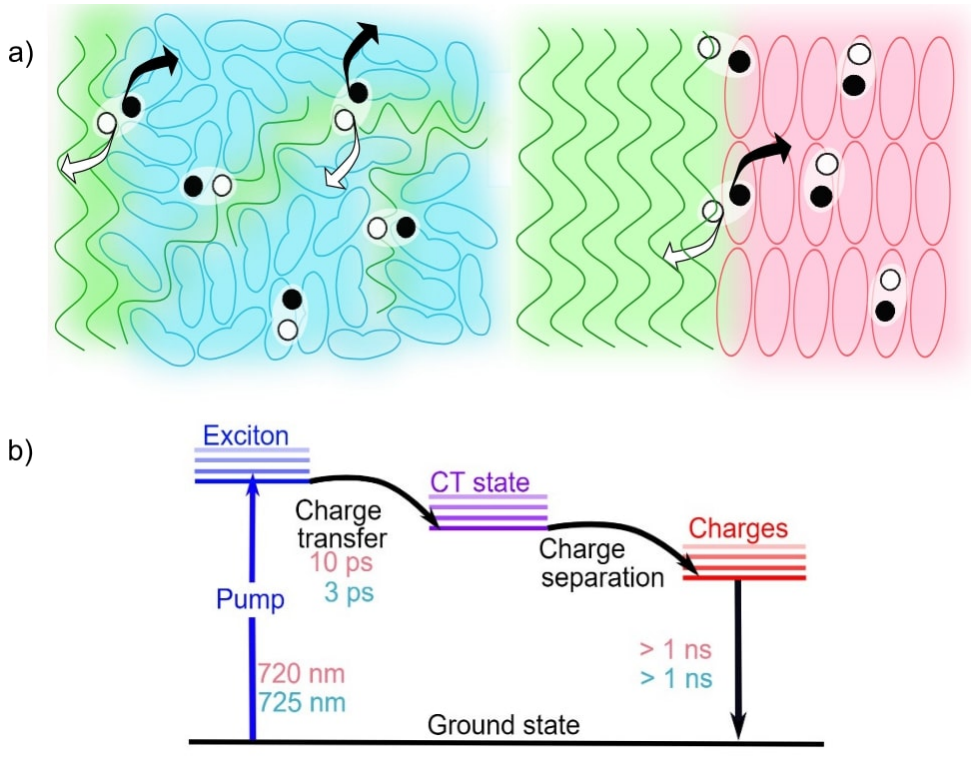


Figure 3.10: a) Cartoon representing how smaller domains (SeIn, blue, left) give rise to faster charge separation lifetimes relative to more crystalline larger domains (SeOut, red, right) when blended with PBDB-T (green polymer chains). b) Schematic diagram of dynamic processes with their characteristic timescales probed by TAS and extracted by GA for SeIn (blue) and SeOut (red) blends.

3.4 Conclusions

In this work the effect of structural modifications to well-studied OPV components, namely push-pull small molecules and NFAs, were investigated. Blends of studied materials were measured by transient absorption spectroscopy and the experimental results were deconvoluted by global analysis in order to separate distinct exciton and charge components. In the case of push-pull small molecules, a minor modification in the chemical structure gave rise to staggering morphological consequences which completely altered the molecule's behaviour in a photovoltaic blend. Similarly a minor modification was again seen to significantly affect the charge formation dynamics in a NFA study. The results highlight the complexity in structure-function relationships in semiconducting materials as the seemingly insignificant regioisomeric modifications manifest remarkable differences in optoelectronic behaviours of blends, in an intricate fashion. This work thereby asserts the importance of ultrafast dynamics in the understanding of new potential materials for organic semiconductors and brings us closer to the goal of being able to selectively design and customise molecular structures in order to achieve optoelectronic goals.

Chapter 4

Correlating photoinduced dynamics and stability in photovoltaic materials

4.1 Context and motivation

Device performances exhibited by OPVs have grown impressively since their inception, with PCEs now typically exceeding 10 %.[242] In this thriving field of research, PCEs are perpetually improving and currently boast a record of 18 %.[110] However, while research has driven the optimisation of OPV efficiency, the complementary and necessary efforts to enhance their operational stability has fallen behind. The longevity of OPV device performance under operational conditions therefore remains the limiting factor impeding their industrialisation. Commercial crystalline silicon solar cells typically come with a 25 year warranty; an estimated 10 year lifetime would be required of OPVs in order to outcompete them.[267] This presents a prohibitive obstacle for OPVs, which typically exhibit 10-50 % depletion in performance within hundreds of hours.[268] Encapsulation of devices, in which the active material is protected from the atmosphere by a glass layer, has been shown to extend lifetimes from hours to years.[269] However, glass encapsulation boosts the cost of device fabrication, while cheaper encapsulation materials such as plastic fail to offer sufficiently effective protection.[270] It is thus imperative that the intrinsic stability of OPV materials can be investigated, understood and improved in order to

make them suited to operational conditions and hence achieve their commercialisation.

Monitoring device performance over long timeframes in outdoor operational conditions, which has been reported for some OPV devices, provides the most representative experiment for determining the stability of a photovoltaic material.[271–273] However, interpretation of results in order to characterise triggers and mechanisms of degradation is complicated due to the lack of control over experimental conditions. It is therefore conventional to measure device performance under simulated real-world operation by control of experimental conditions such as light, atmosphere, electrical parameters and temperature. The commonly employed technique in the field is steady-state observation of device PCE in an artificial environment over several hours.[274–277]

However, degradation typically arises due to a combination of influencing factors including hydration of materials, oxidation and photoinduced mechanisms.[278] The relative prominence and intricate interplay between each of these processes cause barriers to the assignment sources of degradation in different materials when only the overall efficiency is measured over several hours.[279] Furthermore, time-resolved spectroscopic studies have quantified degradation timescales ranging from picoseconds to microseconds, while devices employing photoprotective materials have exhibited photoprotection mechanisms on timescales no longer than microseconds.[215,280–283] The application of ultrafast spectroscopy is therefore a prudent approach for disentangling the processes that cause degradation and photoprotection in solar cell materials in order to observe their action in real-time. In this chapter, transient absorption spectroscopy is applied to two photovoltaic systems for the direction investigation of their charge dynamics in order to elucidate the mechanisms that influence their operational stability.

4.1.1 Photoprotection in fullerene-based solar cells

The stability of organic acceptor materials has consistently been at the forefront of discussion around OPVs.[107] Despite their short operational lifetimes, fullerenes were almost exclusively employed as the electron-accepting component in OPVs until the mid-2010s, due to other attractive optoelectronic properties.[284] Breakthrough results by fullerene-containing organic

devices sparked a surge of interest in the OPV field that fed the ever-growing efforts to drive device performances higher.[285] While efficiency was gradually improved via investigation into novel donor materials and device architectures, the persistent poor stability of fullerenes was neglected. Their intrinsic lack of stability under the required operating conditions of a solar cell is now understood to be a major issue that requires confronting in order to advance OPVs such that they could ever be industrially viable.

The mechanistic explanations for short lifetimes of fullerene-based devices have been thoroughly investigated. Even in an inert atmosphere, incident light alone can activate the dimerisation and oligomerisation of fullerenes via photoinduced 2+2 cycloaddition.[286,287] When fullerenes are blended with a donor component, these reactions perturb the morphology of the blend owing to the poorer miscibility of fullerene oligomers relative to their monomers.[288] Consequently, a severe loss of short-circuit current and thus decreased device performance can occur in the tens of hours following initial illumination.[289] Furthermore, exposure to atmospheric conditions can trigger photooxidation reactions such as epoxide and carbonyl substitutions on the fullerene structure.[290–292] These oxidations decrease the LUMO of the fullerene and thus provide electron traps in acceptor domains, which significantly reduce the open-circuit voltage of the device.[293] This has been shown to have a radical effect on device efficiency, with one study demonstrating a 90 % depletion of initial performance occurring from oxidation on only 3.6 % of the total fullerene population.[294] The same study showed that oxidation on less than 1 % of the present fullerene molecules was sufficient to lose 65 % of the initial device performance. Collectively these mechanisms mean that the operational lifetimes of fullerene-containing devices may be diminished to the range of minutes to hours when illuminated under ambient conditions.[295–297]

In light of the poor stability of fullerenes, the OPV field is increasingly turning to NFAs which do not exhibit these detrimental reactions to operational conditions. Additional attributes such as greater structural tuneability and potential for lower production costs increasingly ramped their popularity, which led to the first NFA system surpassing the efficiency of fullerene blends in 2017.[109] A device comprising Y6 blended with D18, a prominent NFA and donor copolymer respectively, currently holds the record for OPV performance at 18 %.[110] However, although this shift resolves the complications pertaining to the poor stability of fullerenes, it exposes certain

additional problems relating to the manufacturing and implementation of OPV devices.[268] Hence the resolution of fullerene degradation in photovoltaic blends remains a pertinent focus of research.

While the intrinsic stability of fullerenes and small molecule acceptors continues to receive attention, the stability of small molecule donor components remains less well investigated.[298] One particular donor molecule of interest is 2,2'-[(3,3"',3"",4'-tetraoctyl[2,2':5',2":5",2"':5"',2""-quinquethiophene]-5,5""-diyl)bis[(Z)-methylidyne(3-ethyl-4-oxo-5,2-thiazolidinediylidene)]]bispropanedinitrile (DRCN5T), which was first synthesised in 2015[299] and has been blended with both fullerenes and NFAs to afford notable device performances.[300,301] Studies have shown that the morphological consequences of visible light exposure can cause performance losses in DRCN5T-containing devices but its stability under atmospheric conditions had not been investigated prior to this work.[302,303]

In our study, DRCN5T:$PC_{70}BM$ demonstrated impressive stability when exposed to light and oxygen due to the donor molecule's intrinsic stability under operational conditions.[298] A device comprising DRCN5T:$PC_{70}BM$ and a range of polymer:$PC_{70}BM$ devices were exposed to 1 Sun illumination and O_2, while their efficiencies were monitored over a 17 hour period. The performance of the polymer-containing blends depleted dramatically however the DRCN5T-containing blend preserved 93 % of its initial efficiency at the end of the degradation period. In the work described in this chapter, TA spectroscopy was employed to investigate the photophysical explanation for this uniquely impressive stability. The study revealed that ultrafast energy transfer from $PC_{70}BM$ to DRCN5T facilitated quenching of the unfavourable excitation energy on the fullerene which would otherwise activate detrimental degradation mechanisms. Hence, the ability of DRCN5T to accept the energy from $PC_{70}BM$ and to subsequently remain stable was shown to provide a pathway for photoprotection of the fullerene acceptor and thus yield superior stability in a fullerene-containing OPV blend.

4.1.2 The relationship between stability and charge trapping in $AgBiS_2$ quantum dot solar cells

Quantum dot solar cells (QDSCs) are increasingly drawing attention in the photovoltaic field due to desirable optoelectronic properties,[304] the ability to tune the material's bandgap by adjusting the nanocrystal size,[305] and enhanced stability compared to most organic components.[306] Of this class of materials, lead-chalcogenide QDs have proven to be the most prominent,[307,308] due to their solution-processability and high performance,[217] with PCEs above 12 % attained in QDSCs[309] and as high as 16.6 % for lead perovskite QDSCs.[310]

However, such devices are preventatively unstable under the typical operational conditions of a solar cell,[311] while the toxicity of lead prohibits their use in commercial applications.[312] Therefore, the expansion of the QDSC field towards lead-free materials is a highly relevant point of study. One promising alternative receiving attention is bismuth due to its improved stability and low toxicity compared to lead.[311] Several bismuth-containing systems have been reported, including silver bismuth halide perovskites demonstrating the most impressive stability under ambient conditions.[313] Further lead-free materials that have been investigated include silver bismuth sulfide ($AgBiS_2$).[314,315] First employed as a QDSC active material in 2016, it was shown to afford PCEs above 6 % when combined with zinc oxide (ZnO), a commonly employed electron-transporting layer (ETL), and an organic polymer hole-transporting layer (HTL) composed of poly[[4,8-bis9(2-ethylhexyl)oxy]benzo[1,2-b:4,5-b']dithiophene-2,6-diyl][3-fluoro-2-[(2-ethylhexyl)carbonyl]thieno[3,4-b]thiophenediyl]] (PTB7).[217] This was reported to be the first inorganic solar cell material that satisfies all the criteria of low-temperature solution processability, non-toxicity, abundance and adequate device efficiency.

In the typical case for lead-sulfide (PbS) QDSCs, the active layer sits between a ZnO ETL and a HTL comprising PbS QDs coated with 1,2-ethanedithiol ligands (PbS-EDT). While these devices can exhibit impressive operational stability,[316] recent studies show that facile oxidation of the PbS-EDT HTL is responsible for degradation of the HTL and thus a diminishing device efficiency.[317,318] Approaches to overcome this drawback have involved exploring alternative HTLs which suppress the degradation without compromising device performance. One

successful strategy has been to use an organic polymer HTL such as poly(3-hexylthiophene-2,5-diyl) (P3HT), poly-[bis-(4-phenyl)-(2,4,6-trimethylphenyl)-amine (PTAA), or PTB7 which offer improved intrinsic stability relative to QDs, in conjunction with an additional molybdenum trioxide (MoO_3) layer to enhance their hole-transporting ability and hence compensate for their lesser efficiency relative to PbS-EDT.[319–321] The best performing result of this family of devices employed a PBDB-T/MoO_3 HTL, achieving a PCE of 11.2 %.[322] However, the MoO_3 layer has been found to detriment the stability of the device and hence offset the benefits of using the organic HTL over PbS-EDT.[323] The pursuit of alternative MoO_3-free HTLs is therefore imperative in order to realise viability of QDSCs by boosting their stability under operational conditions.

In this study, $AgBiS_2$ QDSCs with different combinations of HTLs and ETLs were trialled as an investigation into the relationship between device architecture and the stability of the resultant devices. Thus far, the operational stability of $AgBiS_2$ QDSCs under ambient conditions and light has not been investigated, though they have been reported to be stable under oxygen in the dark[324] and on a single exposure to water,[313] and neat $AgBiS_2$ is understood to remain stable for several months.[217] Both PTB7/MoO_3 and p-doped PTAA[325] (PTAA:$C_{60}F_{48}$) were separately employed as HTLs. This doping of PTAA has been previously shown to give rise to efficient blocking of electrons and consequently improve the PCE from 9.1 % to 10.4 % relative to PTAA/MoO_3 for a PbS QDSC.[326] The two HTLs were both combined with different morphologies of ZnO ETLs, either in nanoparticle morphology (ZnO_{np}) or deposited from sol-gel (ZnO_{sg}), affording four different device configurations in total, shown in figure 4.1.

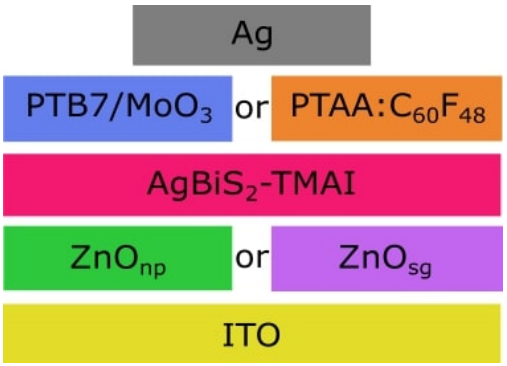


Figure 4.1: Different ETL and HTL components affording the four different devices studied.

The devices' PCEs were measured over time under degradation by oxygen and light exposure, revealing that the ZnO_{sg}/$AgBiS_2$-TMAI/PTAA:$C_{60}F_{48}$ device was the only one with any appreciable stability while the other three devices suffered rapid and dramatic performance loss.[216] Prior studies have shown that PTB7 degrades under O_2 and light resulting in a depletion of chromophores, and hence a decrease in light absorption, as well as a loss of conjugation to the detriment of its transport properties.[327] Scanning electron microscopy measurements revealed considerable corrosion on the electrodes of PTB7-containing devices, due to formation of Ag_2S crystals. This corrosion could also be seen, albeit to a lesser extent, on the ZnO_{np}/$AgBiS_2$-TMAI/PTAA:$C_{60}F_{48}$ device while the sol-gel counterpart appeared unaffected. Neat ZnO is understood to be very stable but it can trigger degradation in the active layers by interfacial effects.[328] Photoelectron spectroscopy studies comparing pristine and oxygen-degraded devices indicated oxidation of $AgBiS_2$ to Bi_2O_3 and iodine by the photoinduced reaction of TMAI ligands and $AgBiS_2$ with atmospheric oxygen:

$$4I^- + O_2 + 2H_2O \rightarrow 4OH^- + 2I_2 \tag{4.1}$$

where the reactant iodide is gleaned from TMAI ligands. The rougher ZnO_{np} relative to ZnO_{sg} ETLs affords greater surface area for physisorption of water which results in an acceleration of reaction 4.1. The iodine produced reacts with the silver electrodes and give rise to their corrosion:

$$2Ag_{(s)} + I_{2(g)} \rightarrow 2AgI \tag{4.2}$$

while atmospheric oxygen can also cause the photoinduced oxidation of the active layer:

$$AgBiS_2 \rightarrow Bi_2O_3 + Ag_2S \tag{4.3}$$

Together these reactions are understood to contribute to a loss of charge extracting ability, but the specific mechanisms by which they detriment the photoinduced dynamics had not yet been investigated. Time-resolved spectroscopy was therefore employed herein to investigate and compare the fates of charge carriers in pristine and degraded devices. TA spectroscopy on neat films of $AgBiS_2$ at increasing extents of degradation first revealed a spectral signature

representing degradation of the material. By subsequently applying TA to the four different QDSC devices and quantifying this spectral representation of degradation for each device configuration, the results provide a hierarchy of stability under operational conditions for the four studied devices. This conclusion was congruent with device performance data thus confirming the validity of the approach and the model.

4.2 Experimental details

4.2.1 Sample preparation

All samples studied were prepared according to the descriptions in section 2.1.

4.2.2 Steady-state absorption characterisation

Steady-state absorption spectra were measured for all samples using the instrument outlined in section 2.2.1.

4.2.3 Transient absorption spectroscopy

Transient absorption (TA) spectra were obtained using the experimental setup outlined in section 2.3.2. For the results presented in section 3.3.1, the TA spectra were measured by Dr Andreas Weu (University of Heidelberg).

4.3 Results and discussion

4.3.1 Photoprotection in fullerene-based solar cells

In TA measurements, a blended film of the small-molecule donor DRCN5T and the fullerene $PC_{70}BM$ was excited with a 700 nm pump resonant with the absorption maximum of the donor. The blend was studied incrementally over a 22 hour period of 20 % O_2 exposure and simultaneous continuous illumination conditions of 1 Sun. The presented results show 11 distinct samples at varying degrees of degradation in order to investigate the effects of gradual degradation on the charge formation dynamics. The spectra were analysed with global analysis (GA) in order to extract specific components for excitons and charges and thus observe their temporal evolution.

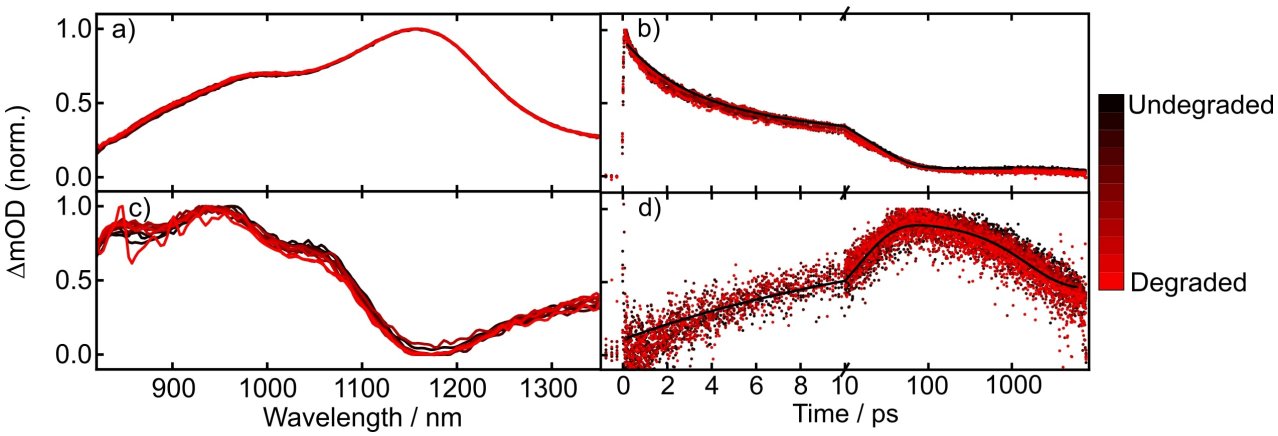


Figure 4.2: Normalised GA-derived spectra (left) and associated kinetics (right) for DRCN5T excitons (top) and charges (bottom) present in the DRCN5T:$PC_{70}BM$ blend extracted from TA spectra collected following 700 nm excitation (150 nJ) for varying extents of degradation. Only one exponential fit is included in each of the kinetic traces for figure clarity, taken from analysis of the pristine blend data and shown as black solid lines.

The spectra collected for the near-infrared probing region and their associated kinetics resulting from GA are shown in figure 4.2. The GA was carried out using the donor exciton spectrum - captured from the neat DRCN5T TA spectrum at very early delay times - as a reference with the second component undergoing free evolution. It can be safely assumed that the DRCN5T exciton is present as it is selectively excited by control of the excitation wavelength. Trials of this method with a greater number of components confirmed that there are only two photophysical species present in the blend following direct excitation of the donor component, represented

spectrally in the left plots of figure 4.2.

The physical character of one species is known, as the DRCN5T exciton was fed into the algorithm, and the second component can be assigned with confidence to free charges based on its temporal evolution. The kinetics for the two components are shown in the right panels of figure 4.2. Monoexponential fits to the exciton decay kinetics reveal that this process occurs with approximately a 3 ps lifetime for all blends. The second species emerges on an approximately 10 ps lifetime and decays on a 3 ns timescale. Charges are typically the only species that persist on the nanosecond timescale in OPV blends due to the short lifetimes of excitons and charge transfer states. The second species is therefore assigned to charges formed in the blend, with the initial picosecond process characterising the charge separation process. This assignment is corroborated by the energetic justification for charge transfer in the blend as the LUMO level for DRCN5T and $PC_{70}BM$ are -3.4 eV and -3.9 eV respectively.

As implied by the overlaid traces in figure 4.2a and 4.2c, the degradation was not observed to affect the spectral shape of the components, revealing that the physical nature of the excitations in question are unaffected by the degradation. The dynamics of charge transfer and decay also appear unchanged by the increasing degradation. Exponential fits allowed determination of time constants for these processes at each incremental stage in the degradation process. In order to fully verify a lack of correlation between degradation and charge dynamics, the time constants were plotted as a function of degradation in figure 4.3. As these plots do not reveal a trend, it can thus be deduced that degradation does not influence the timescales of ultrafast processes induced by 700 nm excitation in the blend.

The 700 nm pump TA study confirms that degradation does not affect the photoinduced dynamics in DRCN5T:$PC_{70}BM$, which is consistent with implications made by the device performance study discussed in section 4.1.1.[298] However, this does not offer any photophysical explanation for the blend's intrinsic stability. Therefore, in order to directly interrogate what is occurring within the fullerene domains that inhibits degradation of $PC_{70}BM$, TA experiments were also carried out with a 250 nm pump. This wavelength is understood to directly effect selective generation of $PC_{70}BM$ excitons as it corresponds to strong absorption by $PC_{70}BM$ and a relatively

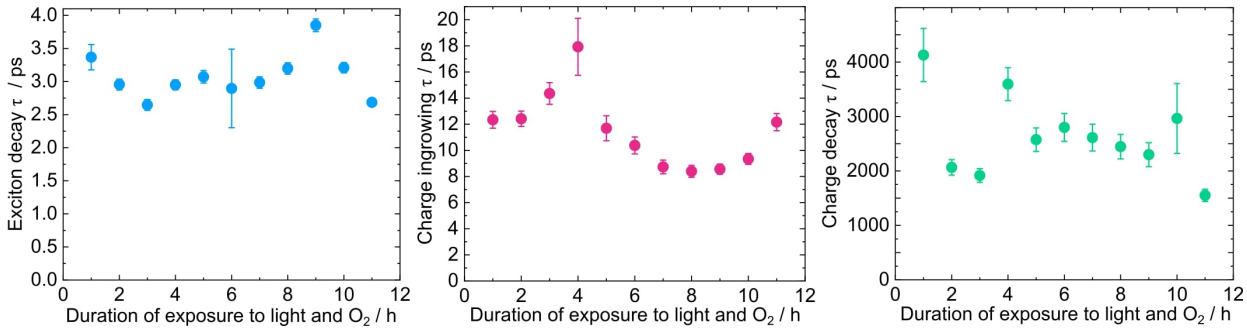


Figure 4.3: Time constants of the photophysical processes occurring in the studied blend following 700 nm excitation, determined by monoexponential fitting of the kinetic traces in figure 4.2, plotted as a function of degradation.

insignificant amplitude of absorption by DRCN5T. However, the shape of the raw spectrum (shown in figure 4.4) before deconvolution by GA appears to contain a strong contribution from DRCN5T by bearing resemblance to the neat DRCN5T spectrum in showing a peak at 1200 nm.

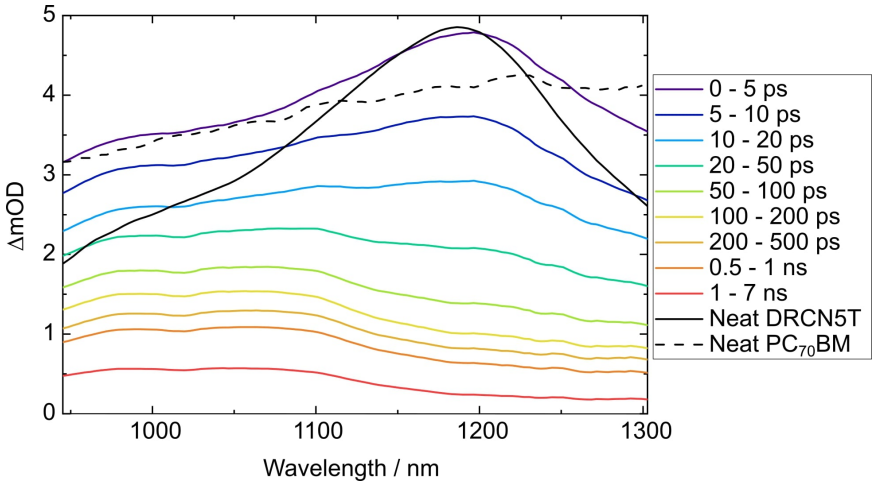


Figure 4.4: TA spectrum of the 250 nm pump experiment (150 nJ) with $PC_{70}BM$ and DRCN5T neat spectra at early times superimposed for clarity.

Contrary to the presence of just one exciton and one charge component in the 700 nm pump data, GA confirmed the presence of three spectral components in the 250 nm experiment. As the spectrum in figure 4.4 suggests a dominant contribution from the DRCN5T exciton spectrum, GA was executed by entering the neat donor exciton spectrum as a reference and allowing two further components to be freely optimised using the algorithm. The spectra of the resultant three components and their associated kinetics are plotted in figure 4.5.

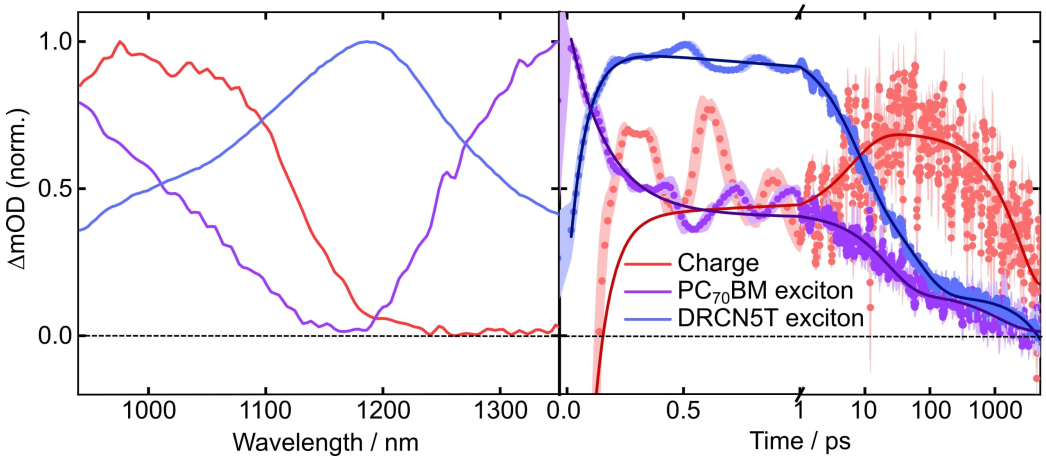


Figure 4.5: Normalised GA-derived spectra (left) and associated kinetics (right) for the TA spectrum measured using a 250 nm pump pulse to selectively excite the fullerene. Kinetics are plotted as moving averages with associated errors shown.

The three components are assigned to DRCN5T excitons, $PC_{70}BM$ excitons and free charges. The donor exciton component can be assigned as it was used as a reference in GA, hence we can be confident of its physical origin. The $PC_{70}BM$ exciton differs slightly from the experimentally measured spectrum (see appendix A.1) in the lower-wavelength edge of the probing region due to some difficulty deconvoluting the $PC_{70}BM$ and charge traces with global analysis. This is also a likely cause for the mixed kinetics for these two traces between 0.5 and 1 ps. However, the $PC_{70}BM$ component can be assigned with confidence due to its selective excitation with the 250 nm pump and because the kinetics show that this component has a maximum amplitude at time zero, which is expected for a species that is generated directly by the pump. The charge spectrum can be assigned due to its temporal evolution, as it rises gradually until 10 ps and then decays slowly on a nanosecond timescale that is characteristic of free charges in OPVs.

The 250 nm photoexcited dynamics reveal that we do not observe direct charge separation from the pump-excited excitons (on $PC_{70}BM$ in this case), as was depicted by synchronous exciton decay and charge rise dynamics in the 700 nm measurement. Instead, the DRCN5T exciton appears to act as an intermediate state to the charge separation process. There is a clear ultrafast decay of the acceptor exciton which occurs with concurrent ultrafast emergence of the donor exciton component. Later, the DRCN5T exciton begins to decay, and the concomitant onset of the charge growth component indicates that charge separation has begun.

These kinetics illustrate that excitation of $PC_{70}BM$ is immediately followed by ultrafast energy transfer to DRCN5T. This process depletes the population of $PC_{70}BM$ excitons and generates donor excitons, from which the subsequent charge separation ensues. In conjunction with this device's observed stability, this process suggests that the ability for this energy transfer to take place on an ultrafast timescale - and for DRCN5T to remain stable after receiving the excitation energy - facilitates a photoprotective mechanism. The transfer pathway allows quenching of excitation on the fullerene which would otherwise provide activation for harmful degradation reactions. This rare characteristic of an OPV blend suppresses degradation and establishes a blend that exhibits intrinsic stability under operating conditions. Similar results have been observed in analogous systems, where Yan et al. found that the rate of fullerene dimerisation was decreased by piperazine doping in an OPV blend, as it provided a charge transfer pathway by which to quench fullerene excitons.[329] We therefore conclude that this effect could be harnessed for design of future OPV systems, in order to attain coincident high stability and performance without needing to compromise one in order to achieve the other.

4.3.2 The relationship between stability and charge trapping in $AgBiS_2$ quantum dot solar cells

TA measurements were first carried out by excitation of neat $AgBiS_2$ films with a 700 nm pump in order to excite just above the material's band gap. Figures 4.6a-e shows the TA spectra for films at increasing extents of degradation under O_2 and light, from pristine (0 hours) to fully degraded (27.5 hours). All spectra contain a single broad photoinduced absorption (PIA) that spans the probing region and contains two kinetic components. A $\sim$100 ps component dominates the decay, which we associate with mobile carriers and their bimolecular recombination, confirmed by steady-state absorption spectroscopy (see appendix B.1) and intensity-dependent TA measurements shown in figure 4.7a. Exciton absorption gives a distinguishable sharp peak at the low-energy edge of the absorption spectrum and therefore a material with excitonic character shows an abrupt onset of absorption as opposed to a gradual slope.[330] Appendix B.1 shows the absorption spectrum for the $AgBiS_2$ films where a sharp absorption edge is not

observed, confirming that the TA signals can be attributed to carriers as opposed to excitons. The intensity-dependence of the TA PIA, shown in figure 4.7a, reveals the carrier population-dependence of the dynamics, confirming that the decay of this signal arises due to bimolecular recombination. A long-lived component in the TA spectra in figure 4.6 persists beyond the 6 ns timescale of the measurement and does not show a pronounced dependence on excitation flux which we therefore attribute to immobile trapped carriers.

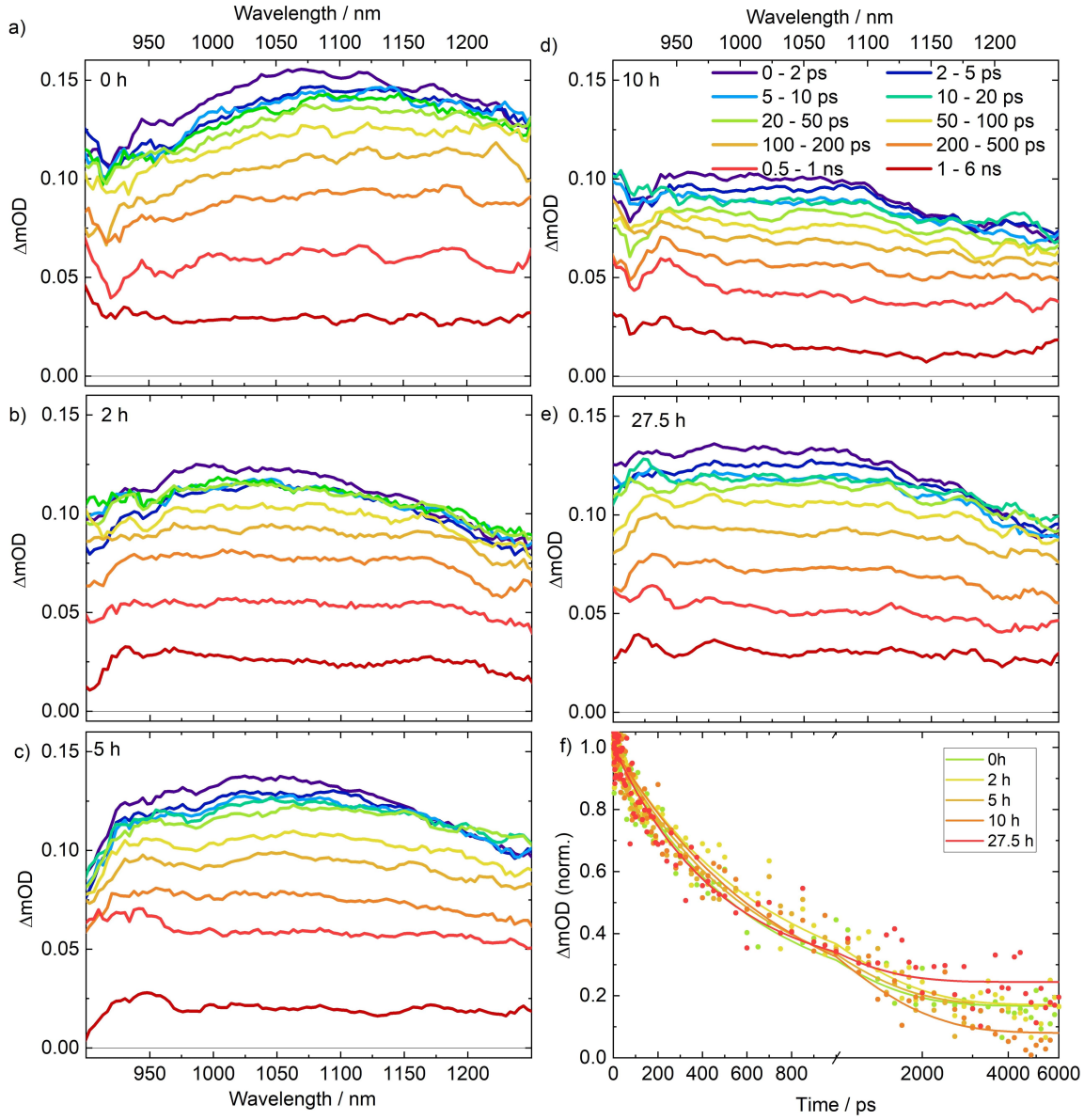


Figure 4.6: a-e): TA spectra for neat $AgBiS_2$ films at increasing extents of degradation, following excitation with a 700 nm pump (50 nJ). f): Normalised kinetics of PIA for each film.

Figure 4.6f shows the evolution of the PIA as a function of time for all films. There is no clear correlation between the kinetics of the decay and the extent of degradation, consistent with the

impressive stability of $AgBiS_2$ material when not incorporated in a device. However, there is a greater amplitude of trapped carriers (present after 1 ns) in the fully degraded film. The decay appears to plateau at 3 ns for this trace but continues until 4-5 ns for the lesser degraded films, which confirms our assignment of long-lived states to trapped charges. Furthermore, the PIA signal is seen to blueshift with increasing degradation relative to the 0 h spectrum (progressing chronologically from figure 4.6a to 4.6e), with the maximum occurring at around 1100 nm and 1000 nm for 0 h and 27.5 h respectively. This effect is particularly pronounced at early time delays where both mobile and trapped carriers contribute to the signal. At later times, where only trapped charges are present, the spectra look similar.

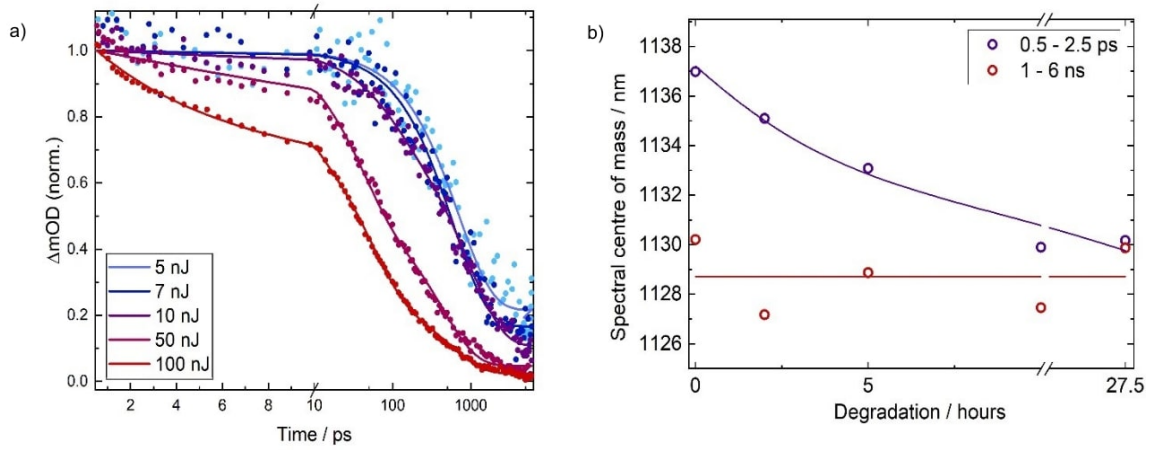


Figure 4.7: a): Fluence dependence kinetics and exponential fits of PIA in pristine film. b): Spectral centre of mass as a function of degradation for early time delays vs late time delays. Fits are included as a guide to the eye to demonstrate the centre of mass trajectory.

In order to quantitatively verify the observed relative peak position shift, the spectral position was calculated as the spectral centre of mass (SCOM) for both early delay times and late delay times. The spectra were therefore first averaged over the temporal ranges 0.5-2.5 ps and 1-6 ns to afford early time and late time spectra. Then for each of these spectra the SCOM was quantified across the probing region, by calculation of the weighted average wavelength in that spectrum, given by the sum of each wavelength n weighted by its amplitude divided by the sum of amplitudes:

$$COM = \frac{\Sigma\lambda(n)\Delta OD(n)}{\Sigma\Delta OD(n)} \tag{4.4}$$

Figure 4.7b shows the SCOM for both the early and late delay time spectra for each of the neat

$AgBiS_2$ films from pristine to fully degraded. The early delay time spectra show a significant blueshift from pristine to degraded, while the SCOM at late times show a consistent PIA position. It is expected that only trapped charges contribute to the signal on the 1-6 ns timescale across all films regardless of their degradation. On the 0.5-2.5 ps timescale, dynamic processes occur involving both free and trapped charges and therefore we expect to observe some variation as a function of degradation. As the SCOM increasingly blueshifts with increasing degradation, we suggest that the spectral position of the PIA represents the relative population of trapped charges in the material.

In order to investigate the relationship between charge trapping and the varying stabilities exhibited by different device configurations, TA measurements were carried out on $AgBiS_2$-containing optoelectronic devices described in section 4.1.2. These experiments were performed by focusing the pump and probe beams onto a spot between electrodes. Figure 4.8 shows TA spectra for $AgBiS_2$ devices with the four different combinations of hole and electron transport layers for pristine (left) and degraded (right). The specific peak positions of the spectra vary across devices due to interference effects caused by contributions from different charge extraction layers. However, the spectra are broadly consistent across the range of device configurations, showing PIA features at the NIR edge of the probing window and a negative signal at wavelengths approaching the visible region. All spectra also contain a long-lived component that remains after the 6 ns timescale of the measurement which generally reflects the broad and flat spectrum of trapped charges present at long time delays in the neat $AgBiS_2$ film spectrum.

In the neat $AgBiS_2$ spectra, a blueshift is observed on degradation; this shift was investigated in the device spectra in figure 4.8. Rather than comparing a temporally-averaged centre of mass for each spectrum as is presented in figure 4.7b, the SCOM of the PIA region for each separate spectrum was calculated as a function of delay time. As the spectral position of the PIA was interpreted to represent the relative population of trapped charges in the material, this time-resolved calculation of PIA position reveals dynamic information regarding the evolution of charge trapping. For each device, the SCOM across the PIA region was calculated at each timepoint and is plotted as a function of time in figure 4.9. All devices can be observed to blueshift until 500 ps with a trace that was fitted to a monoexponential function.

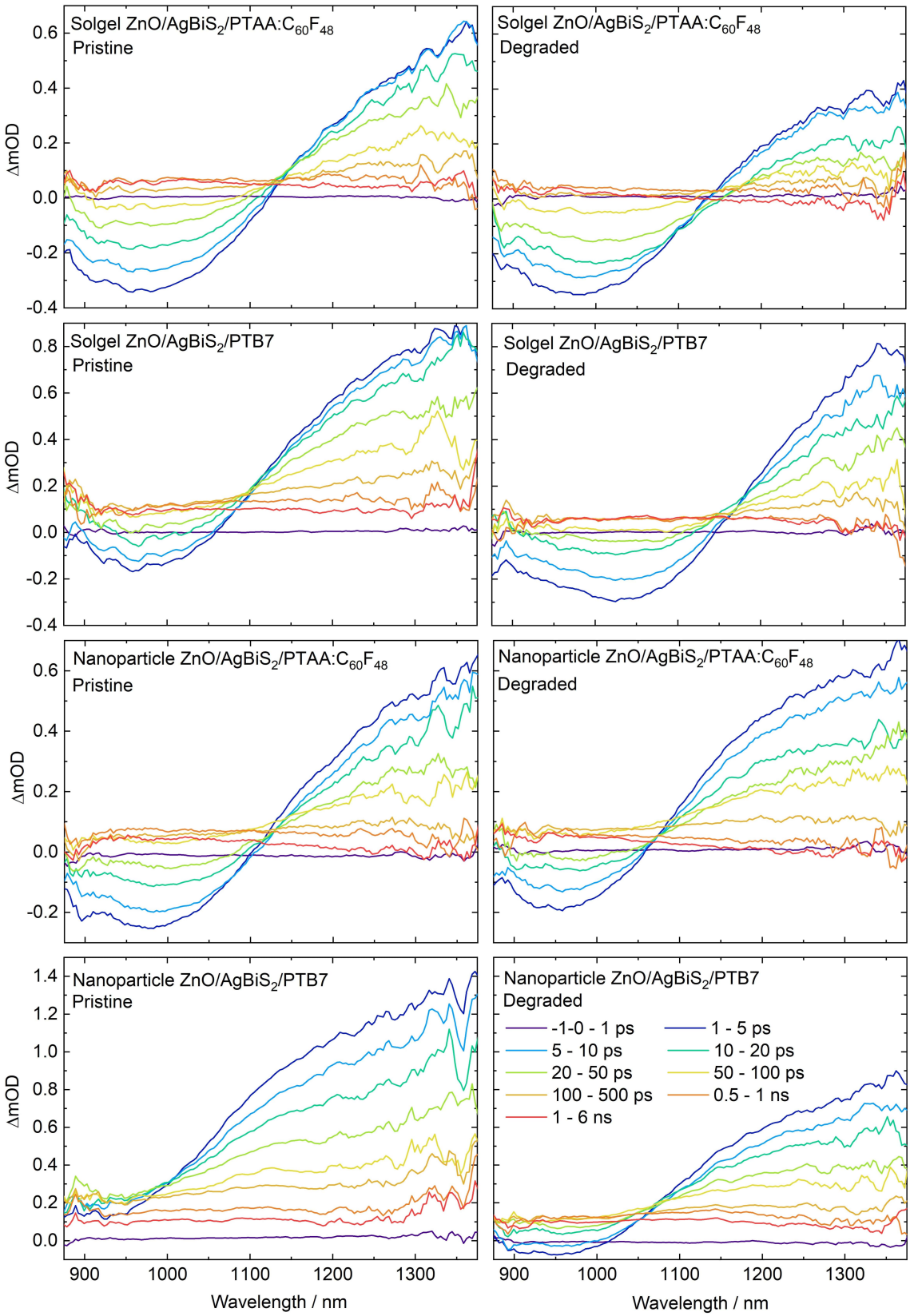


Figure 4.8: TA spectra for $AgBiS_2$ devices (pumped at 700 nm) with different hole and electron transport layers, both pristine (left) and following 8 hours of degradation under light and O_2 (right).

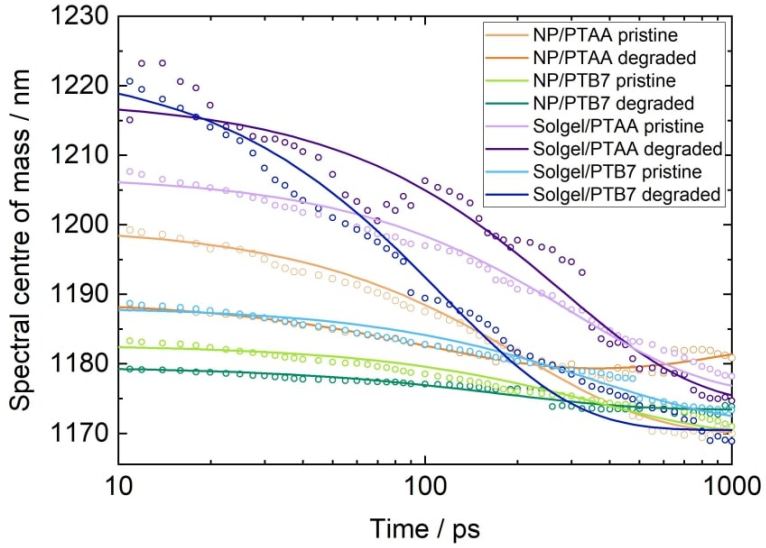


Figure 4.9: Spectral centre of mass across the PIA region for each device as a function of time, as well as solid lines showing monoexponential fits used to quantify the blueshift.

In order to quantitatively describe the impact of degradation for each device configuration, the time constants for this process were extracted from the monoexponential fit. As the blueshift is attributed to formation of trapped charges within the device, a faster lifetime of this process illustrates faster charge trapping. Charge traps are formed as a consequence of degradation and hence each degraded device exhibits a faster timescale of charge trapping relative to the corresponding pristine device. By calculating the percentage decrease of this lifetime for each degraded device relative to the corresponding pristine lifetime, we arrive at a metric that quantifies the effect of degradation on each device. Hence from this analysis it is possible to quantitatively compare each device's susceptibility to degradation and, more specifically, the formation of active charge traps.

Device ETL/HTL	Pristine lifetime / ps	Degraded lifetime / ps	Decrease / %
ZnO_{sg}/PTAA:$C_{60}F_{48}$	306	281	8.2
ZnO_{sg}/PTB7	356	109	69.4
ZnO_{np}/PTAA:$C_{60}F_{48}$	210	114	45.7
ZnO_{np}/PTB7	366	178	51.4

Table 4.1: Time constants for the PIA centres of mass shift, and the percentage decrease of the time constant of the degraded device relative to the pristine device

Three of the four devices show a dramatically faster timescale of charge trapping as a result of degradation with approximately 45 – 70 % faster charge trapping in the degraded devices.

It is important to note that in attempting to model charge trapping as a single photophysical process in each device, monoexponential fits were used in each case. We acknowledge that the traces for the ZnO_{sg}/$AgBiS_2$/PTB7 devices do not fit perfectly and therefore the blueshift lifetime for the pristine device is slightly overestimated while in the degraded case it is slightly underestimated. The charge trapping timescale decrease may therefore not be as high as 69 % if fit to biexponential functions but in order to maintain a consistent analysis across the range of devices, this model was preferred. Nonetheless, the qualitative trend can be assumed to remain accurate as the ZnO_{sg}/$AgBiS_2$/PTB7 device provided a drastically larger decrease than all other devices on a scale beyond the effect of the fit inaccuracies.

The device that is least affected by the degradation is the ZnO_{sg}/$AgBiS_2$/PTAA:$C_{60}F_{48}$ device with only an 8 % faster timescale of charge trapping in the degraded device relative to the pristine device, which is drastically lower than all of the other three material configurations. This conclusion is in excellent agreement with the devices' photovoltaic performance data which showed that the combination of sol-gel ZnO ETL and PTAA:$C_{60}F_{48}$ HTL offered impressive stability under O_2 and illumination while the performance of the other three devices was seen to decline dramatically over the timescale of the measurement. This suggests that degradation products act as trapping sites that significantly impact the ability of the device to generate photocurrent, thus justifying the loss in photovoltaic performance for the poor stability devices. The TA study has therefore rationalised the varying stabilities observed in the device performance data in terms of photoinduced dynamics.

4.4 Conclusions

In this chapter, the stability of material candidates for photovoltaic devices were explored by time-resolved spectroscopy in order to examine the events following photoexcitation. In both studies presented here, previously measured device performance data had revealed interesting findings which were investigated spectroscopically in order to rationalise these observations in terms of photoinduced dynamics. In a blend of a fullerene acceptor with a small molecule donor,

TA spectroscopy unveiled an ultrafast photoprotective mechanism of energy transfer which afforded superior stability of the blend by means of quenching fullerene excitons. This result can be used to guide future design of OPV materials by purposefully unlocking this mechanism to ensure longevity of fullerene-containing devices. In a series of QDSC devices, TA data concluded that the device that exhibited the best operational stability also demonstrated superior resistance to the formation of charge traps after degradation. This study resolves questions surrounding the optimum ETL and HTL configuration in $AgBiS_2$ QDSCs and the results can be used to inform design of such devices, as well as to lead studies which attempt to extrapolate these findings to QDSCs comprising different active materials. Overall, this chapter summarises how time-resolved absorption data can be used to investigate the photoexcited processes which often give rise to degradation in photovoltaic devices. These studies therefore demonstrate the benefits of the ultrafast spectroscopic approach for interrogation of degradation mechanisms over the conventional PCE methods typically measured over long timescales. Degradation is one of the pivotal linchpins requiring control in order to revolutionise photovoltaic materials and this work thereby makes important advances towards their optimisation.

Chapter 5

Time-resolved spectroscopic studies of photosynthesis in cyanobacteria

5.1 Context and motivation

Photosynthesis fundamentally drives and maintains all life on Earth.[331] Its photoinduced fixation of CO_2 yields organic molecules as storage units for solar energy, in the currency of chemical energy, and its simultaneous production of molecular oxygen provides the atmosphere for respirational organisms. Photosynthesis is thus the principal mechanism connecting life on our planet with the 120,000 TW of energy offered by the Sun.[4] There have therefore been growing efforts to exploit photosynthetic microorganisms for the objective of renewable energy generation, owing to their abundance and near-unity efficiencies, their capacity for self-repair as well as direct and intrinsic energy storage mechanisms.[129,144]

5.1.1 Comparison of the photosynthetic processes within biophotovoltaic devices *in vitro* and cyanobacteria cells *in vivo*

The field of biophotovoltaics (BPVs) denotes the use of a whole microorganism for photocurrent generation, taking advantage of its natural photosynthesis for the direct production of electrical

energy.[148] By definition, BPVs specifically consume only sunlight and water in this process.[159] Incident photons are harnessed to induce water splitting at a biophotoanode comprising the microorganism. Electrons are thus harvested from water molecules such that on connection of the biophotoanode to an electrical circuit (i.e., in an electrochemical cell), electrical current is generated. Due to the effectively infinite supply of water and sunlight (relative to the scale of human energy demands), as well as the robustness of microorganisms, the past twenty years has seen an ever-growing interest in the field of BPVs.[149–151]

Of the diverse range of microorganisms employed in BPV devices, cyanobacteria are the most commonly employed and are considered to be the most promising component in photobiotechnology.[332] At the time of writing this thesis, the highest-performing BPV device employed the *Synechococcus* species to afford a power density of 610 mW m^{-2}.[157] Further studies employing the same species as well as several others over the past decade have reinforced the growing popularity of the field.[137,152,174,333–337] The most prominent species of cyanobacteria amongst BPVs is *Synechocystis* sp. PCC 6803 (hereafter Synechocystis) due to its more complete genome characterisation compared to analogous species providing pathways for genetic manipulation, its facile formation of biofilms on conductive electrode surfaces such as ITO, as well as its extensive application in prior photosynthesis research.[142,338]

There has been active discussion pertaining to the electron transfer routes within microorganisms incorporated into biophotoanodes as well as between the microorganism and the electrode surface.[157] However, the processes occurring between photon absorption and electron collection at the electrode, and hence any potential energy loss factors occurring within this diffusion, remain a mystery.[339] Specifically, a common and underlying obstacle amongst all BPV systems is that the electron transfer between the photosystems and the electrode remains poorly understood.[122] Several studies have attempted to characterise the photovoltaic processes in various BPVs in an attempt to better understand their behaviours such that their relatively low photocurrent amplitudes can be enhanced.[340–342] Elucidation of the precise electron transport and transfer processes within these systems would have dramatic implications for the future of photobiotechnology.[343]

Three potential transfer pathways have been postulated, following either direct electron transfer to the electrode from a protein embedded in a cell membrane, indirect electron transfer via redox species or indirect electron transfer via appendages on the cell membrane known as pili.[159,344] Electrochemical measurements by Zhang et al. in 2018 indicated that this process occurs by the mechanism of redox species-mediated electron transfer.[144] This study compared *in vivo* biofilms of cyanobacteria cells with analogous biophotoanodes comprising isolated photosystem II (PSII) films. Both PSI and PSII core complexes can also be wired to electrodes to afford photovoltaic devices analogous to those from cyanobacteria biofilms. Isolated photosystem devices typically afford much higher photocurrent amplitudes than cyanobacteria biofilms with photocurrent densities of up to 1 mA cm^{-1}.[166,345–347]

The aforementioned electrochemical results provide insightful guidance for explicitly assigning the electron transfer pathways following photon absorption within a cyanobacteria biofilm. However, spectroscopic techniques facilitate the direct comparison of photoinduced dynamics within cyanobacterial cells in their true *in vivo* natural state in solution with those exhibited when immobilised onto electrodes. Thus, in section 5.3.1, a range of spectroelectrochemical and spectroscopic techniques were employed to investigate the photoinduced processes in biophotoanodes comprising both PSII *in vitro* and Synechocystis *in vivo* alongside spectroscopic characterisation of Synechocystis *in vivo* in solution. The time constant of charge diffusion from PSII to the electrode within Synechocystis cells was quantified. The results indicate indirect electron transfer via diffusional redox species, in agreement with Zhang et al.'s conclusions from electrochemistry. Photoluminescence quenching was also investigated both for *in vivo* Synechocystis cells in solution and for those wired to an ITO electrode. Comparison of the quenching dynamics revealed that wiring cells to an electrode has dramatic consequences on the photoinduced processes within the cell, revealing that there are fundamental areas in the field of BPVs that are not yet fully understood.

5.1.2 The ultrafast photoinduced dynamics of photosynthesis *in vivo*

The near-unity efficiency of photosynthetic light-harvesting offers many lessons for mankind's endeavour to tackle the energy crisis.[175] However, there remain several knowledge gaps impeding our understanding of the operation of biological systems, which require direct interrogation of their ultrafast photoinduced dynamics. While many biological mechanisms occur on the timescale of milliseconds to seconds, they comprise a sequence of much faster rudimentary processes, such as charge and energy transport, which occur on the femtosecond to picosecond timescale.[348] The high efficiency of these fundamental steps facilitates the necessary ultrafast energy conversion and thus prevents the dissipative wasting of energy.[349] Hence the efficiencies of the elementary processes determine the overall efficiency of the composite biological process. Complex apparatuses composed of many highly efficient ultrafast steps can be found ubiquitously in biology, from photoisomerisation of rhodopsin granting us vision[350] to energy transfer in photosynthetic light-harvesting.[178,351]

A crucial component to photosynthetic light-harvesting in cyanobacteria is chlorophyll-*a* which harnesses photons and also enables charge separation in the reaction centre (RC). It is understood that chlorophyll-*a* exhibits two strong absorption bands in the visible region denoted the B and Q bands, at 400-470 nm and 650-700 nm respectively.[352] Given that chlorophylls are exposed to the full solar spectrum in nature, it is highly likely that a large proportion of the population are initially excited to the B band. After photoexcitation, the subsequent charge separation step is assumed to occur entirely from the Q band, which is generated within the RC in under 100 ps in order to activate the ensuing charge separation.[196] Rapid relaxation from the B band to the Q band is thus imperative in order to trigger the conversion of the electronic excitation into chemical energy.

This relaxation is not only fundamental for the process of photosynthetic light-harvesting, but its efficiency is also essential for photoprotection of the biological system. Ultrafast and efficient conversion of higher-lying singlet excited states (S_n) to the lowest-lying singlet excited state (S_1, on the Q band) inhibits the otherwise harmful conversion of the excitation into triplet states accessible via intersystem crossing. The possibility for ultrafast internal conversion from S_n to

S_1 thereby provides a safe pathway to deactivate routes to potentially dangerous states that cause photodamage on exposure to intense illumination, in a process termed non-photochemical quenching.[183,353] Access to this ultrafast and highly efficient relaxation thus not only promotes the efficiency of the photosynthetic process but also protects the organism from photodamage and preserves its robustness under operational conditions. However, while the charge separation mechanism has been investigated extensively,[191] the crucial relaxation from the higher-lying B band to the Q band has received little attention thus far.[354]

The ultrafast timescale of primary processes prohibits their comprehensive investigation with commonplace transient absorption (TA) measurements that allow time resolutions of approximately 100 fs.[348] However, developments in the field of ultrafast spectroscopy have rapidly advanced the applicability of these techniques to sub-picosecond elementary processes.[355] Specifically, over the last two decades, access to temporally-compressed pump pulses owing to commercially available chirped mirrors has driven the time resolution of TA spectroscopy to under 10 fs.[356] Such fine temporal resolution therefore now facilitates the observation of ultrafast rudimentary processes by TA techniques.[351]

In section 5.3.2, standard TA techniques with approximately 100 fs time resolution and sub-10 fs TA spectroscopy were both applied to investigate the ultrafast photoinduced dynamics within Synechocystis cells *in vivo*. The longer time resolution measurements were employed to confirm assignments of the observed features to fundamental transitions within chlorophyll-*a*. The same photophysical species were then probed with higher time resolution measurements. Subsequent deconvolution by global analysis allowed the elucidation of the sub-picosecond dynamics within the photosystem, quantifying the timescale of internal conversion from S_n to S_1 to be 45 fs *in vivo*. Furthermore, Fourier transformation of the time domain data afforded wavelength domain spectra, allowing detection of vibrational features by this impulsive technique. Multiple reproducible vibrations were observed, with those at 375 cm^{-1} and 500 cm^{-1} corroborated by previous studies *in vitro*.[175,357] The study thereby demonstrates the feasibility of investigating sub-picosecond dynamics in whole microorganisms *in vivo*, illustrating an exciting experimental step in the examination of photosynthetic systems.

5.2 Experimental details

5.2.1 Sample preparation

All samples were prepared according to the methods described in section 2.1.

5.2.2 Steady-state absorption spectroscopy

Steady state absorption spectra were measured using the technique outlined in section 2.2.1.

5.2.3 Steady-state photoluminescence spectroscopy

Steady state photoluminescence spectra were measured according to the procedure described in section 2.2.2.

5.2.4 Time-correlated single photon counting

Time-correlated single photon counting (TCSPC) measurements were carried out according to the technique described in section 2.4.

5.2.5 Incident photon-to-electron conversion efficiency

Incident photon-to-electron conversion efficiency (IPCE) measurements were carried out using the setup developed as described in section 2.2.3. All biophotovoltaic devices were submerged in MES buffer (Sigma-Aldrich) in order to facilitate water splitting and thus enable their function as biophotoanodes. These were incorporated into an electrochemical cell using a platinum counter electrode.

5.2.6 Transient absorption spectroscopy

TA spectra with ∼100 fs pump pulses were obtained using the experimental setup outlined in section 2.3.2. A 500 μm sample path length was used with constant stirring of the suspension in order to enhance the longevity of the measurement. TA spectra with ∼10 fs pump pulses were collected using the experimental setup described in section 2.3.5 with a 50 μm path length in order to preserve the high time resolution.

5.3 Results and discussion

5.3.1 Comparison of the photosynthetic processes within biophotovoltaic devices *in vitro* and cyanobacteria cells *in vivo*

Preliminary measurements were carried out to verify the detection of photocurrent from Synechocystis cells when adsorbed to an ITO electrode and incorporated into an electrochemical cell, using a monochromatic continuous-wave laser. Figure 5.1 summarises the confirmation of photocurrent detection using 675 nm excitation, resonant with chlorophyll-*a* $S_0 \rightarrow S_1$ absorption, as well as the linear relationship between light intensity and photocurrent.

The detection of photocurrent by continuous-wave illumination, in conjunction with the negligible photocurrent observed for bare electrodes, confirms that the preparation technique of dropcasting the cyanobacteria cells onto electrodes successfully produces photoactive biofilms. The linear relationship between light power and photocurrent confirms that photosynthetic light-harvesting is being observed before the saturation point. Previous BPV studies have shown that photocurrent increases with light power until it reaches intensities that are too high and damage the photosynthetic machinery. At this point, the current becomes saturated or depleted.[174,335,358] Hence this measurement confirms the presence of a linear regime within the relationship between intensity and current, such that any subsequent measurements within this region can be assumed to be light-limited as opposed to operating in the saturation regime.

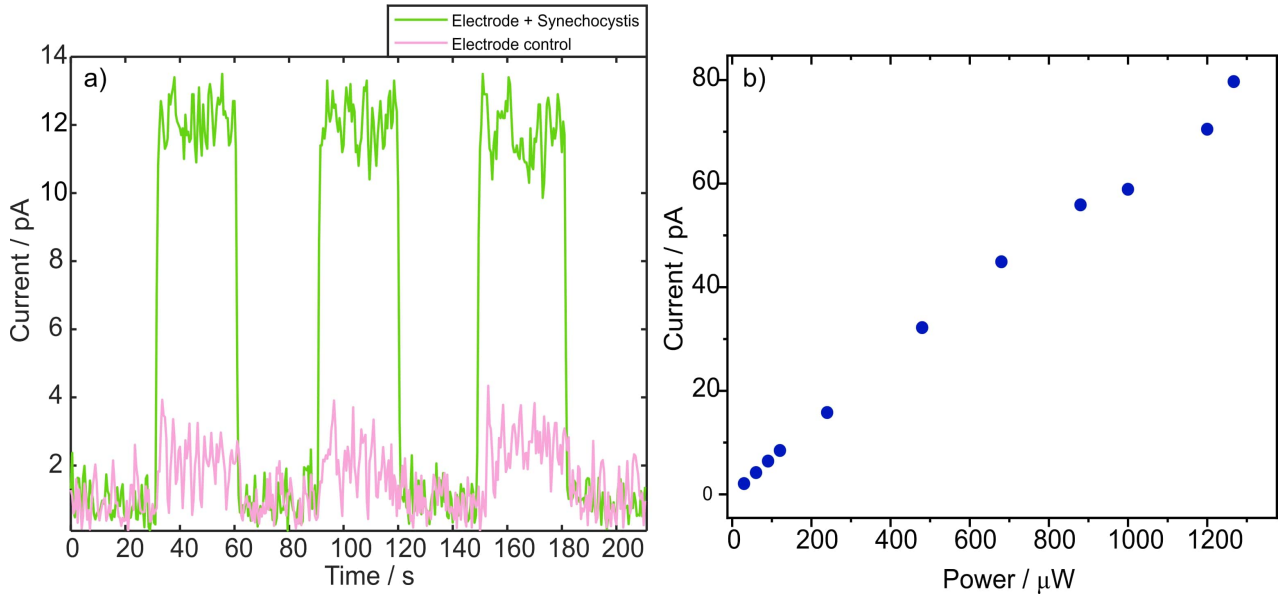


Figure 5.1: a): Generation of photocurrent by continuous-wave illumination (675 nm, 255 μWcm^{-2}) switched on at 30 s, 90 s and 150 s, and switched off at 60 s, 120 s and 180 s. A bare electrode control measurement is also shown for evidence of cyanobacteria contribution. b): Linear relationship between photocurrent and light intensity.

The IPCE spectrum of the Synechocystis BPV was obtained and compared with the well-understood absorption spectrum that is characteristic of photosynthetic light absorption in cyanobacteria. It was therefore verified that the detected electrons originate from photosynthetic pigments. The IPCE spectra of biophotovoltaic devices prepared with isolated PSII - rather than whole cyanobacteria cells - were also measured for comparison. The resultant spectra are shown in figure 5.2.

It is clear from the raw IPCE spectrum (figure 5.2a) that the IPCE for the isolated PSII devices is appreciably greater than for *in vivo* cells, affording approximately ten times the photocurrent at wavelengths corresponding to the absorption maxima. This is an expected result due to the density of photoactive pigments within the sample. The cyanobacteria cells occupy approximately 1.6 μm diameters on the electrode, of which a minor contribution comes from photosynthetically active complexes, while the PSII films are entirely composed of these nm-sized proteins.[144] Therefore, the quantity of chromophores and systems for charge separation is dramatically greater for PSII films than for cyanobacteria films. Hence in order to directly compare the shapes of the spectra, the results were normalised and are presented in figure 5.2b.

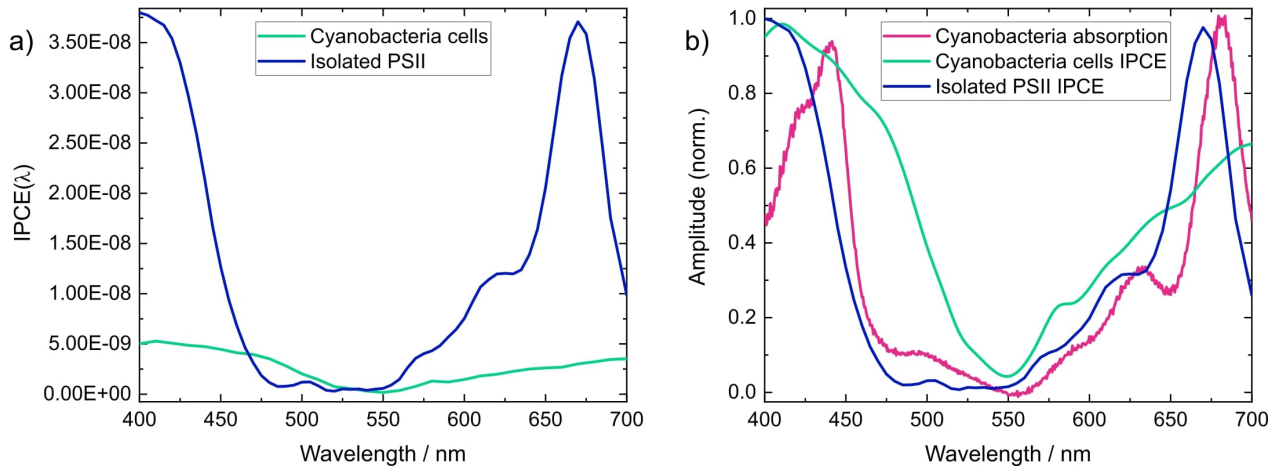


Figure 5.2: a) Raw IPCE spectra for isolated PSII and Synechocystis cells. (b) Normalised IPCE spectra for isolated PSII and Synechocystis cells, as well as absorption spectra for Synechocystis cells in suspension.

The PSII IPCE spectrum shows significant agreement with the absorption spectrum of the *in vivo* cells, even showing shoulder peaks at 570 nm and 625 nm arising from phycocyanin antenna pigments within the phycobilisomes.[359] These, as well as the dominant peak from chlorophyll-*a* ground state absorption at 670 nm, are slightly blue-shifted relative to the cells' absorption spectrum. This is attributed to the interactions between PSII and its surrounding environment *in vivo*, which causes a slight relaxation of the energy level compared to the isolated PSII.

There is a vast discrepancy between the PSII IPCE spectrum and cells' absorption spectrum in the region of 400-430 nm. There is contribution to the absorption from carotenoid antenna pigments in this region.[360] However, it should be exceeded by the chlorophyll-*a* higher-lying absorption - which peaks at 440 nm - due to the overwhelming majority of chlorophyll-*a* pigments compared to carotenoids, as is evident in the absorption spectrum. This discrepancy is suggested to arise due to contributions from the ITO electrode which was determined to absorb blue light in control measurements. Otherwise, it can be confirmed that the PSII BPV generates photocurrent directly from photosynthetic absorption processes by the resemblance between the two spectra.

The *in vivo* cyanobacteria IPCE spectrum bears poorer resemblance to its absorption spectrum compared with isolated PSII. However, there is definite photogeneration of charges within the

principal absorption regions of blue and red light at the far edges of the spectrum, with the minimum at 550 nm consistent between both spectra. The contrast between the spectral features in the PSII vs. cyanobacteria cells IPCE is attributed to the significantly lower signal-to-noise ratio caused by the tenfold lower photocurrent amplitude *in vivo*.

With such low photocurrent amplitudes, contributions to the signal were often overwhelmed by electrical background currents which made data collection much more complicated for *in vivo* samples than for isolated PSII. In an attempt to combat this, the IPCE setup was optimised and developed by first automating its operation such that it could be run for several repeat scans to increase the signal-to-noise ratio. The background electrical contributions were also excluded by implementation of lock-in amplification and a Faraday cage to isolate the photoinduced electrical signals coming from the electrochemical cell only.

Despite the poorer quality of the cyanobacterial cells' IPCE spectrum compared with isolated PSII, this data confirmed that the detected photocurrent originates from photosynthetic absorption processes due to the general agreement between the key spectral regions. The photocurrent generated by 675 nm excitation (as shown in figure 5.1) was thus interpreted to arise from absorption within the photosynthetic pigments and was selected for the subsequent time-resolved measurements.

Using a 675 nm continuous-wave laser, a Synechocystis BPV was illuminated in an electrochemical cell and the laser modulation frequency given by an optical chopper was varied. Figure 5.3 shows the variation of photocurrent amplitude with modulation frequency, which can be seen to undergo significant suppression with increasing frequency.

The attenuation of photocurrent with increasing modulation frequency is an expected result and can be understood according to the Cole-Cole model for dielectric relaxation in disordered systems.[361] In this case, the Cole-Cole equation can be implemented to quantify the lifetime of the diffusion limit of a random walk of photogenerated charges.[362] The data can be modelled according to the following equation:

$$Current = \frac{C}{(1 + i\omega\tau)^{\alpha}} \tag{5.1}$$

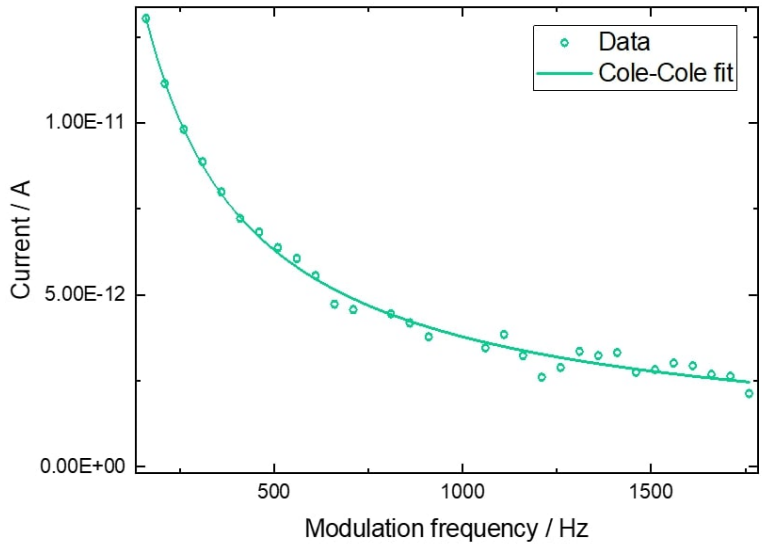


Figure 5.3: Photocurrent detected with 675 nm excitation for a BPV comprising *in vivo* Synechocystis cells, as a function of laser modulation frequency given by an optical chopper.

Where C is the static dielectric constant, ω is the angular frequency and τ is the diffusion time constant. The attenuation curve in figure 5.3 was thereby modelled according to equation 5.1 to extract the time constant, which was quantified to be 0.0083±0.0026 s. This signifies that on photoexcitation in chlorophyll-*a* pigments, the time required for photogenerated charges to reach electrodes for collection is approximately 8 ms.

The transport of free charges generated during photosynthesis along the electron transport chain is understood to occur on the milliseconds to seconds timescale, although the precise lifetimes of each charge transfer step is not known.[363] In order for direct electron transfer across the membrane and also for indirect electron transfer via pili to be possible, charges must not only travel out of the reaction centre but must also diffuse through the cell cytoplasm to reach the membrane in order to meet the electrode interface. Cellular diffusion is also expected to occur on the millisecond to second timescale.[364] Therefore, the 8 ms Cole-Cole derived timescale is considerably fast compared to the proposed mechanisms of direct electron transfer and pili-mediated electron transfer, thus precluding their action. This therefore suggests that electron transfer occurs by the indirect electron transfer process mediated by redox species, as was suggested by aforementioned electrochemical studies.[144]

Thus far, BPV devices employing cyanobacteria are largely assumed to retain *in vivo* be-

haviours and photosynthetic processes. However, it is highly plausible that the immobilisation of microorganisms onto conductive electrodes would impact their photoinduced dynamics. The natural photosynthetic apparatus is exposed to an external electron sink when incorporated into a BPV which establishes a new equilibrium amongst the redox processes involved in photosynthesis, the impact of which remains unknown.[122] In order to investigate the extent to which this electrode wiring influences the temporal evolution of states within cyanobacteria cells, TCSPC was employed to elucidate the photoluminescence (PL) quenching dynamics within cells in solution (which were therefore doubtlessly exhibiting *in vivo* equilibrium behaviour) as well as within those immobilised onto electrodes. This technique allows the application of the same detection regime and measurement conditions to both solution samples and biofilm samples, allowing direct comparison between biofilm cells and free cells.

A 635 nm excitation wavelength was selected, resonant with phycobilisome absorption, which was measured using steady-state PL spectroscopy to be highly emissive.[359] Figures 5.4a and b show the PL spectra for cells in solution and those immobilised onto electrodes, respectively, as a function of both excitation and emission wavelengths. The 400-450 nm excitation range is assigned to the chlorophyll-*a* absorption from S_0 to a higher-lying excited state, S_n. The broad and strong PL signal spanning the 600-700 nm excitation range is assigned to a combination of phycobilisomes and the chlorophyll-*a* $S_0 \rightarrow S_1$ transition, either by direct absorption within the RC or by absorption within the antenna pigments followed by subsequent energy transfer to chlorophyll-*a* resulting in formation of its S_1 state. Both samples are evidently strongly emissive in the red region. Figure 5.4c shows a slice of the solution sample at 635 nm excitation, depicting a strong PL signal with a peak at 714 nm. This wavelength was thus selected as the detection wavelength for subsequent TCSPC measurements.

Figure 5.4d shows the time-dependent PL quenching for cells in solution and those incorporated into a device by immobilisation on an electrode. The grey IRF trace represents the instrument response function. It is evident that PL quenching is accelerated within cyanobacteria cells when wired to electrodes in contrast with those in solution, even when the electrode is not connected to a circuit or exposed to applied bias.

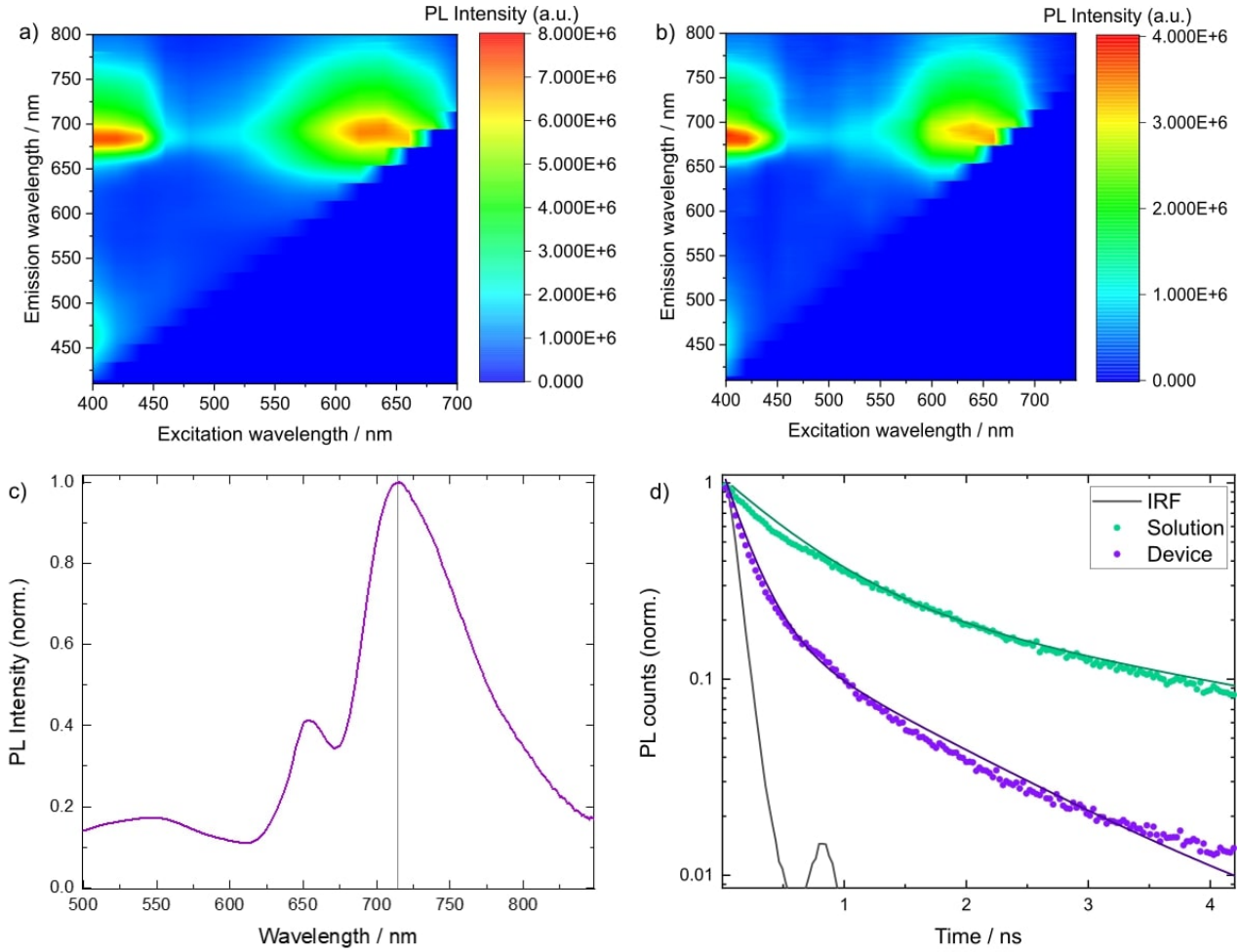


Figure 5.4: Steady-state photoluminescence spectra of a) Synechocystis cells in suspension and b) Synechocystis cells immobilised onto electrodes. c) Steady-state photoluminescence spectrum of Synechocystis cells in suspension following 635 nm excitation. b) PL quenching dynamics of cells in solution and those wired to an electrode to afford a BPV device. IRF = instrument response function.

Both traces were fitted to biexponential curves to quantify their decay lifetimes and in both cases a picosecond component and a nanosecond component were observed, which are summarised in table 5.1. Both components to the decay were found to be three times faster in cyanobacteria cells when wired to electrodes by contrast with those in buffer solution.

Cell environment	**Fast decay component / ps**	**Slow decay component / ns**
Solution	634 ± 4	3.84 ± 0.03
BPV device	200 ± 1	1.29 ± 0.01

Table 5.1: Time constants for PL quenching in cyanobacteria cells in solution and those immobilised onto an electrode to afford a BPV device.

The accelerated PL quenching reveals that the dynamics of photoinduced processes within cyanobacteria cells are significantly influenced by their wiring to electrodes. This finding emphasises the extent to which the photosynthetic mechanisms in BPVs are not yet understood. Therefore, these results demonstrate that considerable further work is required in order to fully understand the generation of electrical current in photobiotechnology.

5.3.2 The ultrafast photoinduced dynamics of photosynthesis *in vivo*

Transient absorption spectroscopy with ~100 fs pump pulses

Figure 5.5 shows the TA spectrum of a suspension of Synechocystis cells *in vivo*, dispersed in solution with MES buffer, measured according to the method detailed in section 2.3.2. This data was collected following excitation with a 440 nm pump, resonant with the dominant higher energy absorption of chlorophyll-*a*, measured in the visible probing region.[365] The main features are the photoinduced absorption spanning from 600–675 nm, and the ground state bleach (GSB) from 675–775 nm. The former has been previously assigned in the literature (in studies on isolated PSII) to chlorin excitons and anions, while the latter is well understood to arise as a result of the chlorophyll-a $S_0 \rightarrow S_1$ absorption.[366,367]

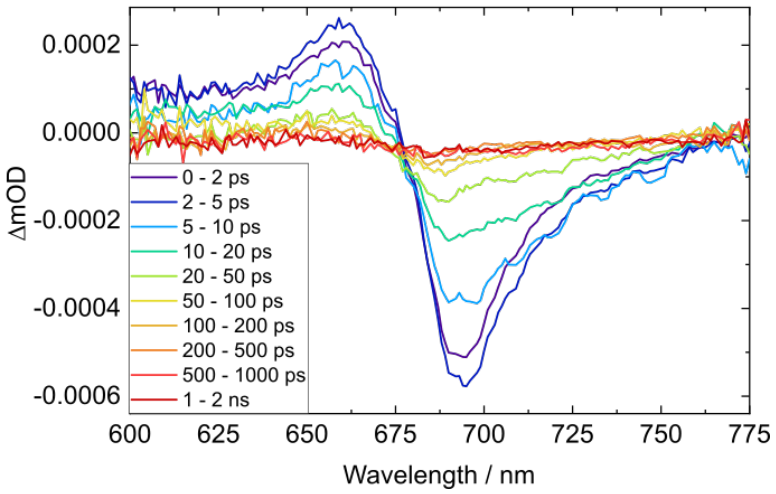


Figure 5.5: a):Transient absorption spectrum of cyanobacteria cells in suspension dispersed in MES buffer solution following 440 nm pump excitation (50 nJ, 100 fs time resolution).

There is also some contribution to the feature at 695 nm from the stimulated emission (SE) component. Figure 5.4a shows the photoluminescence spectrum of the suspension of cyanobacteria where the 600-700 nm excitation range is assigned to the chlorophyll-*a* S_1 state. This spectrum reveals that the S_1 state on chlorophyll-*a* is highly emissive, hence it is expected that a large contribution to the negative feature in the TA spectrum arises from SE.

Both signals in the TA spectrum can be observed to decay gradually over the 6 ns timescale of the measurement, consistent with the timescale of separated charges being transferred into the electron transport chain previously observed in bacterial reaction centres.[368] However, the ingrowth of further signals was not detected here and thus it is not possible to experimentally confirm their formation. This measurement was predominantly used to confirm the presence of signals assigned in the literature arising from PSII in order to verify our understanding of the photoinduced processes *in vivo* and hence to inform the following ultrafast measurements.

Transient absorption spectroscopy with sub-10 fs pulses

The TA measurements were then repeated with the experimental technique described in section 2.3.5 with sub-10 fs pump pulses in order to achieve higher time resolution. Due to the temporal pulse compression, the pump pulse undergoes a degree of spectral broadening and the following data were collected using a 395–420 nm pump pulse. We maintain the assumption that this pump wavelength excites chlorophyll-*a* to its higher-lying excited state, S_n. The resulting spectrum is shown in figure 5.6a for the 1 ps timescale of the measurement. The dominant PIA and GSB/SE features from the slower TA are still present on the sub-picosecond timescale. The PIA can be observed to redshift over the timescale of the measurement, which has been observed previously on slower timescale measurements of isolated PSII. Furthermore, there is an additional GSB feature at 750 nm which has not yet been detected in the literature. Current ongoing work carried out by our collaborators, employing mutant cells and isolated photosystems, suggests that this feature originates from PSI.

Comparison of the temporal evolution of the dominant GSB feature and the PIA reveals that the two states have different rise times. The kinetics were extracted from the 635–665 nm and

685–705 nm regions for the PIA and GSB respectively. The data were fit to monoexponential functions to quantify the lifetime of the growth of the signals and are plotted in figure 5.6b. The time constants associated with the rise of the GSB and PIA signals were found to be 33 fs and 66 fs, respectively. This confirms that the two spectral features must be assigned to distinct photophysical states; it is not possible that they originate from the same photoexcitation event, as the GSB is formed somewhat instantaneously while a delayed onset is observed for the PIA. Both features show flat dynamics after their initial rise, which is expected on the sub-picosecond timescale given that both were observed to decay on the timescale of hundreds of picoseconds in the slower TA measurement.

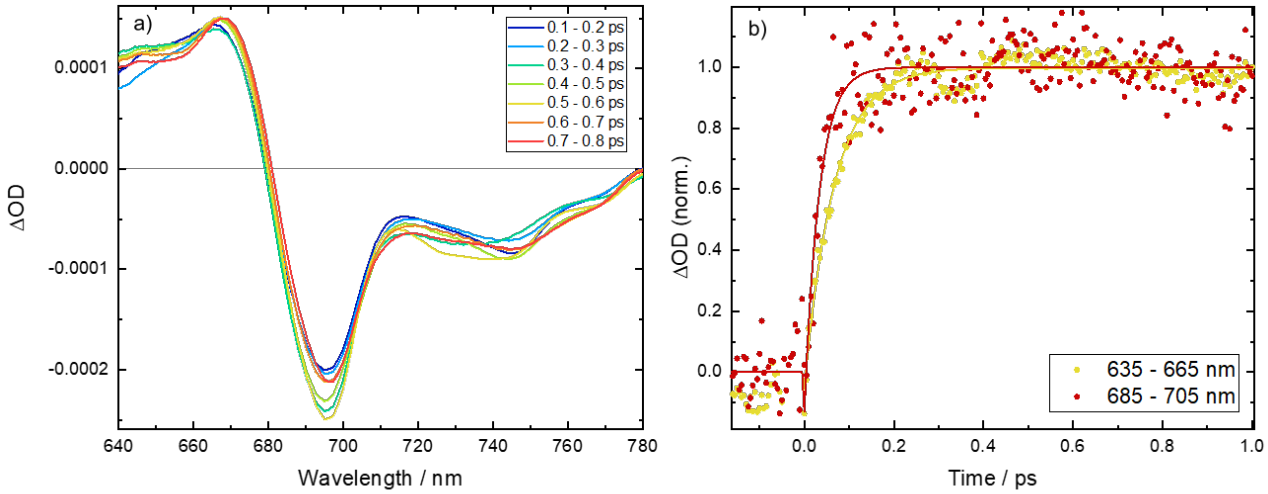


Figure 5.6: a): Transient absorption spectrum for cyanobacteria cells *in vivo* in suspension dispersed in MES buffer solution with a 395-420 nm pump (320 μW, ~12 fs time resolution). b) The kinetics extracted for the PIA and 695 nm GSB feature.

Global analysis was implemented to deconvolute the spectrum into distinct photophysical species in order to understand the above dynamics. The resultant spectra and kinetics of the components are shown in figure 5.7. The spectrum was resolved into two species: the GSB feature peaking at 680 nm, assigned to chlorophyll-*a* ground state absorption, and a second component comprising both the PIA and the SE. The fact that the PIA and SE are formed on the same timescale indicates that they originate from the same state. The kinetics reveal that the GSB feature is formed instantaneously on pump absorption and decays very promptly. The two components are assigned to the S_1 and S_n states on chlorophyll-*a*, which is explained in the following discussion. The assignments are corroborated by a prior study in which identi-

cal deconvoluted spectral components are observed in isolated chlorophyll-*a* molecules and are therein also assigned to S_1 and S_n.[354]

Both components were fit to a monoexponential curve and time constants were derived to be 45±0.7 fs and 43±2 fs for GSB decay and PIA/SE onset respectively. The remarkable synchronicity of these processes indicates that the excited state formed by chlorophyll-*a* ground state absorption subsequently evolves to form the species represented spectrally by the PIA/SE component. The kinetics in figure 5.7 also make this apparent by eye, where the two traces appear to perfectly mirror each other, illustrating the process of the initial state evolving to form a new state.

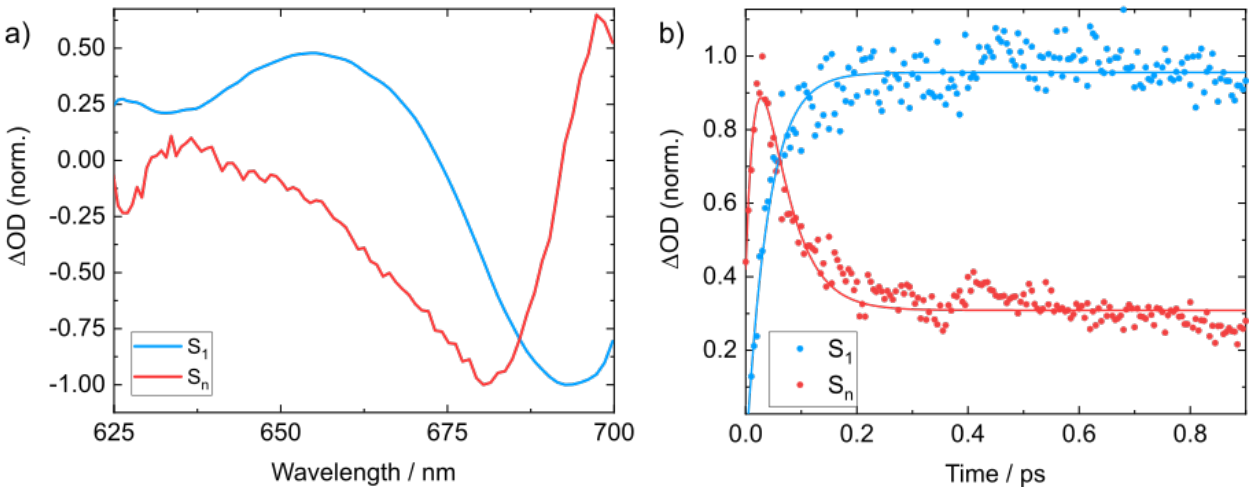


Figure 5.7: Spectra (a) and kinetics (b) for the two photophysical components extracted from the TA spectrum in figure 5.6 using global analysis.

Collating the observations, the following model was devised to rationalise the sub-picosecond dynamics observed in TA spectroscopy and is illustrated in figure 5.8. The broad blue pump excites chlorophyll-*a* from its ground state to the higher-lying S_n state. This instantaneously depletes the 680 nm $S_0 \rightarrow S_1$ transition due to depopulation of the ground state resulting in instantaneous bleaching at 680 nm. On a slower timescale, the S_1 state is formed, resulting in the onset of detection of PIA from S_1 to S_n as well as SE from S_1 to S_0. The GSB arising from excitation to S_n simultaneously begins to decay as S_n is depopulated while photophysical processes originating from S_1 begin to emerge as the S_1 population grows, as is observed in the concomitant dynamics of the processes. This indicates that the S_n state evolves to form the

S_1 state. It is well understood that the higher-lying excited states on chlorophyll-*a* undergo rapid internal conversion to S_1, from which 100 % of the subsequent charge separation steps occur, in order to then trigger charge transport along the electron transport chain. Previous studies by Meneghin et al. employing two-dimensional electronic spectroscopy have reported an ultrafast component to the internal conversion from S_n to S_1 that was estimated to occur with a 40 fs timescale.[357] This is in remarkable agreement with the timescale derived herein by global analysis and we therefore attribute this delayed rise of the S_1 component to its formation by internal conversion from S_n. The lifetime of this process *in vivo* is thereby quantified to be 45 fs from the fits to the kinetics from global analysis.

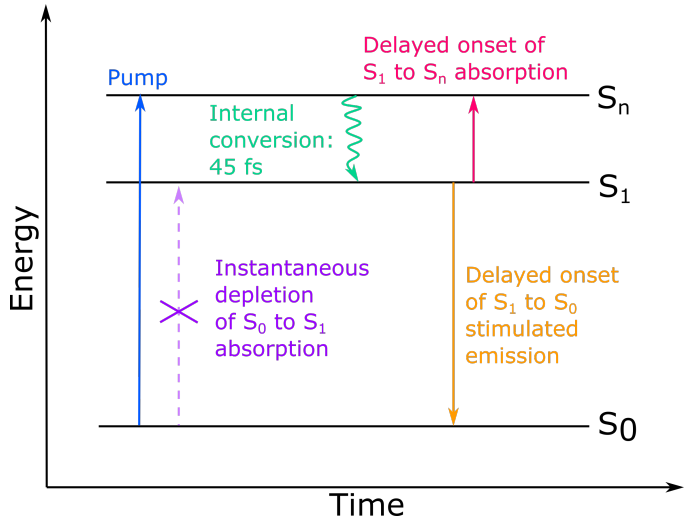


Figure 5.8: Energy level diagram of the photophysical model proposed to rationalise the sub-picosecond dynamics observed in TA measurements.

As discussed in section 2.3.5, the dynamics of the spectroscopic signal in high time resolution TA measurements can exhibit oscillations as a result of the temporal evolution of the vibrational wavepacket.[369] The frequencies of these oscillations correspond to vibrational frequencies on the excited state which can be retrieved by Fourier transformation of the time domain signal. The Fourier transform was thus applied to the time domain data from the sub-10 fs TA measurements in order to observe the signals in the frequency domain. Figure 5.9 shows the spectra derived by this analysis in the $S_1 \rightarrow S_n$ PIA region for three separate repeat measurements in order to verify the reproducibility of the findings.

It should be noted that at the time of writing this thesis, this part of the project is very much

in its infancy. There are therefore imperfections to the approach discussed herein with several implications for further work and improvement. In this context, the principal limitation is that these three measurements were carried out with different time resolutions of 10 fs, 5 fs and 2 fs (for figures 5.9 a, b and, c respectively). This is reflected in the sharpness of the peaks in figure 5.9c in contrast with the relatively broadened peaks in figure 5.9a.

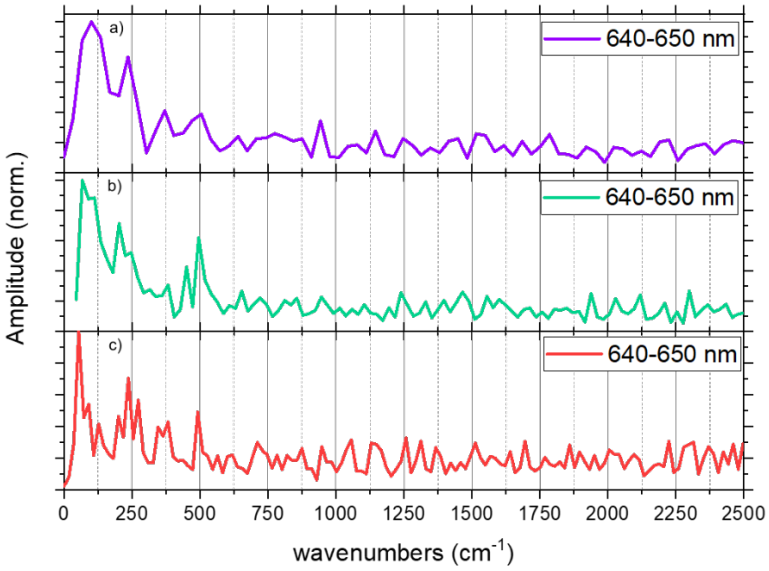


Figure 5.9: Frequency-domain data extracted by Fourier transform of the sub-picosecond TA spectrum in figure 5.6 to afford excited state vibrational spectra of *in vivo* cyanobacteria cells from three different measurements to demonstrate reproducibility.

Several frequencies were detected in these measurements with the key features appearing at 60 cm^{-1}, 250 cm^{-1}, 375 cm^{-1} and 500 cm^{-1}. The reproducible nature of these oscillations across the three measurements confirms the *in vivo* detection of vibrational states on the excited state within the cyanobacterial cells. As the analysis is carried out on the PIA region where the most prominent oscillations were detected, these oscillations are interpreted to involve the vibrational manifold on the chlorophyll-*a* S_1 electronically excited state.

The oscillations detected at 375 cm^{-1} and 500 cm^{-1} are in significant agreement with those previously attributed to vibronic states on S_1, reported at 340 cm^{-1} and 510 cm^{-1}.[175,357] Both prior studies were carried out on isolated photosystems, whereas here they are detected *in vivo*. Hence the small discrepancies in oscillation frequencies could arise due to the interactions of the reaction centre with its surrounding medium, affecting the energy levels of the vibronic

states in the systems studied herein, which does not occur when they are isolated.

Moreover, our assignment of the dynamics on the PIA to ultrafast internal conversion from S_n to S_1 indicates that the observed vibrations are coupled to this relaxation process. In particular, the study by Meneghin et al. concluded that this ultrafast internal conversion involves vibronic states at 510 cm^{-1} within the manifold on S_1.[357] This is consistent with our detection of 500 cm^{-1} vibrations within S_1. It is also otherwise well-established that vibronic states on S_1 are involved in electronic relaxation from higher-lying states in photosynthetic light-harvesting.[354] We therefore suggest that this is an exciting result demonstrating the *in vivo* measurement of the vibrational energy levels coupled to the S_1 excited state in cyanobacteria.

5.4 Conclusions

In this work, the photosynthetic processes within Synechocystis cyanobacterial cells *in vivo* were investigated by a range of electrochemical and spectroscopic techniques. Spectroelectrochemical measurements were employed to quantify the timescale of charge diffusion from the photosystem to the electrode in cyanobacteria biophotoanodes. The timescale was determined to be 8 ms, suggesting the action of an indirect electron transfer mechanism at the cell-electrode interface via redox species. TCSPC revealed that PL quenching occurs much faster in cyanobacteria cells when immobilised on electrodes compared to those in their natural state in solution, suggesting the incorporation into a BPV device drastically influences the photoinduced dynamics within the cell.

Transient absorption spectroscopy with sub-10 fs pump pulses was used to interrogate the sub-picosecond dynamics in cyanobacteria cells *in vivo*. Deconvolution of the data by global analysis shows internal conversion from S_n to S_1 occurring with a 45 fs lifetime, consistent with previous reports. Application of the Fourier transform facilitated observation of oscillation frequencies arising from vibrational levels within the manifold of vibrational states on S_1. This result therefore presents the first implementation of impulsive vibrational spectroscopy by the sub-10 fs pump-probe technique in photosynthetic light-harvesting *in vivo*, with promising implications

for future investigations. The ability to directly probe the excited state vibrational spectrum and its temporal evolution *in vivo*, rather than in an artificial representative system, unlocks the potential to expose the true photophysical nature of biological light-harvesting. Observing these dynamics on living microorganisms can thus provide crucial lessons by which to inform our development of highly-efficient photovoltaic materials.

Chapter 6

Conclusions and Outlook

In this thesis, spectroscopic tools were employed to investigate the fundamental photophysical behaviours in a diverse range of "soft" photovoltaic materials. Organic, hybrid and biological systems were explored in an attempt to rationalise their light-harvesting characteristics in terms of their time-resolved photoinduced mechanisms. With this approach, it is possible to expand our understanding of the photovoltaic processes within next-generation solar cell materials, as well as in biological systems that are billions of years ahead of us in their optimisation of efficiency. The conclusions derived from these studies thereby provide invaluable lessons for the design of state-of-the-art solar cells in order to realise efficient, low-cost and environmentally friendly energy generation.

6.1 Conclusions

Chapter 3 considered the photophysical consequences of regioisomeric molecular tuning in two systems employing small molecules for OPVs. A pair of push-pull molecules, structurally identical aside from a 1-carbon displacement of an alkyl chain, were studied due to interesting results revealing that they exhibited opposite operational behaviours in OPVs. This minor structural modification was reported to invert the molecule's preference for operation as a donor or acceptor component and the study presented herein investigated this contrast by transient absorption

spectroscopy.[370] Global analysis of the time-resolved data rationalised the device performances of the D:A blends in terms of exciton dissociation and charge carrier recombination lifetimes. The second study examined optoelectronic consequences of the position of a chalcogen substitution on a commonly employed NFA. Transient absorption spectroscopy and subsequent global analysis exposed stark differences in the materials' charge separation dynamics when blended with a donor polymer. The discrepancy in the NFA's exciton diffusion lifetimes were justified in terms of blend morphology, which was found to be heavily influenced by the regioisomeric structure. Together these studies emphasise the intricacy of the structure-function relationships in candidate molecules for OPVs.

In chapter 4, the focus was shifted from photovoltaic performance to the operational stability of prospective components. Like chapter 3, the discussion was approached from the perspective of two distinct studies in order to provide a thorough demonstration of the unique and diverse applications of time-resolved spectroscopic tools. Transient absorption spectroscopy of a blend containing a small molecule donor and a fullerene acceptor unveiled an unprecedented intrinsic photoprotection mechanism, granting the material exceptional stability relative to analogous blends. The same experimental technique was also applied to a range of quantum dot solar cell devices employing varied charge extraction layers in order to elucidate the charge trapping dynamics and reconcile them as a consequence of degradation. This chapter thereby highlighted the nuanced relationship between photovoltaic materials and operational stability. More importantly, however, this work illustrated the great potential of ultrafast spectroscopy for the deconvolution of degradation and photoprotection mechanisms, where operational stability has conventionally been investigated by steady-state methods. This chapter also emphasised the significant impact that device architectures and charge extraction layers have on device stability, thus depicting the importance of implementing time-resolved spectroscopic techniques on complete devices rather than focussing only on active layers.

Chapter 5 presented a sidestep from the conversation around synthetic soft semiconductors by delving into photosynthetic light-harvesting. Both steady-state spectroelectrochemical and time-resolved spectroscopic methods were implemented to characterise biophotovoltaic devices employing whole cyanobacteria microorganisms *in vivo*. The results shed light on exoelectro-

genesis mechanisms while highlighting the presence of fundamental gaps in our understanding of the operation of these systems. Application of transient absorption spectroscopy with sub-picosecond time resolution to the *in vivo* cells provided significant insight into the ultrafast photoinduced processes within the photosynthetic apparatus. Observation of periodic modulations to the signal allowed construction of a vibrational spectrum by Fourier transformation thus facilitating the impulsive measurement of the excited state vibrational spectrum of the system. The results of this study therefore not only elucidated the photophysical processes within the photosynthetic reaction centre but also demonstrated the applicability of advanced spectroscopic techniques to highly complex biological systems.

6.2 Outlook

6.2.1 Maximising OPV performance

This thesis evinces considerable consequences of seemingly insignificant molecular modifications on the optoelectronic properties of OPV devices. Logical extrapolation of this argument leads us to the notion that there exists an infinitely large pool of possible molecules for better-performing organic semiconductors. Experimental analysis of each new candidate for OPV application necessitates expensive synthesis, purification and device fabrication procedures for the iterative enhancement of performance. Design principles have been widely accepted to demand incorporation of electron-rich cores, π-spacers and flanking electron-withdrawing motifs. However, the infinite number of potential combinations of these moieties means that conjecture remains around the subject of performance-targeted structure optimisation. High-throughput virtual screening therefore presents a cheaper approach for characterising a molecule's applicability to photovoltaic devices by computing their optoelectronic properties and thus ascertaining new design principles for OPV components.[371,372] Indeed, the rapid screening of millions of different organic molecules has resulted in the recent proposal of promising new contenders.[373]

However, the presently applied model in this approach employs density functional theory, cal-

culating only the frontier molecular orbitals of the molecules.[374] It therefore does not accurately compute PCEs of photovoltaic materials. Developing this technique to integrate machine learning for direct PCE calculation could introduce remarkable advances in the efforts to find next-generation OPV materials, as has already been demonstrated in the discovery of novel drugs and materials.[375–378] Recent reports have thereby developed machine learning models to calculate efficiencies and screen tens of thousands of molecules for OPVs, exposing new design principles for the relative combinations of the key building blocks in organic semiconductors.[379,380] Nonetheless, computational prediction of the optoelectronic characteristics of candidate molecules is still a long way from accurately determining their behaviours when blended with another component in a bulk heterojunction and sandwiched between charge extraction layers and electrodes. Hence a combination of machine learning predictions together with time-resolved spectroscopic techniques and device performance measurements could provide a powerful tool for the efficient and cheap discovery of new molecules for OPVs.

Arguably the most important consideration for advancing the efficiency of next-generation photovoltaic devices is geminate recombination (GR). As the principal process of charge recombination in OPVs, GR essentially determines the overall efficiency of the material.[381] The intrinsic complexity arising due to intricate morphologies, charge mobilities, charge traps and disorder within OPVs mean that a complete picture to comprehensively understand GR is still in its developmental stages. Results from time-resolved experiments revealed that spin plays a key role in recombination processes; Rao et al. showed that GR produced triplet excitons in some polymer:fullerene blends which induced energy loss due to annihilation of triplets by charges.[382] Combination of these results with steady-state performance measurements should provide routes for better characterisation of GR losses and their triggers in order to form methods for the suppression of recombination.

6.2.2 Towards operationally stable organic solar cells

While the ever-advancing efficiencies of soft materials for photovoltaics is exciting, the general lack of operational stability exhibited across this field remains a major hurdle inhibiting

their commercialisation. Perpetual effort to enhance device performances remains futile if they are never to be applicable to real-world operation, potentially manifesting years of wasted research efforts. This thesis presents an interesting perspective on this subject by ultrafast spectroscopy, which is sparsely-employed in the consideration of stability. This work indicates that the application of time-resolved spectroscopic methods can better elucidate degradation and photoprotection processes in order to better our understanding of how to improve the longevity of photovoltaic devices.

In particular, the direct observation of an ultrafast photoprotective mechanism presents a promising result which should be investigated further. Harnessing this effect such that it can be achieved by design, in conjunction with molecular optimisation for maximisation of device efficiency, offers a new and exciting opportunity for the union of impressive photovoltaic performance and appreciable stability. Specifically, the system studied in chapter 4 exhibited a PCE of 8 % which could be enhanced by molecular tuning, in parallel with investigation of the ultrafast dynamics in order to investigate whether the photoprotective mechanism is maintained or suppressed.[215] It could thus be possible to deliberately preserve the intrinsic photoprotection mechanism that is fundamental to this material's stability, while simultaneously tuning its optoelectronic properties in order to boost its efficiency. This approach could hence grant a promising pathway to developing the industrial applicability of soft materials for photovoltaics.

6.2.3 Ultrafast spectroscopic techniques for investigating photosynthesis

The work in this thesis provides an intriguing outlook for the application of complex transient spectroscopic methods to *in vivo* biological systems. Time-resolved techniques have been applied extensively to isolated photosystems and photosynthetic chromophores in the literature.[383–385] However, the nuanced relationships between these biomolecules and their native environment hinders these experiments' ability to truly represent the optical dynamics of photosynthesis *in vivo*. Surprisingly, the measurements presented in chapter 5 afforded clear spectroscopic signals aligned with those reported in isolated photosystems with remarkable

simplicity. By observation of sub-picosecond dynamics for impulsive vibrational spectroscopy, this study pushed the boundaries of the implementation of ultrafast spectroscopy for *in vivo* microorganisms. Going forward, by employing mutant cells lacking certain pigments, the vibrational spectra of relevant chromophores within the *in vivo* system can be measured by Raman spectroscopy[386] in order to assign the wild type spectrum. Alignment of these two techniques could provide an effective approach for the direct observation and assignment of excited state vibrational spectra in biological microorganisms *in vivo* in order to accurately represent their natural photosynthetic machinery. This could therefore present encouraging implications for better elucidation of the ultrafast processes entangled within photosynthesis concerning molecular structure and dynamic disorder. Thereby gleaning lessons from nature about methods for achieving highly-efficient solar light-harvesting, it could be possible to optimise the design of state-of-the-art soft photovoltaic materials such that they could outcompete unsustainable energy resources.

Appendix A

$PC_{70}BM$ absorption

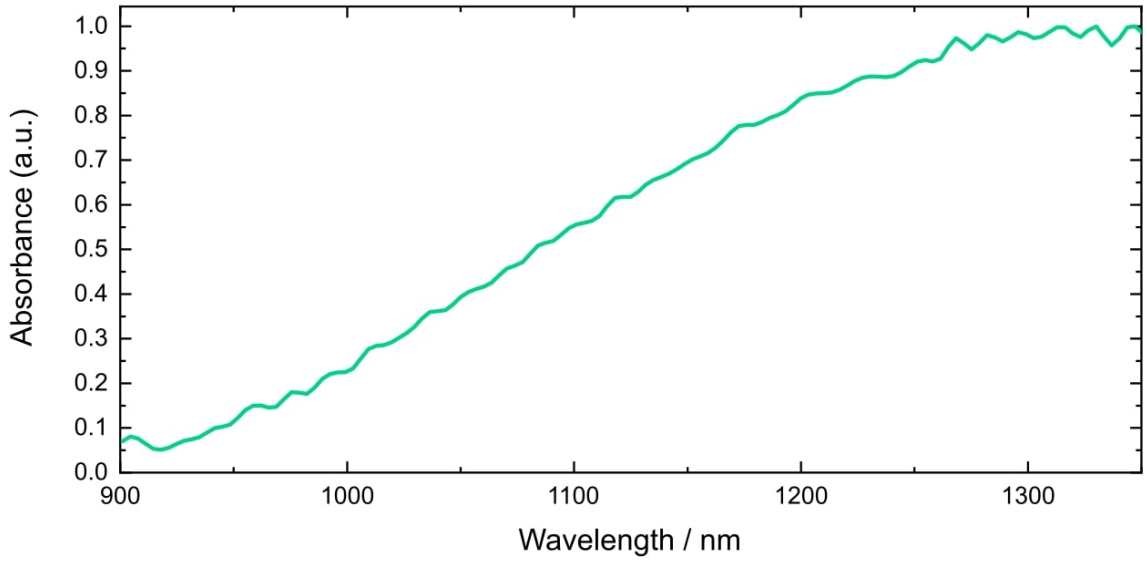


Figure A.1: Steady-state near-IR absorption spectrum of neat $PC_{70}BM$ film.

Appendix B

$AgBiS_2$ absorption

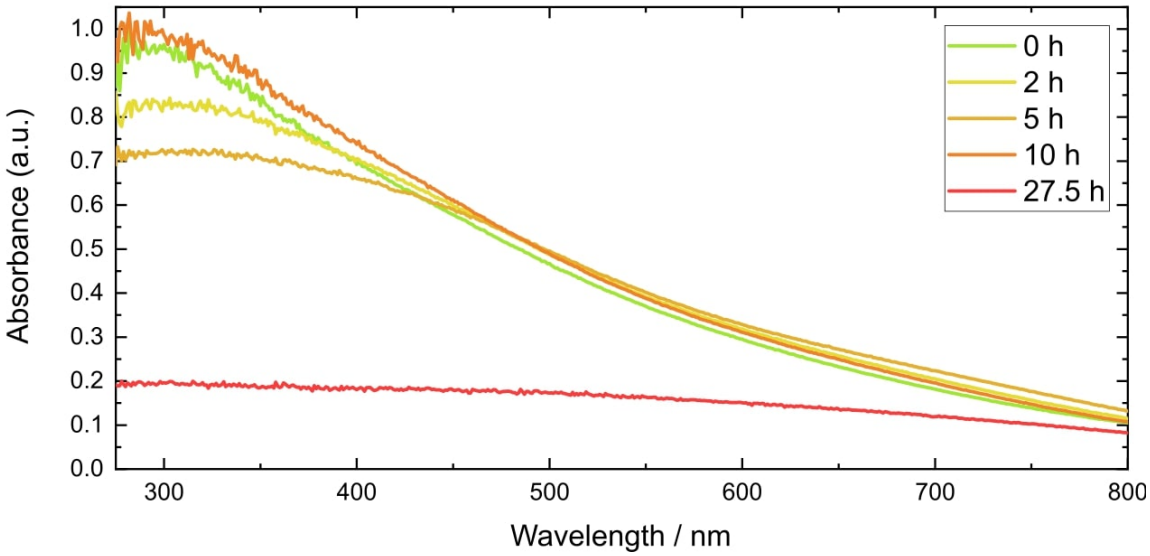


Figure B.1: Steady-state UV-visible absorption spectra of neat $AgBiS_2$ films at varying durations of exposure to light and O_2.

References

1. S. H. Mohr, J. Wang, G. Ellem, J. Ward, and D. Giurco. *Fuel*, 141:120–135, 2015.

2. J. L. Bamber, M. Oppenheimer, R. E. Kopp, W. P. Aspinall, and R. M. Cooke. *Proceedings of the National Academy of Sciences of the United States of America*, 116(23):11195–11200, 2019.

3. H. Ritchie and M. Roser. Energy, Nov 2020.

4. P. V. Kamat. Meeting the clean energy demand: Nanostructure architectures for solar energy conversion. *Journal of Physical Chemistry C*, 111(7):2834–2860, 2007.

5. N. M. Haegel et al. *Science*, 364(6443):836–+, 2019.

6. M. A. Green. *Physica E-Low-Dimensional Systems Nanostructures*, 14(1-2):11–17, 2002.

7. M. Piccolino. *Trends in Neurosciences*, 23(4):147–151, 2000.

8. C. Cramer. *Thomas Edison*. Greenhaven Press, 2001.

9. R. Chen, M. Wright, D. Chen, J. Yang, P. T. Zheng, X. Y. Zhang, S. Wenham, and A. Ciesla. *Progress in Photovoltaics*, 29(11):1213–1218, 2021.

10. D. M. Chapin, C. S. Fuller, and G. L. Pearson. *Journal of Applied Physics*, 25(5):676–677, 1954.

11. M. J. Y. Tayebjee, D. R. McCamey, and T. W. Schmidt. *Journal of Physical Chemistry Letters*, 6(12):2367–2378, 2015.

12. P. Busch, T. Heinonen, and P. Lahti. *Physics Reports-Review Section of Physics Letters*, 452(6):155–176, 2007.

13. P. W. Atkins. *Physical Chemistry*. Oxford University Press, 2014.

14. R. Hoffmann. *Angewandte Chemie*, 26(9):846–878, 1987.

15. M. Kasha. *Journal of the Chemical Society, Faraday Transactions*, 9:14–19, 1950.

16. P. Peumans, A. Yakimov, and S. R. Forrest. *Journal of Applied Physics*, 93(7):3693–3723, 2003.

17. C. J. Brabec, S. Gowrisanker, J. J. M. Halls, D. Laird, S. J. Jia, and S. P. Williams. *Advanced Materials*, 22(34):3839–3856, 2010.

18. S. Speiser. *Chemical Reviews*, 96(6):1953–1976, 1996.

19. O. V. Mikhnenko, P. W. M. Blom, and T. Q. Nguyen. Exciton diffusion in organic semiconductors. *Energy Environmental Science*, 8(7):1867–1888, 2015.

20. C. Deibel, T. Strobel, and V. Dyakonov. *Advanced Materials*, 22(37):4097–4111, 2010.

21. R. D. Pensack and J. B. Asbury. *Journal of the American Chemical Society*, 131(44):15986–+, 2009.

22. A. A. Bakulin, A. Rao, V. G. Pavelyev, P. H. M. van Loosdrecht, M. S. Pshenichnikov, D. Niedzialek, J. Cornil, D. Beljonne, and R. H. Friend. *Science*, 335(6074):1340–1344, 2012.

23. D. Caruso and A. Troisi. *Abstracts of Papers of the American Chemical Society*, 243, 2012.

24. T. M. Clarke and J. R. Durrant. *Chemical Reviews*, 110(11):6736–6767, 2010.

25. G. G. Macfarlane, T. P. McLean, J. E. Quarrington, and V. Roberts. *Physical Review*, 111(5):1245–1254, 1958.

26. P. K. Nayak. *Synthetic Metals*, 174:42–45, 2013.

27. A. Dkhissi. *Synthetic Metals*, 161(13-14):1441–1443, 2011.

28. J. L. Bredas, J. Cornil, and A. J. Heeger. *Advanced Materials*, 8(5):447–, 1996.

29. A. Zhugayevych, O. Postupna, R. C. Bakus, G. C. Welch, G. C. Bazan, and S. Tretiak. *Journal of Physical Chemistry C*, 117(10):4920–4930, 2013.

30. H. Kuang, M. J. Janik, and E. D. Gomez. *Journal of Polymer Science Part B-Polymer Physics*, 53(17):1224–1230, 2015.

31. C. Leng, H. M. Qin, Y. B. Si, and Y. Zhao. *Journal of Physical Chemistry C*, 118(4):1843–1855, 2014.

32. D. Beljonne, A. J. Ye, Z. Shuai, and J. L. Bredas. *Advanced Functional Materials*, 14(7):684–692, 2004.

33. J. L. Bredas, D. Beljonne, J. Cornil, J. P. Calbert, Z. Shuai, and R. Silbey. *Synthetic Metals*, 125(1):107–116, 2001.

34. A. Petrella, J. Cremer, L. De Cola, P. Bauerle, and R. M. Williams. *Journal of Physical Chemistry A*, 109(51):11687–11695, 2005.

35. Z. G. Shuai, W. T. Li, J. J. Ren, Y. Q. Jiang, and H. Geng. *Journal of Chemical Physics*, 153(8), 2020.

36. T. Liu and A. Troisi. *Journal of Physical Chemistry C*, 115(5):2406–2415, 2011.

37. K. M. Pelzer and S. B. Darlin. *Molecular Systems Design Engineering*, 1(1):10–24, 2016.

38. B. M. Savoie, A. Rao, A. A. Bakulin, S. Gelinas, B. Movaghar, R. H. Friend, T. J. Marks, and M. A. Ratner. *Journal of the American Chemical Society*, 136(7):2876–2884, 2014.

39. V. D. Mihailetchi, L. J. A. Koster, P. W. M. Blom, C. Melzer, B. de Boer, J. K. J. van Duren, and R. A. J. Janssen. *Advanced Functional Materials*, 15(5):795–801, 2005.

40. L. J. A. Koster, E. C. P. Smits, V. D. Mihailetchi, and P. W. M. Blom. *Physical Review B*, 72(8), 2005.

41. V. D. Mihailetchi, L. J. A. Koster, J. C. Hummelen, and P. W. M. Blom. *Physical Review Letters*, 93(21), 2004.

42. V. D. Mihailetchi, L. J. A. Koster, and P. W. M. Blom. *Applied Physics Letters*, 85(6):970–972, 2004.

43. G. A. Buxton and N. Clarke. *Physical Review B*, 74(8), 2006.

44. L. Onsager. *Physical Review*, 54(8):554–557, 1938.

45. C. L. Braun. *Journal of Chemical Physics*, 80(9):4157–4161, 1984.

46. M. Tachiya. *Journal of Chemical Physics*, 89(11):6929–6935, 1988.

47. P. M. Borsenberger and A. I. Ateya. *Journal of Applied Physics*, 50(2):909–913, 1979.

48. K. M. Hong and J. Noolandi. *Journal of Chemical Physics*, 69(11):5026–5039, 1978.

49. J. Singh and H. Baessler. *Physica Status Solidi B-Basic Research*, 63(1):425–430, 1974.

50. Y. C. Zhou, L. Wang, H. Zhang, Y. Y. Bai, Y. J. Niu, and H. Wang. *Applied Physics Letters*, 101(1), 2012.

51. S. Kraner, R. Scholz, C. Koerner, and K. Leo. *Journal of Physical Chemistry C*, 119(40):22820–22825, 2015.

52. S. Torabi, F. Jahani, I. Van Severen, C. Kanimozhi, S. Patil, R. W. A. Havenith, R. C. Chiechi, L. Lutsen, D. J. M. Vanderzande, T. J. Cleij, J. C. Hummelen, and L. J. A. Koster. *Advanced Functional Materials*, 25(1):150–157, 2015.

53. N. Cho, C. W. Schlenker, K. M. Knesting, P. Koelsch, H. L. Yip, D. S. Ginger, and A. K. Y. Jen. *Advanced Energy Materials*, 4(10), 2014.

54. M. Wojcik and M. Tachiya. *Radiation Physics and Chemistry*, 74(3-4):132–138, 2005.

55. S. Athanasopoulos, J. Kirkpatrick, D. Martinez, J. M. Frost, C. M. Foden, A. B. Walker, and J. Nelson. *Nano Letters*, 7(6):1785–1788, 2007.

56. W. I. Jeong, Y. E. Lee, H. S. Shim, T. M. Kim, S. Y. Kim, and J. J. Kim. *Advanced Functional Materials*, 22(14):3089–3094, 2012.

57. S. Fratini, M. Nikolka, A. Salleo, G. Schweicher, and H. Sirringhaus. Charge transport in high-mobility conjugated polymers and molecular semiconductors. *Nature Materials*, 19(5):491–502, 2020.

58. M. Nikolka, K. Broch, J. Armitage, D. Hanifi, P. J. Nowack, D. Venkateshvaran, A. Sadhanala, J. Saska, M. Mascal, S. H. Jung, J. K. Lee, I. McCulloch, A. Salleo, and H. Sirringhaus. High-mobility, trap-free charge transport in conjugated polymer diodes. *Nature Communications*, 10, 2019.

59. M. F. Xiao, R. L. Carey, H. Chen, X. C. Jiao, V. Lemaur, S. Schott, M. Nikolka, C. Jellett, A. Sadhanala, S. Rogers, S. P. Senanayak, A. Onwubiko, S. Y. Han, Z. L. Zhang, M. Abdi-Jalebi, Y. C. Zhang, T. H. Thomas, N. Mahmoudi, L. L. Lai, E. Selezneva, X. L. Ren, M. Nguyen, Q. J. Wang, I. Jacobs, W. Yue, C. R. McNeill, G. M. Liu, D. Beljonne, I. McCulloch, and H. Sirringhaus. Charge transport physics of a unique class of rigid-rod conjugated polymers with fused-ring conjugated units linked by double carbon-carbon bonds. *Science Advances*, 7(18), 2021.

60. D. Venkateshvaran, M. Nikolka, A. Sadhanala, V. Lemaur, M. Zelazny, M. Kepa, M. Hurhangee, A. J. Kronemeijer, V. Pecunia, I. Nasrallah, I. Romanov, K. Broch, I. McCulloch, D. Emin, Y. Olivier, J. Cornil, D. Beljonne, and H. Sirringhaus. Approaching disorder-free transport in high-mobility conjugated polymers. *Nature*, 515(7527):384–388, 2014.

61. P. Yin, Z. G. Yin, Y. L. Ma, and Q. D. Zheng. *Energy Environmental Science*, 13(12):5177–5185, 2020.

62. C. Labanti, M. Sung, J. Luke, S. Kwon, R. Kumar, J. Hong, J. Kim, A. A. Bakulin, and Y-H. Kwon, S-K.and Kim. *ACS Nano*, 15(4):7700–7712, 2021.

63. S. M. Menke, N. A. Ran, G. C. Bazan, and R. H. Friend. *Joule*, 2(1):25–35, 2018.

64. J. Wang, J. Zhang, Y. Z. Zhou, H. B. Liu, Q. F. Xue, X. S. Li, C. C. Chueh, H. L. Yip, Z. L. Zhu, and A. K. Y. Jen. *Nature Communications*, 11(1), 2020.

65. X. Liu, X. Y. Du, J. Y. Wang, C. H. Duan, X. F. Tang, T. Heumueller, G. G. Liu, Y. Li, Z. H. Wang, J. Wang, F. Liu, N. Li, C. J. Brabec, F. Huang, and Y. Cao. *Advanced Energy Materials*, 8(26), 2018.

66. R. Wang, J. Q. Xu, L. L. Fu, C. F. Zhang, Q. Li, J. Yao, X. J. Li, C. K. Sun, Z. G. Zhang, X. Y. Wang, Y. F. Li, J. Ma, and M. Xiao. *Journal of the American Chemical Society*, 143(11):4359–4366, 2021.

67. H. T. Fu, Y. M. Wang, D. Meng, Z. T. Ma, Y. Li, F. Gao, Z. H. Wang, and Y. M. Sun. *Acs Energy Letters*, 3(11):2729–2735, 2018.

68. F. D. Eisner, M. Azzouzi, Z. P. Fei, X. Y. Hou, T. D. Anthopoulos, T. J. S. Dennis, M. Heeney, and J. Nelson. *Journal of the American Chemical Society*, 141(15):6362–6374, 2019.

69. W. Gao, H. T. Fu, Y. X. Li, F. Lin, R. Sun, Z. Wu, X. Wu, C. Zhong, J. Min, J. D. Luo, H. Y. Woo, Z. L. Zhu, and A. K. Y. Jen. *Advanced Energy Materials*, 11(4), 2021.

70. Y. P. Xie, T. F. Li, J. Guo, P. Q. Bi, X. N. Xue, H. S. Ryu, Y. H. Cai, J. Min, L. J. Huo, X. T. Hao, H. Y. Woo, X. W. Zhan, and Y. M. Sun. *Acs Energy Letters*, 4(5):1196–1203, 2019.

71. Z. Xing, X. C. Meng, R. Sun, T. Hu, Z. Q. Huang, J. Min, X. T. Hu, and Y. W. Chen. *Advanced Functional Materials*, 30(21), 2020.

72. C. M. Proctor, M. Kuik, and T. Q. Nguyen. *Progress in Polymer Science*, 38(12):1941–1960, 2013.

73. H. J. Cha, J. Y. Wu, A. Wadsworth, J. Nagitta, S. Limbu, S. Pont, Z. Li, J. Searle, M. F. Wyatt, D. Baran, J. S. Kim, I. McCulloch, and J. R. Durrant. *Advanced Materials*, 29(33), 2017.

74. H. Cha, C. H. Tan, J. Y. Wu, Y. F. Dong, W. M. Zhang, H. Chen, S. Rajaram, K. S. Narayan, I. McCulloch, and J. R. Durrant. *Advanced Energy Materials*, 8(32), 2018.

75. C. M. Proctor, S. Albrecht, M. Kuik, D. Neher, and T. Q. Nguyen. *Advanced Energy Materials*, 4(10), 2014.

76. Z. C. Zhou, W. R. Liu, G. Q. Zhou, M. Zhang, D. P. Qian, J. Y. Zhang, S. S. Chen, S. J. Xu, C. D. Yang, F. Gao, H. M. Zhu, F. Liu, and X. Z. Zhu. *Advanced Materials*, 32(4), 2020.

77. H. Cha, S. Wheeler, S. Holliday, S. D. Dimitrov, A. Wadsworth, H. H. Lee, D. Baran, I. McCulloch, and J. R. Durrant. *Advanced Functional Materials*, 28(3), 2018.

78. W. Shockley and W. T. Read. *Physical Review*, 87(5):835–842, 1952.

79. K. D. Rosenthal, M. P. Hughes, B. R. Luginbuhl, N. A. Ran, A. Karki, S. J. Ko, H. Hu, M. Wang, H. Ade, and T. Q. Nguyen. *Advanced Energy Materials*, 9(27), 2019.

80. J. H. Schon, C. Kloc, E. Bucher, and B. Batiogg. *Nature*, 403(6768):408–410, 2000.

81. D. A. Neamen. *Semiconductor physics and devices: Basic principles*. McGraw-Hill, 2012.

82. H. F. Haneef, A. M. Zeidell, and O. D. Jurchescu. *Journal of Materials Chemistry C*, 8(3):759–787, 2020.

83. N. Ahn, K. Kwak, M. S. Jang, H. Yoon, B. Y. Lee, J. K. Lee, P. V. Pikhitsa, J. Byun, and M. Choi. *Nature Communications*, 7, 2016.

84. W. Nie, J. C. Blancon, A. J. Neukirch, K. Appavoo, H. Tsai, M. Chhowalla, M. A. Alam, M. Y. Sfeir, C. Katan, J. Even, S. Tretiak, J. J. Crochet, G. Gupta, and A. D. Mohite. *Nature Communications*, 7, 2016.

85. Q. Q. Gan, F. J. Bartoli, and Z. H. Kafafi. *Advanced Materials*, 25(17):2385–2396, 2013.

86. L. T. Dou, J. B. You, Z. R. Hong, Z. Xu, G. Li, R. A. Street, and Y. Yang. *Advanced Materials*, 25(46):6642–6671, 2013.

87. M. Kaltenbrunner, M. S. White, E. D. Glowacki, T. Sekitani, T. Someya, N. S. Sariciftci, and S. Bauer. *Nature Communications*, 3, 2012.

88. L. E. Brus. *The Journal of Chemical Physics*, 80(9):4403–4409, 1984.

89. A. L. Efros and A. L. Efros. Interband absorption of light in a semiconductor sphere. *Soviet Physics Semiconductors-Ussr*, 16(7):772–775, 1982.

90. J. Y. Yuan, A. Hazarika, Q. Zhao, X. F. Ling, T. Moot, W. L. Ma, and J. M. Luther. *Joule*, 4(6):1160–1185, 2020.

91. A. Pochettino. *Acad. Lincei Rend*, 15:355, 1906.

92. P. M. Borsenberger and D.S. Weiss. *Organic photoreceptors for Imaging Systems*. Dekker, 1993.

93. H. Sun, F. Chen, and Z. K. Chen. *Materials Today*, 24:94–118, 2019.

94. H. Spanggaard and F. C. Krebs. *Solar Energy Materials and Solar Cells*, 83(2-3):125–146, 2004.

95. C. W. Tang. *Applied Physics Letters*, 48(2):183–185, 1986.

96. H. Y. Mao, B. Xu, and S. Holdcroft. *Macromolecules*, 26(5):1163–1169, 1993.

97. W. Li, J. L. Cai, F. L. Cai, Y. Yan, H. N. Yi, R. S. Gurney, D. Liu, A. Iraqi, and T. Wang. Achieving over 11 % power conversion efficiency in pffbt4t-2od-based ternary polymer solar cells with enhanced open-circuit-voltage and suppressed charge recombination. *Nano Energy*, 44:155–163, 2018.

98. Z. Zheng, H. F. Yao, L. Ye, Y. Xu, S. Q. Zhang, and J. H. Hou. *Materials Today*, 35:115–130, 2020.

99. N. S. Sariciftci, L. Smilowitz, A. J. Heeger, and F. Wudl. *Science*, 258(5087):1474–1476, 1992.

100. Y. Lin and X. Zhan. *Materials Horizons*, 1(5):470, 2014.

101. A. Wadsworth, M. Moser, A. Marks, M. S. Little, N. Gasparini, C. J. Brabec, D. Baran, and I. Mcculloch. *Chemical Society Reviews*, 48(6):1596–1625, 2019.

102. N. Li, I. McCulloch, and C. J. Brabec. *Energy Environmental Science*, 11(6):1355–1361, 2018.

103. M. Lenes, G. J. A. H. Wetzelaer, F. B. Kooistra, S. C. Veenstra, J. C. Hummelen, and P. W. M. Blom. *Advanced Materials*, 20(11):2116–+, 2008.

104. F. B. Kooistra, J. Knol, F. Kastenberg, L. M. Popescu, W. J. H. Verhees, J. M. Kroon, and J. C. Hummelen. *Organic Letters*, 9(4):551–554, 2007.

105. C. Z. Li, S. C. Chien, H. L. Yip, C. C. Chueh, F. C. Chen, Y. Matsuo, E. Nakamura, and A. K. Y. Jen. *Chemical Communications*, 47(36):10082–10084, 2011.

106. H. M. Ko, H. Choi, S. Paek, K. Kim, K. Song, J. K. Lee, and J. Ko. Molecular engineering of push-pull chromophore for efficient bulk-heterojunction morphology in solution processed small molecule organic photovoltaics. *Journal of Materials Chemistry*, 21(20):7248–7253, 2011.

107. P. Meredith, W. Li, and A. Armin. *Advanced Energy Materials*, 10(33), 2020.

108. J. Li, Y. Q. Zhang, J. Yuan, C. Zhu, H. J. Peng, and Y. P. Zou. Fine-tuning of non-fullerene acceptor gives over 14 % efficiency for organic solar cells. *Dyes and Pigments*, 181, 2020.

109. W. C. Zhao, S. S. Li, H. F. Yao, S. Q. Zhang, Y. Zhang, B. Yang, and J. H. Hou. *Journal of the American Chemical Society*, 139(21):7148–7151, 2017.

110. Q. S. Liu, Y. F. Jiang, K. Jin, J. Q. Qin, J. G. Xu, W. T. Li, J. Xiong, J. F. Liu, Z. Xiao, K. Sun, S. F. Yang, X. T. Zhang, and L. M. Ding. *Science Bulletin*, 65(4):272–275, 2020.

111. D. R. Whang and D. H. Apaydin. *Chemphotochem*, 2(3):148–160, 2018.

112. *Science*, 323(5919):1286–1287, 2009.

113. P. Sanchez-Baracaldo and T. Cardona. *New Phytologist*, 225(4):1440–1446, 2020.

114. L. Behrendt, E. L. Trampe, N. B. Nord, J. Nguyen, M. Kuhl, D. Lonco, A. Nyarko, A. Dhinojwala, O. S. Hershey, and H. Barton. *Environmental Microbiology*, 22(3):952–963, 2020.

115. R. J. Sension. *Nature*, 446(7137):740–741, 2007.

116. M. M. Najafpour, I. Zaharieva, Z. Zand, S. M. Hosseini, M. Kouzmanova, M. Holynska, I. Tranca, A. W. Larkum, J. R. Shen, and S. I. Allakhverdiev. *Coordination Chemistry Reviews*, 409, 2020.

117. M. Kato, J. Z. Zhang, N. Paul, and E. Reisner. *Chemical Society Reviews*, 43(18):6485–6497, 2014.

118. K. N. Ferreira, T. M. Iverson, K. Maghlaoui, J. Barber, and S. Iwata. *Science*, 303(5665):1831–1838, 2004.

119. S. Y. Zhen and B. Bugbee. *Plant Cell and Environment*, 43(5):1259–1272, 2020.

120. G. Ananyev and G. C. Dismukes. *Photosynthesis Research*, 84(1-3):355–365, 2005.

121. Y. J. Xiao, Y. Qian, A. Q. Chen, T. Qin, F. Zhang, H. H. Tang, Z. T. Qiu, and B. L. Lin. *Journal of Materials Chemistry A*, 8(35):18310–18317, 2020.

122. J. Tschortner, B. Lai, and J. O. Kromer. *Frontiers in Microbiology*, 10, 2019.

123. J. Barber. *Chemical Society Reviews*, 38(1):185–196, 2009.

124. J. Barber and P. D. Tran. *Journal of the Royal Society Interface*, 10(81), 2013.

125. D. R. Lovley. *Annual Review of Microbiology, Vol 66*, 66:391–409, 2012.

126. K. H. Nealson and S. E. Finkel. *Mrs Bulletin*, 36(5):380–384, 2011.

127. J. A. Gralnick and D. K. Newman. *Molecular Microbiology*, 65(1):1–11, 2007.

128. S. H. Lee, K. S. Lee, S. Sorcar, A. Razzaq, C. A. Grimes, and S. I. In. *Journal of Photochemistry and Photobiology a-Chemistry*, 358:432–440, 2018.

129. R. W. Bradley, P. Bombelli, S. J. L. Rowden, and C. J. Howe. *Biochemical Society Transactions*, 40:1302–1307, 2012.

130. L. T. Wey, P. Bombelli, X. L. Chen, J. M. Lawrence, C. M. Rabideau, S. J. L. Rowden, J. Z. Zhang, and C. J. Howe. *Chemelectrochem*, 6(21):5375–5386, 2019.

131. O. Yehezkeli, R. Tel-Vered, J. Wasserman, A. Trifonov, D. Michaeli, R. Nechushtai, and I. Willner. *Nature Communications*, 3, 2012.

132. K. Tanaka, R. Tamamushi, and T. Ogawa. *Journal of Chemical Technology and Biotechnology B-Biotechnology*, 35(3):191–197, 1985.

133. T. Yagishita, T. Horigome, and K. Tanaka. *Journal of Chemical Technology and Biotechnology*, 56(4):393–399, 1993.

134. K. L. Saar, P. Bombelli, D. J. Lea-Smith, T. Call, E. M. Aro, T. Muller, C. J. Howe, and T. P. J. Knowles. *Nature Energy*, 3(1):75–81, 2018.

135. S. J. Rowden, P. Bombelli, and C. J. Howe. *Methods in Molecular Biology*, 1770:335–346, 2018.

136. B. E. Logan, B. Hamelers, R. A. Rozendal, U. Schrorder, J. Keller, S. Freguia, P. Aelterman, W. Verstraete, and K. Rabaey. *Environmental Science Technology*, 40(17):5181–5192, 2006.

137. P. Bombelli, M. Zarrouati, R. J. Thorne, K. Schneider, S. J. L. Rowden, A. Ali, K. Yunus, P. J. Cameron, A. C. Fisher, D. I. Wilson, C. J. Howe, and A. J. McCormick. *Physical Chemistry Chemical Physics*, 14(35):12221–12229, 2012.

138. P. Bateson, J. E. H. Fleet, A. S. Riseley, E. Janeva, A. S. Marcella, C. Farinea, M. Kuptsova, N. C. Pueyo, C. J. Howe, P. Bombelli, and B. M. Parker. *Biology-Basel*, 7(2), 2018.

139. J. Chouler, M. D. Monti, W. J. Morgan, P. J. Cameron, and M. Di Lorenzo. *Electrochimica Acta*, 309:392–401, 2019.

140. R. G. Compton and C. E. Banks. *Understanding voltammetry*. World Scientific, 2018.

141. C. Leger and P. Bertrand. *Chemical Reviews*, 108(7):2379–2438, 2008.

142. A. Cereda, A. Hitchcock, M. D. Symes, L. Cronin, T. S. Bibby, and A. K. Jones. *Plos One*, 9(3), 2014.

143. A. C. Gonzalez-Aravena, K. Yunus, L. Zhang, B. Norling, and A. C. Fisher. *Rsc Advances*, 8(36):20263–20274, 2018.

144. J. Z. Zhang, P. Bombelli, K. P. Sokol, A. Fantuzzi, A. W. Rutherford, C. J. Howe, and E. Reisner. *Journal of the American Chemical Society*, 140(1):6–9, 2018.

145. C. G. Granqvist and A. Hultaker. *Thin Solid Films*, 411(1):1–5, 2002.

146. K. Schneider, R. J. Thorne, and P. J. Cameron. *Philosophical Transactions of the Royal Society a-Mathematical Physical and Engineering Sciences*, 374(2061), 2016.

147. R. Thorne, H. N. Hu, K. Schneider, P. Bombelli, A. Fisher, L. M. Peter, A. Dent, and P. J. Cameron. *Journal of Materials Chemistry*, 21(44):18055–18060, 2011.

148. A. J. McCormick, P. Bombelli, A. M. Scott, A. J. Philips, A. G. Smith, A. C. Fisher, and C. J. Howe. *Energy Environmental Science*, 4(11):4699–4709, 2011.

149. K. Rabaey and R. A. Rozendal. *Nature Reviews Microbiology*, 8(10):706–716, 2010.

150. F. Harnisch, L. F. M. Rosa, F. Kracke, B. Virdis, and J. O. Kromer. *Chemsuschem*, 8(5):758–766, 2015.

151. F. Kracke, B. Lai, S. Q. Yu, and J. O. Kromer. *Metabolic Engineering*, 45:109–120, 2018.

152. J. M. Pisciotta, Y. Zou, and I. V. Baskakov. *Plos One*, 5(5), 2010.

153. L. Darus, Y. Lu, P. Ledezma, J. Keller, and S. Freguia. *Bioresource Technology*, 195:248–253, 2015.

154. Y. Yuan, Q. Chen, S. G. Zhou, L. Zhuang, and P. Hu. *Journal of Hazardous Materials*, 187(1-3):591–595, 2011.

155. K. S. Madiraju, D. Lyew, R. Kok, and V. Raghavan. *Bioresource Technology*, 110:214–218, 2012.

156. N. Sekar, Y. Umasankar, and R. P. Ramasamy. *Physical Chemistry Chemical Physics*, 16(17):7862–7871, 2014.

157. S. Kaushik, M. K. Sarma, and P. Goswami. *Journal of Materials Chemistry A*, 5(17):7885–7895, 2017.

158. G. Longatte, F. Rappaport, F. A. Wollman, M. Guille-Collignon, and F. Lemaitre. *Electrochimica Acta*, 236:327–332, 2017.

159. A. J. McCormick, P. Bombelli, R. W. Bradley, R. Thorne, T. Wenzele, and C. J. Howe. *Energy Environmental Science*, 8(5):1627–1627, 2015.

160. S. Yoon, H. Lee, A. Fraiwan, C. H. Dai, and S. Choi. *2014 9th Ieee International Conference on Nano/Micro Engineered and Molecular Systems (Nems)*, pages 265–268, 2014.

161. H. Ochiai, H. Shibata, Y. Sawa, M. Shoga, and S. Ohta. *Applied Biochemistry and Biotechnology*, 8(4):289–303, 1983.

162. R. Vasudevan, G. A. R. Gale, A. A. Schiavon, A. Puzorjov, J. Malin, M. D. Gillespie, K. Vavitsas, V. Zulkower, B. J. Wang, C. J. Howe, D. J. Lea-Smith, and A. J. McCormick. *Plant Physiology*, 180(1):39–55, 2019.

163. Pinhassi et al. *Plos One*, 10(4), 2015.

164. K. Hasan, R. D. Milton, M. Grattieri, T. Wang, M. Stephanz, and S. D. Minteer. *Acs Catalysis*, 7(4):2257–2265, 2017.

165. T. Kothe, S. Poller, F. Y. Zhao, P. Fortgang, M. Rogner, W. Schuhmann, and N. Plumere. *Chemistry-a European Journal*, 20(35):11029–11034, 2014.

166. K. P. Sokol, W. E. Robinson, J. Warnan, N. Kornienko, M. M. Nowaczyk, A. Ruff, J. Z. Zhang, and E. Reisner. *Nature Energy*, 3(11):944–951, 2018.

167. D. Mersch, C. Y. Lee, J. Z. Zhang, K. Brinkert, J. C. Fontecilla-Camps, A. W. Rutherford, and E. Reisner. *Journal of the American Chemical Society*, 137(26):8541–8549, 2015.

168. Y. H. Xu, A. Fischer, L. L. Duan, L. P. Tong, E. Gabrielsson, B. Akermark, and L. C. Sun. *Angewandte Chemie-International Edition*, 49(47):8934–8937, 2010.

169. C. Duan, F. Huang, and Y. Cao. *Journal of Materials Chemistry*, 22(21):10416, 2012.

170. J. S. Kanady, E. Y. Tsui, M. W. Day, and T. Agapie. *Science*, 333(6043):733–736, 2011.

171. Q. S. Yin, J. M. Tan, C. Besson, Y. V. Geletii, D. G. Musaev, A. E. Kuznetsov, Z. Luo, K. I. Hardcastle, and C. L. Hill. *Science*, 328(5976):342–345, 2010.

172. S. Y. Reece, J. A. Hamel, K. Sung, T. D. Jarvi, A. J. Esswein, J. J. H. Pijpers, and D. G. Nocera. *Science*, 334(6056):645–648, 2011.

173. M. Dinca, Y. Surendranath, and D. G. Nocera. *Proceedings of the National Academy of Sciences of the United States of America*, 107(23):10337–10341, 2010.

174. T. Wenzel, D. Hartter, P. Bombelli, C. J. Howe, and U. Steiner. 9, 2018.

175. E. Romero, V. I. Novoderezhkin, and R. van Grondelle. *Nature*, 543(7645):355–365, 2017.

176. J. J. Shiang, L. M. Yoder, and R. J. Sension. *Journal of Physical Chemistry B*, 107(9):2162–2169, 2003.

177. L. M. Yoder, A. G. Cole, and R. J. Sension. *Photosynthesis Research*, 72(2):147–158, 2002.

178. T. Brixner, J. Stenger, H. M. Vaswani, M. Cho, R. E. Blankenship, and G. R. Fleming. *Nature*, 434(7033):625–628, 2005.

179. J. Myers. *Photosynthesis Research*, 40(3):303–310, 1994.

180. R. van Grondelle and H. van Gorkom. *Photosynthesis Research*, 120(1-2):3–7, 2014.

181. A. Zouni, H. T. Witt, J. Kern, P. Fromme, N. Krauss, W. Saenger, and P. Orth. *Nature*, 409(6821):739–743, 2001.

182. Y. Umena, K. Kawakami, J. R. Shen, and N. Kamiya. *Nature*, 473(7345):55–U65, 2011.

183. G. D. Scholes, G. R. Fleming, A. Olaya-Castro, and R. van Grondelle. *Nature Chemistry*, 3(10):763–774, 2011.

184. R. van Grondelle, H. van Amerongen, and S. Valkuna. *Photosynthetic excitons*. World Scientific, 2000.

185. J. Frenkel. *Physical Review*, 37(10):1276–1294, 1931.

186. J. R. Durrant, G. Hastings, D. M. Joseph, J. Barber, G. Porter, and D. R. Klug. *Proceedings of the National Academy of Sciences of the United States of America*, 89(23):11632–11636, 1992.

187. A. Y. Shkuropatov, R. A. Khatypov, V. A. Shkuropatova, M. G. Zvereva, T. G. Owens, and V. A. Shuvalov. *Febs Letters*, 450(1-2):163–167, 1999.

188. F. Vacha, D. M. Joseph, J. R. Durrant, A. Telfer, D. R. Klug, G. Porter, and J. Barber. *Proceedings of the National Academy of Sciences of the United States of America*, 92(7):2929–2933, 1995.

189. B. A. Diner, E. Schlodder, P. J. Nixon, W. J. Coleman, F. Rappaport, J. Lavergne, W. F. J. Vermaas, and D. A. Chisholm. *Biochemistry*, 40(31):9265–9281, 2001.

190. V. I. Novoderezhkin, E. Romero, J. P. Dekker, and R. van Grondelle. *Chemphyschem*, 12(3):681–688, 2011.

191. E. Romero, I. H. van Stokkum, V. I. Novoderezhkin, J. P. Dekker, and R. van Grondelle. *Biochemistry*, 49(20):4300–4307, 2010.

192. J. C. Wright. *International Reviews in Physical Chemistry*, 21(2):185–255, 2002.

193. S. Mukamel. *Annual Review of Physical Chemistry*, 51:691–729, 2000.

194. D. B. Turner, R. Dinshaw, K. K. Lee, M. S. Belsley, K. E. Wilk, P. M. G. Curmi, and G. D. Scholes. *Physical Chemistry Chemical Physics*, 14(14):4857–4874, 2012.

195. K. L. M. Lewis and J. P. Ogilvie. *Journal of Physical Chemistry Letters*, 3(4):503–510, 2012.

196. Y. C. Cheng and G. R. Fleming. *Annual Review of Physical Chemistry*, 60:241–262, 2009.

197. D. Zigmantas, E. L. Read, T. Mancal, T. Brixner, A. T. Gardiner, R. J. Cogdell, and G. R. Fleming. *Proceedings of the National Academy of Sciences of the United States of America*, 103(34):12672–12677, 2006.

198. S. Savikhin, D. R. Buck, and W. S. Struve. *Chemical Physics*, 223(2-3):303–312, 1997.

199. T. R. Calhoun, N. S. Ginsberg, G. S. Schlau-Cohen, Y. C. Cheng, M. Ballottari, R. Bassi, and G. R. Fleming. *Journal of Physical Chemistry B*, 113(51):16291–16295, 2009.

200. E. Collini, C. Y. Wong, K. E. Wilk, P. M. G. Curmi, P. Brumer, and G. D. Scholes. *Nature*, 463(7281):644–U69, 2010.

201. G. S. Schlau-Cohen, A. Ishizaki, T. R. Calhoun, N. S. Ginsberg, M. Ballottari, R. Bassi, and G. R. Fleming. *Nature Chemistry*, 4(5):389–395, 2012.

202. R. Hildner, D. Brinks, J. B. Nieder, R. J. Cogdell, and N. F. van Hulst. *Science*, 340(6139):1448–1451, 2013.

203. G. S. Engel, T. R. Calhoun, E. L. Read, T. K. Ahn, T. Mancal, Y. C. Cheng, R. E. Blankenship, and G. R. Fleming. *Nature*, 446(7137):782–786, 2007.

204. G. Panitchayangkoon, D. Hayes, K. A. Fransted, J. R. Caram, E. Harel, J. Z. Wen, R. E. Blankenship, and G. S. Engel. *Proceedings of the National Academy of Sciences of the United States of America*, 107(29):12766–12770, 2010.

205. E. Collini and G. D. Scholes. *Science*, 323(5912):369–373, 2009.

206. F. Milota, V. I. Prokhorenko, T. Mancal, H. von Berlepsch, O. Bixner, H. F. Kauffmann, and J. Hauer. *Journal of Physical Chemistry A*, 117(29):6007–6014, 2013.

207. H. Lee, Y. C. Cheng, and G. R. Fleming. *Science*, 316(5830):1462–1465, 2007.

208. S. Westenhoff, D. Palecek, P. Edlund, P. Smith, and D. Zigniantas. *Journal of the American Chemical Society*, 134(40):16484–16487, 2012.

209. M. H. Vos, J. C. Lambry, S. J. Robles, D. C. Youvan, J. Breton, and J. L. Martin. *Proceedings of the National Academy of Sciences of the United States of America*, 88(20):8885–8889, 1991.

210. M. H. Vos, F. Rappaport, J. C. Lambry, J. Breton, and J. L. Martin. *Nature*, 363(6427):320–325, 1993.

211. F. D. Fuller, J. Pan, A. Gelzinis, V. Butkus, S. S. Senlik, D. E. Wilcox, C. F. Yocum, L. Valkunas, D. Abramavicius, and J. P. Ogilvie. *Nature Chemistry*, 6(8):706–711, 2014.

212. E. Romero, R. Augulis, V. I. Novoderezhkin, M. Ferretti, J. Thieme, D. Zigmantas, and R. van Grondelle. *Nature Physics*, 10(9):677–683, 2014.

213. Demtroder W. *Laser spectroscopy.* Springer, 2016.

214. T. R. Hopper, D. Qian, L. Yang, X. Wang, K. Zhou, R. Kumar, W. Ma, C. He, J. Hou, and F. Gao. *Chemistry of Materials*, 31(17):6860–6869, 2019.

215. A. Weu, R. Kumar, J. F. Butscher, V. Lami, F. Paulus, A. A. Bakulin, and Y. Yaynzof. *Advanced Functional Materials*, (5):1907432, 2019.

216. D. Becker-Koch, M. Albaladejo-Siguan, J. Kress, R. Kumar, Y. J. Hofstetter, Q. An, A. A. Bakulin, Paulus F., and Vaynzof Y. *Nanoscale*, 14:3020–3030, 2022.

217. M. Bernechea, N. C. Miller, G. Xercavins, D. So, A. Stavrinadis, and G. Konstantatos. *Nature Photonics*, 10(8):521–525, 2016.

218. D. Calloway. *Journal of Chemical Education*, 74:744, 1997.

219. X. Guo, Y. Luo, Y. Zhang, X. Huang, D. Li, and Q. Meng. *Review of Scientific Instruments*, 81(10):103106, 2010.

220. Y. Liang, T. Tsubota, L. P. Mooij, and R. van de Krol. *The Journal of Physical Chemistry C*, 115(35):17594–17598, 2011.

221. R. Berera, R. van Grondelle, and J. T. Kennis. *Photosynthesis Research*, 101(2-3):105–118, 2009.

222. S. Kim and S. Ma. *Steel and Composite Structures*, 7(6):421–440, 2007.

223. C. Ruckebusch, M. Sliwa, P. Pernot, A. de Juan, and R. Tauler. *Journal of Photochemistry and Photobiology C: Photochemistry Reviews*, 13(1):1–27, 2012.

224. M. Nurhuda, A. Suda, K. Midorikawa, and H. Budiono. *Journal of the Optical Society of America B*, 22(8):1757, 2005.

225. J. T. Bloking, T. Giovenzana, A. T. Higgs, A. J. Ponec, E. T. Hoke, K. Vandewal, S. Ko, Z. Bao, A. Sellinger, and M. D. Mcgehee. *Advanced Energy Materials*, 4(12):1301426, 2014.

226. R. S Gurney, D. G Lidzey, and T. Wang. *Reports on Progress in Physics*, 82(3):036601, 2019.

227. B. A. Collins, Z. Li, J. R. Tumbleston, E. Gann, C. R. Mcneill, and H. Ade. *Advanced Energy Materials*, 3(1):65–74, 2012.

228. W. Ma, J. R. Tumbleston, M. Wang, E. Gann, F. Huang, and H. Ade. *Advanced Energy Materials*, 3(7):864–872, 2013.

229. S. Mukherjee, C. M. Proctor, J. R. Tumbleston, G. C. Bazan, T. Nguyen, and H. Ade. *Advanced Materials*, 27(6):1105–1111, 2014.

230. S. Mukherjee, X. Jiao, and H. Ade. *Advanced Energy Materials*, 6(18):1600699, 2016.

231. A. C. Stuart, J. R. Tumbleston, H. Zhou, W. Li, S. Liu, H. Ade, and W. You. *Journal of the American Chemical Society*, 135(5):1806–1815, 2013.

232. J. Zhang, K. Jiang, G. Yang, T. Ma, J. Liu, Z. Li, J. Y. L. Lai, W. Ma, and H. Yan. *Advanced Energy Materials*, 7(15):1602119, 2017.

233. S. D. Dimitrov and J. R. Durrant. *Chemistry of Materials*, 26(1):616–630, 2013.

234. S. J. Jeon, Y. H. Kim, D. H. Hong, N. G. Yang, Y. W. Han, and D. K. Moon. *Solar RRL*, 5(3):2000608, 2021.

235. Y. Qin, M. A. Uddin, Y. Chen, B. Jang, K. Zhao, Z. Zheng, R. Yu, T. J. Shin, H. Y. Woo, and J. Hou. *Advanced Materials*, 28(42):9416–9422, 2016.

236. Y. Hsiao, Ch. Li, S. Chang, S. Heo, K. Tajima, Y. Cheng, and C. Hsu. *ACS Applied Materials Interfaces*, 9(48):42035–42042, 2017.

237. M. Li, W. Ni, X. Wan, Q. Zhang, B. Kan, and Y. Chen. *Journal of Materials Chemistry A*, 3(9):4765–4776, 2015.

238. W. Ni, X. Wan, M. Li, Y. Wang, and Y. Chen. *Chemical Communications*, 51(24):4936–4950, 2015.

239. Y. Li. *Science China Chemistry*, 58(2):191–191, 2015.

240. Y. Chen, X. Wan, and G. Long. *Accounts of Chemical Research*, 46(11):2645–2655, 2013.

241. H. Fan and X. Zhu. *Science China Chemistry*, 58(6):922–936, 2015.

242. Y. Liu, C. Chen, Z. Hong, J. Gao, Y. Yang, H. Zhou, L. Dou, G. Li, and Y. Yang. *Scientific Reports*, 3(1), 2013.

243. N. L. Janaki, B. Priyanka, Anup Thomas, and K. Bhanuprakash. *The Journal of Physical Chemistry C*, 116(43):22663–22674, 2012.

244. B. Mukherjee and M. Mukherjee. *ACS Omega*, 2(12):9181–9190, 2017.

245. B. Priyanka, V. Anusha, and K. Bhanuprakash. *The Journal of Physical Chemistry C*, 119(22):12251–12261, 2015.

246. C. Zhao, Q. Zhang, X. Yu, K. Zhou, L. Jin, and W. Wang. *Molecular Physics*, 118(5), 2019.

247. S. Zhang, X. Wang, A. Tang, J. Huang, C. Zhan, and J. Yao. *Physical Chemistry Chemical Physics*, 16(10):4664, 2014.

248. H. Yao, L. Ye, H. Zhang, S. Li, S. Zhang, and J. Hou. *Chemical Reviews*, 116(12):7397–7457, 2016.

249. L. Huo and J. Hou. *Polymer Chemistry*, 2(11):2453, 2011.

250. L. Ye, S. Zhang, L. Huo, M. Zhang, and J. Hou. *Accounts of Chemical Research*, 47(5):1595–1603, 2014.

251. J. Hou, M. Park, S. Zhang, Y. Yao, L. Chen, J. Li, and Y. Yang. *Macromolecules*, 41(16):6012–6018, 2008.

252. Y. Liu, X. Wan, F. Wang, J. Zhou, G. Long, J. Tian, and Y. Chen. *Advanced Materials*, 23(45):5387–5391, 2011.

253. W. Ni, X. Li, M.and Wan, H. Feng, B. Kan, Y. Zuo, and Y. Chen. *RSC Adv.*, 4(60):31977–31980, 2014.

254. J. Zhou, X. Wan, Y. Liu, Y. Zuo, Z. Li, G. He, G. Long, W. Ni, C. Li, and X. Su. *Journal of the American Chemical Society*, 134(39):16345–16351, 2012.

255. M. Li, F. Liu, X. Wan, W. Ni, B. Kan, H. Feng, Q. Zhang, X. Yang, Y. Wang, and Y. Zhang. *Advanced Materials*, 27(40):6296–6302, 2015.

256. K. Sun, Z. Xiao, S. Lu, W. Zajaczkowski, W. Pisula, E. Hanssen, J. M. White, R. M. Williamson, J. Subbiah, and J. Ouyang. *Nature Communications*, 6(1), 2015.

257. D. Liu, L. Yang, Y. Wu, X. Wang, Y. Zeng, G. Han, H. Yao, S. Li, S. Zhang, and Y. Zhang. *Chemistry of Materials*, 30(3):619–628, 2018.

258. P. Cheng, G. Li, X. Zhan, and Y. Yang. *Nature Photonics*, 12(3):131–142, 2018.

259. Y. Lin, Z. Zhang, H. Bai, J. Wang, Y. Yao, Y. Li, D. Zhu, and X. Zhan. *Energy Environmental Science*, 8(2):610–616, 2015.

260. Y. Lin, J. Wang, Z. Zhang, H. Bai, Y. Li, D. Zhu, and X. Zhan. *Advanced Materials*, (7):1170–1174, 2015.

261. G. Forti, A. Nitti, P. Osw, G. Bianchi, R. Po, and D. Pasini. *International Journal of Molecular Sciences*, 21(21):8085, 2020.

262. Z. Zheng, O. M. Awartani, B. Gautam, D. Liu, Y. Qin, W. Li, A. Bataller, K. Gundogdu, H. Ade, and J. Hou. *Advanced Materials*, 29(5):1604241, 2016.

263. W. Zhao, D. Qian, S. Zhang, S. Li, O. Inganäs, F. Gao, and J. Hou. *Advanced Materials*, 28(23):4734–4739, 2016.

264. E. Fragoso, R. Azpiroz, P. Sharma, G. Espinosa-Perez, F. Lara-Ochoa, A. Toscano, R. Gutierrez, and O. Portillo. New organoselenium compounds with intramolecular se center dot center dot center dot o/se center dot center dot center dot h interactions: Nmr and theoretical studies. *Journal of Molecular Structure*, 1155:711–719, 2018.

265. A. J. Mukherjee, S. S. Zade, H. B. Singh, and R. B. Sunoj. Organoselenium chemistry: Role of intramolecular interactions. *Chemical Reviews*, 110(7):4357–4416, 2010.

266. A. Atkinson, A. D. Brewster, S. V. Ley, R. S. Osborn, D. Rogers, D. J. Williams, and K. A. Woode. X-ray evidence for partial bonding between sulfur or selenium and oxygen in thio-imines and seleno-imines. *Journal of the Chemical Society-Chemical Communications*, (9):325–326, 1977.

267. B. Azzopardi, C. J. M. Emmott, A. Urbina, F. C. Krebs, J. Mutale, and J. Nelson. *Energy Environmental Science*, 4(10):3741–3753, 2011.

268. W. R. Mateker and M. D. McGehee. *Advanced Materials*, 29(10), 2017.

269. C. H. Peters, I. T. Sachs-Quintana, J. P. Kastrop, S. Beaupre, M. Leclerc, and M. D. McGehee. *Advanced Energy Materials*, 1(4):491–494, 2011.

270. E. M. Speller, A. J. Clarke, J. Luke, H. K. H. Lee, J. R. Durrant, N. Li, T. Wang, H. C. Wong, J. S. Kim, W. C. Tsoi, and Z. Li. *Journal of Materials Chemistry A*, 7(41):23361–23377, 2019.

271. M. Corazza, F. C. Krebs, and S. A. Gevorgyan. *Solar Energy Materials and Solar Cells*, 143:467–472, 2015.

272. E. A. Katz, S. Gevorgyan, M. S. Orynbayev, and F. C. Krebs. *European Physical Journal-Applied Physics*, 36(3):307–311, 2006.

273. Y. W. Zhang, E. Bovill, J. Kingsley, A. R. Buckley, H. N. Yi, A. Iraqi, T. Wang, and D. G. Lidzey. *Scientific Reports*, 6, 2016.

274. Y. B. Lin, Y. Firdaus, F. H. Isikgor, M. I. Nugraha, E. Yengel, G. T. Harrison, R. Hallani, A. El-Labban, H. Faber, C. Ma, X. P. Zheng, A. Subbiah, C. T. Howells, O. M. Bakr, I. McCulloch, S. De Wolf, L. Tsetseris, and T. D. Anthopoulos. *Acs Energy Letters*, 5(9):2935–2944, 2020.

275. X. M. Xu, K. Fukuda, A. Karki, S. Park, H. Kimura, H. Jinno, N. Watanabe, S. Yamamoto, S. Shimomura, D. Kitazawa, T. Yokota, S. Umezu, T. Q. Nguyen, and T. Someya. *Proceedings of the National Academy of Sciences of the United States of America*, 115(18):4589–4594, 2018.

276. B. Roth, G. A. D. Benatto, M. Corazza, R. R. Sondergaard, S. A. Gevorgyan, M. Jorgensen, and F. C. Krebs. *Advanced Energy Materials*, 5(9), 2015.

277. Z. Jiang, F. J. Wang, K. Fukuda, A. Karki, W. Huang, K. Yu, T. Yokota, K. Tajima, T. Q. Nguyen, and T. Someya. *Proceedings of the National Academy of Sciences of the United States of America*, 117(12):6391–6397, 2020.

278. D. Chemisana, A. Moreno, M. Polo, C. Aranda, A. Riverola, E. Ortega, C. Lamnatou, A. Domenech, G. Blanco, and A. Cot. *Renewable Energy*, 137:177–188, 2019.

279. N. Grossiord, J. M. Kroon, R. Andriessen, and P. W. M. Blom. *Organic Electronics*, 13(3):432–456, 2012.

280. T. M. Clarke, C. Lungenschmied, J. Peet, N. Drolet, K. Sunahara, A. Furube, and A. J. Mozer. *Advanced Energy Materials*, 3(11):1473–1483, 2013.

281. Y. Wang, Z. M. Zhang, Y. J. Lan, Q. Song, M. Z. Li, and Y. L. Song. *Angewandte Chemie-International Edition*, 60(16):8673–8677, 2021.

282. R. D. Pensack, K. M. Banyas, and J. B. Asbury. *Journal of Physical Chemistry C*, 114(12):5344–5350, 2010.

283. J. Luke, E. M. Speller, A. Wadsworth, M. F. Wyatt, S. Dimitrov, H. K. H. Lee, Z. Li, W. C. Tsoi, I. McCulloch, D. Bagnis, J. R. Durrant, and J. S. Kim. Twist and degrade-impact of molecular structure on the photostability of nonfullerene acceptors and their photovoltaic blends. *Advanced Energy Materials*, 9(15), 2019.

284. P. R. Berger and M. Kim. *Journal of Renewable and Sustainable Energy*, 10(1), 2018.

285. T. Heumueller, W. R. Mateker, A. Distler, U. F. Fritze, R. Cheacharoen, W. H. Nguyen, M. Biele, M. Salvador, M. von Delius, H. J. Egelhaaf, M. D. McGehee, and C. J. Brabec. *Energy Environmental Science*, 9(1):247–256, 2016.

286. A. Distler, T. Sauermann, H. J. Egelhaaf, S. Rodman, D. Waller, K. S. Cheon, M. Lee, and D. M. Guldi. *Advanced Energy Materials*, 4(1), 2014.

287. Q. Burlingame, X. R. Tong, J. Hankett, M. Slootsky, Z. Chen, and S. R. Forrest. *Energy Environmental Science*, 8(3):1005–1010, 2015.

288. N. Li, J. D. Perea, T. Kassar, M. Richter, T. Heumueller, G. J. Matt, Y. Hou, N. S. Gueldal, H. W. Chen, S. Chen, S. Langner, M. Berlinghof, T. Unruh, and C. J. Brabec. *Nature Communications*, 8, 2017.

289. L. Duan, Y. Zhang, M. He, H. Deng, R.and Yi, Q. Wei, Y. Zou, and A. Uddin. *ACS Applied Materials amp; Interfaces*, 12(24):27433–27442, 2020.

290. S. Chambon, A. Rivaton, J. L. Gardette, and M. Firon. *Solar Energy Materials and Solar Cells*, 91(5):394–398, 2007.

291. S. Yamane, J. Mizukado, Y. Suzuki, M. Sakurai, L. Chen, and H. Suda. *Chemistry Letters*, 44(3):339–341, 2015.

292. Z. Xiao, J. Y. Yao, D. Z. Yang, F. D. Wang, S. H. Huang, L. B. Gan, Z. S. Jia, Z. P. Jiang, X. B. Yang, B. Zheng, G. Yuan, S. W. Zhang, and Z. M. Wang. *Journal of the American Chemical Society*, 129(51):16149–16162, 2007.

293. Y. C. Wang, M. J. Chang, B. Kan, X. J. Wan, C. X. Li, and Y. S. Chen. *Acs Applied Energy Materials*, 1(5):2150–2156, 2018.

294. H. K. H. Lee, A. M. Telford, J. A. Rohr, M. F. Wyatt, B. Rice, J. Y. Wu, A. D. Maciel, S. M. Tuladhar, E. Speller, J. McGettrick, J. R. Searle, S. Pont, T. Watson, T. Kirchartz, J. R. Durrant, W. C. Tsoi, J. Nelson, and Z. Li. *Energy Environmental Science*, 11(2):417–428, 2018.

295. K. Kawano, R. Pacios, D. Poplavskyy, J. Nelson, D. D. C. Bradley, and J. R. Durrant. *Solar Energy Materials and Solar Cells*, 90(20):3520–3530, 2006.

296. Z. Li, H. C. Wong, Z. G. Huang, H. L. Zhong, C. H. Tan, W. C. Tsoi, J. S. Kim, J. R. Durrant, and J. T. Cabral. *Nature Communications*, 4, 2013.

297. S. Wood, J. Wade, M. Shahid, E. Collado-Fregoso, D. D. Bradley, J. R. Durrant, M. Heeney, and J. Kim. *Energy amp; Environmental Science*, 8(11):3222–3232, 2015.

298. A. Weu, R. Kumar, J. F. Butscher, V. Lami, F. Paulus, A. A. Bakulin, and Y. Yaynzof. *Advanced Functional Materials*, 30(5), 2020.

299. B. Kan, M. M. Li, Q. Zhang, F. Liu, X. J. Wan, Y. C. Wang, W. Ni, G. K. Long, X. Yang, H. R. Feng, Y. Zuo, M. T. Zhang, F. Huang, Y. Cao, T. P. Russell, and Y. S. Chen. *Journal of the American Chemical Society*, 137(11):3886–3893, 2015.

300. Y. M. Wang, M. J. Jafari, N. N. Wang, D. P. Qian, F. L. Zhang, T. Ederth, E. Moons, J. P. Wang, O. Inganas, W. Huang, and F. Gao. *Journal of Materials Chemistry A*, 6(25):11884–11889, 2018.

301. N. N. Liang, D. Meng, Z. T. Ma, B. Kan, X. Y. Meng, Z. Zheng, W. Jiang, Y. Li, X. J. Wan, J. H. Hou, W. Ma, Y. S. Chen, and Z. H. Wang. *Advanced Energy Materials*, 7(6), 2017.

302. R. Cheacharoen, W. R. Mateker, Q. Zhang, B. Kan, D. Sarkisian, X. F. Liu, J. A. Love, X. J. Wan, Y. S. Chen, T. Q. Nguyen, G. C. Bazan, and M. D. McGehee. 161:368–376, 2017.

303. J. Min, X. C. Jiao, V. Sgobba, B. Kan, T. Heumuller, S. Rechberger, E. Spiecker, D. M. Guldi, X. J. Wan, Y. S. Chen, H. Ade, and C. J. Brabec. *Nano Energy*, 28:241–249, 2016.

304. P. R. Brown, D. Kim, R. R. Lunt, N. Zhao, M. G. Bawendi, J. C. Grossman, and V. Bulovic. *Acs Nano*, 8(6):5863–5872, 2014.

305. L. E. Brus. *Journal of Chemical Physics*, 80(9):4403–4409, 1984.

306. D. Jia, J. Chen, S. Zheng, D. Phuyal, M. Yu, L. Tian, J. Liu, O. Karis, H. Rensmo, and E. M. Johansson. *Advanced Energy Materials*, 9(44):1902809, 2019.

307. K. Y. Lu, Y. J. Wang, Z. K. Liu, L. Han, G. Z. Shi, H. H. Fang, J. Chen, X. C. Ye, S. Chen, F. Yang, A. G. Shulga, T. Wu, M. F. Gu, S. J. Zhou, J. Fan, M. A. Loi, and W. L. Ma. *Advanced Materials*, 30(25), 2018.

308. J. B. Zhang, J. B. Gao, C. P. Church, E. M. Miller, J. M. Luther, V. I. Klimov, and M. C. Beard. *Nano Letters*, 14(10):6010–6015, 2014.

309. M. X. Liu, Y. L. Chen, C. S. Tan, R. Quintero-Bermudez, A. H. Proppe, R. Munir, H. R. Tan, O. Voznyy, B. Scheffel, G. Walters, A. P. T. Kam, B. Sun, M. J. Choi, S. Hoogland, A. Amassian, S. O. Kelley, F. P. G. de Arquer, and E. H. Sargent. *Nature*, 570(7759):96–+, 2019.

310. M. M. Hao, Y. Bai, S. Zeiske, L. Ren, J. X. Liu, Y. B. Yuan, N. Zarrabi, N. Y. Cheng, M. Ghasemi, P. Chen, M. Q. Lyu, D. X. He, J. H. Yun, Y. Du, Y. Wang, S. S. Ding, A. Armin, P. Meredith, G. Liu, H. M. Cheng, and L. Z. Wang. *Nature Energy*, 5(1):79–88, 2020.

311. S. Premkumar, D. Liu, Y. M. Zhang, D. Nataraj, S. Ramya, Z. Z. Jin, B. B. Mamba, A. T. Kuvarega, and J. Z. Gui. *Acs Applied Nano Materials*, 3(9):9141–9150, 2020.

312. Y. G. Rong, Y. Hu, A. Y. Mei, H. R. Tan, M. I. Saidaminov, S. I. Seok, M. D. McGehee, E. H. Sargent, and H. W. Han. *Science*, 361(6408), 2018.

313. Y. N. Zhang, T. Shah, F. L. Deepak, and B. A. Korgel. *Chemistry of Materials*, 31(19):7962–7969, 2019.

314. J. T. Oh, S. Y. Bae, S. R. Ha, H. Cho, S. J. Lim, D. W. Boukhvalov, Y. Kim, and H. Choi. *Nanoscale*, 11(19):9633–9640, 2019.

315. L. Hu, R. J. Patterson, Z. L. Zhang, Y. C. Hu, D. B. Li, Z. H. Chen, L. Yuan, Z. L. Teh, Y. J. Gao, G. J. Conibeer, and S. J. Huang. *Journal of Materials Chemistry C*, 6(4):731–737, 2018.

316. J. Choi, M. J. Choi, J. Kim, F. Dinic, P. Todorovic, B. Sun, M. Y. Wei, S. W. Baek, S. Hoogland, F. P. G. de Arquer, O. Voznyy, and E. H. Sargent. *Advanced Materials*, 32(7), 2020.

317. D. Becker-Koch, M. Albaladejo-Siguan, V. Lami, F. Paulus, H. Y. Xiang, Z. Y. Chen, and Y. Vaynzof. *Sustainable Energy Fuels*, 4(1):108–115, 2020.

318. A. R. Kirmani, A. D. Sheikh, M. R. Niazi, M. A. Haque, M. X. Liu, F. P. G. de Arquer, J. X. Xu, B. Sun, O. Voznyy, N. Gasparini, D. Baran, T. Wu, E. H. Sargent, and A. Amassian. *Advanced Materials*, 30(35), 2018.

319. H. Aqoma, M. Al Mubarok, W. Lee, W. T. Hadmojo, C. Park, T. K. Ahn, D. Y. Ryu, and S. Y. Jang. *Advanced Energy Materials*, 8(23), 2018.

320. X. L. Zhang, Y. Justo, J. Maes, W. Walravens, J. D. Zhang, J. H. Liu, Z. Hens, and E. M. J. Johansson. *Journal of Materials Chemistry A*, 3(41):20579–20585, 2015.

321. D. C. J. Neo, N. L. Zhang, Y. Tazawa, H. B. Jiang, G. M. Hughes, C. R. M. Grovenor, H. E. Assender, and A. A. R. Watt. *Acs Applied Materials Interfaces*, 8(19):12101–12108, 2016.

322. S. W. Baek, S. Jun, B. Kim, A. H. Proppe, O. Ouellette, O. Voznyy, C. Kim, J. Kim, G. Walters, J. H. Song, S. Jeong, H. R. Byun, M. S. Jeong, S. Hoogland, F. P. G. de Arquer, S. O. Kelley, J. Y. Lee, and E. H. Sargent. *Nature Energy*, 4(11):969–976, 2019.

323. C. H. M. Chuang, P. R. Brown, V. Bulovic, and M. G. Bawendi. *Nature Materials*, 13(8):796–801, 2014.

324. S. Q. Ming, X. H. Liu, W. X. Zhang, Q. M. Xie, Y. L. Wu, L. J. Chen, and H. Q. Wang. *Journal of Cleaner Production*, 246, 2020.

325. Y. Yu, O. Solomeshch, H. Chechik, A. A. Goryunkov, R. F. Tuktarov, D. H. Choi, J. Jin, Y. Eichen, and N. Tessler. *Journal of Applied Physics*, 104(12):124505, 2008.

326. D. Becker-Koch, M. Albaladejo-Siguan, Y. J. Hofstetter, O. Solomeshch, D. Pohl, B. Rellinghaus, N. Tessler, and Y. Vaynzof. *Acs Applied Materials Interfaces*, 13:18750–18757, 2021.

327. C. Li, S. Tscheuschner, F. Paulus, P. E. Hopkinson, J. Kiessling, A. Kohler, Y. Vaynzof, and S. Huettner. *Advanced Materials*, 28(12):2446–2454, 2016.

328. S. Svanstrom, T. J. Jacobsson, G. Boschloo, E. M. J. Johansson, H. Rensmo, and U. B. Cappel. *Acs Applied Materials Interfaces*, 12(6):7212–7221, 2020.

329. L. Yan, Y. Wang, J. Wei, G. Ji, H. Gu, Z. Li, J. Zhang, Q. Luo, Z. Wang, and X. Liu. *Journal of Materials Chemistry A*, 7(12):7099–7108, 2019.

330. J. H. Simmons and K. S. Potter. *Optical Materials*. Academic Press, 2021.

331. A. W. Galston. *Bioscience*, 42(7):490–493, 1992.

332. Z. Zhu, J. H. Jiang, and Y. Fa. *Molecules*, 25(22), 2020.

333. S. Tsujimura, A. Wadano, K. Kano, and T. Ikeda. *Enzyme and Microbial Technology*, 29(4-5):225–231, 2001.

334. M. K. Sarma, M. G. A. Quadir, R. Bhaduri, S. Kaushik, and P. Goswami. *Biosensors Bioelectronics*, 119:94–102, 2018.

335. J. M. Pisciotta, Y. J. Zou, and I. V. Baskakov. *Applied Microbiology and Biotechnology*, 91(2):377–385, 2011.

336. A. E. Inglesby, K. Yunus, and A. C. Fisher. *Physical Chemistry Chemical Physics*, 15(18):6903–6911, 2013.

337. E. Cevik, M. Titiz, and M. Senel. *Electrochimica Acta*, 291:41–48, 2018.

338. H. Lee and S. Choi. *Lab on a Chip*, 15(2):391–398, 2015.

339. D. J. Lea-Smith, P. Bombelli, R. Vasudevan, and C. J. Howe. *Biochimica Et Biophysica Acta-Bioenergetics*, 1857(3):247–255, 2016.

340. D. R. Lovley. *Energy Environmental Science*, 4(12):4896–4906, 2011.

341. G. Reguera, K. D. McCarthy, T. Mehta, J. S. Nicoll, M. T. Tuominen, and D. R. Lovley. *Nature*, 435(7045):1098–1101, 2005.

342. Y. A. Gorby, S. Yanina, J. S. McLean, K. M. Rosso, D. Moyles, A. Dohnalkova, T. J. Beveridge, I. S. Chang, B. H. Kim, K. S. Kim, D. E. Culley, S. B. Reed, M. F. Romine, D. A. Saffarini, E. A. Hill, L. Shi, D. A. Elias, D. W. Kennedy, G. Pinchuk, K. Watanabe, S. Ishii, B. Logan, K. H. Nealson, and J. K. Fredrickson. *Proceedings of the National Academy of Sciences of the United States of America*, 103(30):11358–11363, 2006.

343. C. A. E. Hauser and S. G. Zhang. *Nature*, 468(7323):516–517, 2010.

344. A. P. Borole, G. Reguera, B. Ringeisen, Z. W. Wang, Y. J. Feng, and B. H. Kim. *Energy Environmental Science*, 4(12):4813–4834, 2011.

345. N. Sekar, R. Jain, Y. Yan, and R. P. Ramasamy. *Biotechnology and Bioengineering*, 113(3):675–679, 2016.

346. K. Hasan, H. B. Yildiz, E. Sperling, P. O. Conghaile, M. A. Packer, D. Leech, C. Hagerhall, and L. Gorton. *Physical Chemistry Chemical Physics*, 16(45):24676–24680, 2014.

347. T. Kothe, N. Plumere, A. Badura, M. M. Nowaczyk, D. A. Guschin, M. Rogner, and W. Schuhmann. *Angewandte Chemie-International Edition*, 52(52):14233–14236, 2013.

348. G. Cerullo, C. Manzoni, L. Luer, and D. Polli. *Photochemical Photobiological Sciences*, 6(2):135–144, 2007.

349. P. M. Champion. *Science*, 310(5750):980–982, 2005.

350. P. Kukura, D. W. McCamant, S. Yoon, D. B. Wandschneider, and R. A. Mathies. *Science*, 310(5750):1006–1009, 2005.

351. G. Cerullo, D. Polli, G. Lanzani, S. De Silvestri, H. Hashimoto, and R. J. Cogdell. *Science*, 298(5602):2395–2398, 2002.

352. R. Croce and H. van Amerongen. *Nature Chemical Biology*, 10(7):492–501, 2014.

353. A. V. Ruban, M. P. Johnson, and C. D. P. Duffy. *Biochimica Et Biophysica Acta-Bioenergetics*, 1817(1):167–181, 2012.

354. W. P. Bricker, P. M. Shenai, A. Ghosh, Z. T. Liu, M. G. M. Enriquez, P. H. Lambrev, H. S. Tan, C. S. Lo, S. Tretiak, S. Fernandez-Alberti, and Y. Zhao. *Scientific Reports*, 5, 2015.

355. S. Mukamel. *Principles of nonlinear optical spectroscopy*. Oxford University Press, 1999.

356. M. Zavelani-Rossi, G. Cerullo, S. De Silvestri, L. Gallmann, N. Matuschek, G. Steinmeyer, U. Keller, G. Angelow, V. Scheuer, and T. Tschudi. *Optics Letters*, 26(15):1155–1157, 2001.

357. E. Meneghin, C. Leonardo, A. Volpato, L. Bolzonello, and E. Collini. *Scientific Reports*, 7, 2017.

358. Y. J. Zou, J. Pisciotta, R. B. Billmyre, and I. V. Baskakov. *Biotechnology and Bioengineering*, 104(5):939–946, 2009.

359. L. G. Erokhina, T. A. Vishnivetskaya, and D. A. Gilichinskii. The content and composition of phycobilisome pigments in cells of ancient viable cyanobacteria from arctic permafrost. *Microbiology*, 67(6):682–687, 1998.

360. M. P. Johnson. *Understanding Biochemistry 2*, 60(3):255–273, 2016.

361. K. S. Cole and R. H. Cole. *The Journal of Chemical Physics*, 9(4):341–351, 1941.

362. Y. P. Kalmykov, W. T. Coffey, D. S. F. Crothers, and S. V. Titov. *Physical Review E*, 70(4), 2004.

363. W. S. Chow. *Journal of Biological Physics*, 29(4):447–459, 2003.

364. C. C. Moser and P. L. Dutton. *Biochimica Et Biophysica Acta*, 1101(2):171–176, 1992.

365. P. Halldal. *The Biological Bulletin*, 134(3):411–424, 1968.

366. I. Fujita, M. S. Davis, and J. Fajer. *Journal of the American Chemical Society*, 100(19):6280–6282, 1978.

367. J. Baugher, J. C. Hindman, and J. J. Katz. *Chemical Physics Letters*, 63(1):159–162, 1979.

368. P. D. Laible, C. Kirmaier, C. S. M. Udawatte, S. J. Hofman, D. Holten, and D. K. Hanson. *Biochemistry*, 42(6):1718–1730, 2003.

369. L. Dhar, J. A. Rogers, and K. A. Nelson. *Chemical Reviews*, 94(1):157–193, 1994.

370. D. Liu, L. Yang, Y. Wu, X. Wang, Y. Zeng, G. Han, H. Yao, S. Li, S. Zhang, and Y. Zhang. *Chemistry of Materials*, 30(3):619–628, 2018.

371. L. Wilbraham, E. Berardo, L. Turcani, K. Jelfs, and M. Zwijnenburg. 30(12):2450–2459, 2018.

372. S. Curtarolo, G. L. W. Hart, M. B. Nardelli, N. Mingo, S. Sanvito, and O. Levy. *Nature Materials*, 12(3):191–201, 2013.

373. J. Hachmann, R. Olivares-Amaya, A. Jinich, A. L. Appleton, M. A. Blood-Forsythe, L. R. Seress, C. Román-Salgado, K. Trepte, S. Atahan-Evrenk, and S. Er. *Energy Environ. Sci.*, 7(2):698–704, 2014.

374. M. C. Scharber, D. Mühlbacher, M. Koppe, P. Denk, C. Waldauf, A. J. Heeger, and C. J. Brabec. *Advanced Materials*, 18(6):789–794, 2006.

375. R. F. Murphy. *Nature Chemical Biology*, 7(6):327–330, 2011.

376. W. P. Walters and M. Namchuk. *Nature Reviews Drug Discovery*, 2(4):259–266, 2003.

377. A. Mannodi-Kanakkithodi, A. Chandrasekaran, C. Kim, T. D. Huan, G. Pilania, V. Botu, and R. Ramprasad. *Materials Today*, 21(7):785–796, 2018.

378. G. Panapitiya, G. Avendaño-Franco, P. Ren, X. Wen, Y. Li, and J. P. Lewis. *Journal of the American Chemical Society*, 140(50):17508–17514, 2018.

379. H. Sahu, F. Yang, X. Ye, J. Ma, W. Fang, and H. Ma. *Journal of Materials Chemistry A*, 7(29):17480–17488, 2019.

380. D. Padula, J. D. Simpson, and A. Troisi. *Materials Horizons*, (2):343–349, 2019.

381. C. G. Shuttle, R. Hamilton, B. C. Oregan, J. Nelson, and J. R. Durrant. *Proceedings of the National Academy of Sciences*, 107(38):16448–16452, 2010.

382. A. Rao, P. C. Y. Chow, S. Gélinas, C. W. Schlenker, C. Li, H. Yip, A. K.-Y. Jen, D. S. Ginger, and R. H. Friend. *Nature*, (7463):435–439, 2013.

383. D. R. Klug, T. Rech, D. M. Joseph, J. Barber, J. R. Durrant, and G. Porter. *Chemical Physics*, 194(2-3):433–442, 1995.

384. J. P. Connelly, M. G. Müller, R. Bassi, R. Croce, and A. R. Holzwarth. *Biochemistry*, 36(2):281–287, 1997.

385. J. Wendler, A. Holzwarth, and W. Wehrmeyer. *Biochimica et Biophysica Acta - Bioenergetics*, 765(1):58–67, 1984.

386. D. J. Gardiner, P. R. Graves, and H. J. Bowley. *Practical raman spectroscopy*. Springer, 1989.